UNIVERSIDAD AUTÓNOMA DE NUEVO LEÓN
FACULTAD DE CIENCIAS QUÍMICAS

EVALUATION OF A TiO_2 SEMICONDUCTOR FORMED BY BIOMINERALIZATION INDUCED BY PEARL OYSTERS FOR THE PHOTOCATALYTIC DEGRADATION OF MICROPLASTICS

Presentado por:

Ing. Brenda Estefanía Llorente García

Director:

Dra. Erika Iveth Cedillo González

Co-director

Dr. Pasiano Rivas García

Co-directores externos

Dr. Pedro E. Saucedo (CIBNOR), Dra. Cristina Siligardi (UNIMORE)

Como requisito parcial para obtener el Grado de MAESTRÍA EN CIENCIAS con orientación en PROCESOS SUSTENTABLES

Monterrey, Nuevo León. Abril de 2020

EVALUATION OF A TiO2 SEMICONDUCTOR FORMED BY BIOMINERALIZATION INDUCED BY PEARL OYSTERS FOR THE PHOTOCATALYTIC DEGRADATION OF MICROPLASTICS

Revisión de la Tesis:

Dra. Erika Iveth Cedillo González
Directora de Tesis

Dr. Pasiano Rivas García
Co-director interno

Dr. Juan Manuel Hernández López
Comité tutorial

Dr. Carlos Escamilla Alvarado
Comité tutorial

Dra. Astrid Iriana Sánchez Vázquez
Comité tutorial

EVALUATION OF A TiO2 SEMICONDUCTOR FORMED BY BIOMINERALIZATION INDUCED BY PEARL OYSTERS FOR THE PHOTOCATALYTIC DEGRADATION OF MICROPLASTICS

Aprobación de la Tesis:

Dra. Erika Iveth Cedillo González

Presidente

Dr. Juan Manuel Hernández López

Secretario

Dr. Carlos Escamilla Alvarado

Vocal

Dra. María Elena Cantú Cárdenas

Sub-Directora de Posgrado

AGRADECIMIENTOS

A la Universidad Autónoma de Nuevo León, a la Fundación UANL y en especial a la Facultad de Ciencias Químicas por permitirme realizar mis estudios de posgrado y por las becas otorgadas.

Al programa del Gobierno de México de becas nacionales CONACYT por el apoyo económico brindado a lo largo de la realización de este proyecto.

Al Proyecto CONACYT APN 2017-5167 por el apoyo financiero para la realización de los experimentos, la estancia en el CIBNOR y la presentación en el congreso PACRIM 2019 de Okinawa.

A mi familia por todo su apoyo incondicional en todas mis decisiones.

A mi asesora Dra. Erika I. Cedillo González por su paciencia, enseñanzas y las oportunidades que me brindó para hacerme crecer como persona y profesionista.

Al doctor Pedro E. Saucedo Lastra por su gran orientación, ayuda y motivarme de gran manera en este trayecto. Muchas gracias por todo su apoyo.

A todos en *Perlas del Cortez* por su amistad y ayuda, sin ustedes este proyecto no hubiera sido posible.

A la doctora Cristina Siligardi por darme la oportunidad de conocer nuevos campos de aplicación. Le agradezco mucho todo lo que hizo por mí.

Al doctor Pasiano Rivas Garcia por su tiempo.

Con mucho cariño le agradezco a Camila, Beatrice, Mary, y todos los compañeros del DIEF. Sin ustedes el viaje no hubiera sido igual. Gracias por escucharme y por esa gran amistad, los quiero.

A los miembros del Comité Tutorial.

RESUMEN

Ing. Brenda Estefanía Llorente García Fecha de Graduación: Agosto 2020

Universidad Autónoma de Nuevo León

Facultad de Ciencias Químicas

Título del estudio: EVALUATION OF A TiO_2 SEMICONDUCTOR FORMED BY BIOMINERALIZATION INDUCED BY PEARL OYSTERS FOR THE PHOTOCATALYTIC DEGRADATION OF MICROPLASTICS.

Número de páginas: 129

Candidato para el grado de Maestro en Ciencias con orientación en Procesos Sustentables.

Área de estudio: Procesos Sustentables

Propósito y método de estudio:

El plástico es una pieza clave para la sociedad, pues se utiliza desde la seguridad alimentaria hasta el desarrollo de la ciencia y tecnología. Sin embargo, su uso excesivo y la mala gestión de residuos plásticos hace que estos terminen en ecosistemas marinos y terrestres. El plástico liberado en el medio ambiente puede ser fragmentado o ser liberado directamente en pequeñas partículas con diámetros < 5 mm, los cuales son conocidos como microplásticos y provocan

daños irreversibles a los ecosistemas. Los microplásticos se convierten en contaminantes en biodisponibles para la biota y representan un riesgo debido a la toxicidad acumulativa dentro de la red trófica. En este estudio, se propone la utilización de la fotocatálisis para la degradación de microplásticos, usando la ruta sintética de biomineralización para la obtención de semiconductores a temperatura ambiente.

El propósito del presente estudio fue la evaluación y obtención de semiconductores de TiO_2 sintetizados mediante biomineralización, usando una ostra perlera mexicana *Pteria sterna*. Primeramente, se obtuvieron los semiconductores amorfos (precursores) y posteriormente se biomineralizaron por 20, 32, 77, y 90 días mediante la incubación dentro de las ostras perleras. Se realizó la caracterización de dichos semiconductores en términos de composición cristalográfica (XRD), absorción de luz (Espectroscopía UV-Vis) y presencia de grupos funcionales (FTIR). Una vez establecidos los semiconductores con las mejores propiedades, se procedió a evaluar su actividad fotocatalítica para la degradación de microplásticos de polietileno. Se utilizó el polietileno de alta densidad (HDPE, por sus siglas en inglés) con diferentes tamaños de partícula (381.87 y 876.26 μm). Los microplásticos fueron extraídos de tres marcas de exfoliantes faciales comercialmente disponibles en la mayoría de los supermercados y comercios dedicados al sector cosmético en México.

Las pruebas fotocatalíticas se realizaron con tres semiconductores: el precursor amorfo, y los materiales biomineralizados por 32 y 90 días. Estos materiales son predominantemente amorfos y contienen nitrógeno, lo que los

hace activos en luz visible. Las pruebas se realizaron en medio acuoso a una temperatura de 31 ± 3 ºC a pH 7 ± 1 usando una lámpara LED con emisión en el intervalo de 400 a 700 nm. El tiempo de irradiación fue de 30 horas. La degradación fue evaluada mediante pérdida de masa, cambios en las bandas de absorción del espectro FTIR de los microplásticos, índice vinilo y microscopía óptica. Los resultados de las pruebas de fotólisis demostraron que los medios de reacción evaluados no promueven la fotocatálisis de los microplásticos. En las pruebas fotocatalíticas de los microplásticos con tamaño de partícula de 381.87 µm, se obtuvieron pérdidas de masa de 26.93% y 5.89% para los semiconductores biomineralizados por 32 y 90 días, respectivamente. Para los microplásticos con tamaño de partícula de 876.26 µm, se obtuvieron pérdidas de masa de 3.5% y 19.51%, para los semiconductores biomineralizados por 32 y 90 días, respectivamente. Con este estudio, quedó demostrado que los semiconductores de TiO_2 biomineralizado en ostras perleras (*Pteria sterna*) por 32 y 90 días permanecen predominantemente amorfos, contienen nitrógeno y son activos en luz visible, propiedades que los hacen capaces de degradar fotocatalíticamente microplásticos de HDPE en medio acuoso a pH 7 y temperatura ambiente.

Firma del asesor: Erika Cedillo

Dra. Erika Iveth Cedillo González

SUMMARY

Ing. Brenda Estefania Llorente Garcia Graduation date: August 2020

Universidad Autónoma de Nuevo León

Facultad de Ciencias Químicas

Thesis Title: EVALUATION OF A TiO_2 SEMICONDUCTOR FORMED BY BIOMINERALIZATION INDUCED BY PEARL OYSTERS FOR THE PHOTOCATALYTIC DEGRADATION OF MICROPLASTICS.

Number of pages: 129

Candidate for the Master of Science with orientation in Sustainable Processes

Study area: Sustainable Processes

Purpose and method of study:

Plastic has a crucial role in modern society. It is used for food security and in the development of science and technology. However, because of its excessive use and the poorly waste mismanagement of plastic this end up in marine and terrestrial ecosystems. Plastic released into the environment can be fragmented or directly released into small particles with diameters of <5 mm, which are known as microplastics and cause irreversible damage to ecosystems. Microplastics become pollutants that are bioavailable for biota and represent a critical risk due to cumulative toxicity within the food web. In this study, the use of photocatalysis

for the degradation of microplastics is proposed, using the synthetic route of biomineralization to obtain semiconductors at room temperature.

The purpose of the present study was the evaluation and obtaining of TiO_2 semiconductors synthesized by biomineralization, using a Mexican pearl oyster *Pteria sterna*. The amorphous semiconductors (precursors) were obtained and subsequently biomineralized for 20, 32, 77, and 90 days by incubation within pearl oysters. These semiconductors were characterized in terms of crystallographic composition (XRD), light absorption (UV-Vis spectroscopy) and the presence of functional groups (FTIR). Once the semiconductors with the best properties were established, their photocatalytic activity was evaluated for the degradation of polyethylene microplastics. High-density polyethylene (HDPE) with different particle sizes (381.87 and 876.26 µm) was used. The microplastics were extracted from three brands of facial scrubs commercially available in most supermarkets and shops dedicated to the cosmetic sector in Mexico.

Photocatalytic tests were performed with three semiconductors: the amorphous precursor, and the biomineralized materials for 32 and 90 days. These materials are predominantly amorphous and contain nitrogen, making them active in visible light. The tests were performed in aqueous medium at a temperature of 31 ± 3 ºC at pH 7 ± 1 using an LED lamp with emission in the range of 400 to 700 nm. The irradiation time was 30 hours. The degradation was evaluated by mass loss, changes in the absorption bands of the FTIR spectrum of microplastics, vinyl index and light microscopy. The results of the photolysis tests showed that the evaluated reaction media do not promote the photocatalysis of the microplastics. In photocatalytic tests of microplastics with a particle size of 381.87 µm, mass

losses of 26.93% and 5.89% were obtained for biomineralized semiconductors for 32 and 90 days, respectively. For microplastics with a particle size of 876.26 µm, mass losses of 3.5% and 19.51% were obtained, for biomineralized semiconductors for 32 and 90 days, respectively. With this study, it was demonstrated that the biomineralized TiO_2 semiconductors in pearl oysters (*Pteria sterna*) for 32 and 90 days remain predominantly amorphous, contain nitrogen and are active in visible light, this properties make them capable of photocatalytically degrading HDPE microplastics in aqueous media at pH 7 and room temperature.

TABLE OF CONTENTS

AGRADECIMIENTOS I

TABLE OF CONTENTS X

LIST OF TABLES XIV

LIST OF FIGURES XIV

NOMENCLATURE 1

CHAPTER 1 4

1. INTRODUCTION 4

CHAPTER 2 8

2. PROBLEM STATEMENT 8

2.1 Plastic and microplastic pollution. 8

2.1.1 Microplastics definitions. 10

2.1.2 Primary and secondary microplastics. 11

2.1.3 The pathways of microplastics into the environment 12

2.1.4 Effects of microplastics in marine environments and their biota. 14

2.1.5 Effects of microplastics in terrestrial environments and their biota. 15

2.1.6 Current strategies for fighting microplastic pollution. 16

CHAPTER 3 19

3. STATE OF THE ART AND CRITICAL ANALAYSIS OF THE LITERATURE 19

3.1 Photocatalysis of plastics. 19

3.2 Photocatalysis of microplastics. 21

3.3 Biomineralization of semiconductors. 25

CHAPTER 4 27

4. HYPOTHESIS AND OBJECTIVES 27
4.1 Hypothesis. 27
4.2 General objective. 27
4.3 Specific objectives. 28
4.4 Scientific contribution. 28
CHAPTER 5 29
5. THEORETICAL FRAMEWORK 29
5.1 Photocatalysis. 29
5.2 Semiconductors 32
5.2.1 TiO_2 photocatalyst. 35
5.3 Crystalline and amorphous solids 37
5.3.1 Crystallization of solids by biomineralization. 38
5.4 Biomineralization (fundamentals). 40
5.4.1 Biomineralization with pearl oysters. 42
CHAPTER 6 45
6. EXPERIMENTAL PROCEDURES 45
6.1 Microplastics obtainment and characterization 45
6.2 Biomineralization 46
6.2.1 Amorphous TiO_2 obtainment. 47
6.2.2 Organism obtainment and characterization 48
6.2.3 Relaxation methodology 49
6.2.4 Tablet implantation 50
6.2.5 Tablet extraction 51
6.3 Semiconductor characterization 52

6.4 Determination of the pollutant model, particle shape and size and semiconductor presentation 53
6.4.1 Sol-gel and bioinspired synthesis for preliminary tests 54
6.4.2 Model pollutants for preliminary tests 55
6.4.3 Preliminary photocatalytic tests 56
6.5 Photocatalysis of microplastics with the biomineralized materials. 58
6.6 Generated waste disposal 61
CHAPTER 7 62
7. RESULTS AND DISCUSSION 62
7.1 Microplastics characterization 62
7.1.1 Microplastics used in the preliminary tests 62
7.1.2 Microplastics for testing the photocatalytic activity of the biomineralization-derived TiO_2 materials 67
7.2 Amorphous TiO_2 characterization 69
7.3 Biomineralization results 75
7.3.1 Organisms survival ratio 75
7.3.2 Tablet rejection ratio 76
7.3.3 Biomineralized TiO_2 materials 77
7.3.3.1 XRD analysis 77
7.3.3.2 FTIR analysis 80
7.3.3.3 UV-Vis analysis 83
7.4 Preliminary tests for the selection of the operational conditions of the photocatalytic tests for the biomineralized materials 87
7.4.1 Semiconductor characterization 87
7.4.2 Photocatalytic test with the semiconductors in the form of coatings 93

7.4.3 Photocatalytic test with the semiconductors in the form of powders 97

7.5 Photocatalysis with biomineralized semiconductors 98

CHAPTER 8 112

8. CONCLUSIONS 112

REFERENCES 115

APPENDIX A: Diffusion of the project 130

APPENDIX B: Paper accepted for publication on Journal Coatings (MDPI), ISSN 2079-6412, Impact Factor of 2.33 (JCR). 131

LIST OF TABLES

Table 1. Conventional photocatalytic semiconductors, band-gap energy, and the corresponding absorption edge..... 34
Table 2. Description of the preliminary photocatalytic tests..... 58
Table 3. Description of the photocatalytic tests using the biomineralized materials. 61
Table 4. Eg. calculation using Kubelka Munk function..... 86
Table 5 . Eg calculation using Kubelka Munk function..... 92
Table 6. Calculation of VI and UVI for HDPE 381.87 µm..... 109
Table 7. Calculation of VI and UVI for HDPE 876.26 µm..... 109
Table 8. Wastes and disposition containers. 61

LIST OF FIGURES

Figure 1. Example of primary and secondary microplastics. 12
Figure 2. The entrance of microplastics to the environment. (1) fragmentation of tire wears and littering, (2) fragmentation of larger plastics, (3) atmospheric release and dispersion by wing, (4) sewage, and (5) illegal waste dumping..... 13
Figure 3. Mechanism of photocatalysis. The scheme took from Byrne et al., 2018. [68]..... 30
Figure 4. Calcite (a) and aragonite structure (b). Ca (green) O (red) C (gray). Structures taken from Omair et al. (2016). [90]..... 38
Figure 5. Architectural arrangement of the shell of a marine pearl oyster of the genus *Pinctada*, (Taken from Levi *et al.* (1998) [92]). 39
Figure 6. The shell of *Pteria sterna* and the layers subdivision. 43
Figure 7. Facilities of *Perlas del Cortez* (a) and the line (b). 47
Figure 8. Pearls oyster *Pteria sterna*..... 48
Figure 9. Culture cages (a) and the line were organism were kept (b)..... 49

Figure 10. Relaxation methodology..... 50
Figure 11. Implantation of one precursor tablet..... 51
Figure 12. Experimental procedure for preliminary photocatalytic tests..... 56
Figure 13. Experimental procedure for photocatalytic tests. 59
Figure 14. Optical micrograph of the microbeads obtained from the two commercial scrubs. (a) Brand A, (b) Brand B..... 63
Figure 15. FTIR spectrum of microbeads extracted from the commercial facial scrubs. 64
Figure 16. XRD diffractogram of microbeads extracted from the commercial facial scrubs (a) Brand A and (b) Brand B..... 65
Figure 17. Microplastics in the form of films obtained from the commercial bag. (a) Films of size 5x5 mm, (b) Films of size 3x3 mm. 66
Figure 18. FTIR spectrum of microplastics extracted from the commercial plastic bag..... 67
Figure 19. Optical micrograph of the microbeads from the commercials facial scrub of Brand C. 68
Figure 20. FTIR spectrum of microbeads extracted from the commercial facial scrubs. 69
Figure 21. XRD diffractogram of the amorphous TiO_2 precursor..... 70
Figure 22. FTIR spectrum of amorphous TiO_2 precursor 71
Figure 23. (a) Diffuse reflectance spectrum of the amorphous TiO_2 precursor and (b) Kubelka-Munk transformation for Eg calculation. 72
Figure 24. SEM micrograph of the amorphous TiO_2 precursor. 73
Figure 25. N_2 adsorption-desorption isotherm of amorphous precursor TiO_2... 74
Figure 26. XRD patterns of the TiO_2 materials biomineralized inside the P.sterna oysters for PS20N, PS32N, PS77N and PS90N days. For comparison, the spectrum of the TiO_2 amorphous precursor was included. Also, the characteristic peaks of the anatase phase are shown (ICDD file 21-1272)..... 78
Figure 27. FTIR spectra of the TiO_2 biomineralized inside *P.sterna* oyster for 20, 32, 77 and 90 days. 81

Figure 28. UV-Vis absorption spectra of biomineralized (a-d) and amorphous TiO_2 (e) semiconductors. 84
Figure 29. Plots $(F(R)*hv)^{1/2}$ vs hv of biomineralized (a-d) and amorphous TiO_2 (e) semiconductors. 85
Figure 30. XRD of the bioinspired N-TiO_2. 88
Figure 31. XRD of the sol gel derived N-TiO_2..... 89
Figure 32. ATR-FTIR spectrum of the bioinspired N-TiO_2. 90
Figure 33. ATR-FTIR spectrum of the sol gel derived N-TiO_2. 91
Figure 34. FEG-SEM micrographs of the N-TiO_2 bioinspired (a) and sol gel derived (b) coating. 93
Figure 35. Mass loss after 50 h of photocatalysis using the mesoporous N-TiO_2 coating. 94
Figure 36. Formation of a LDPE MP's layer. 95
Figure 37. Mass loss after 50 h of photocatalysis with microplastics using the bioinspired N-TiO_2 coating. 96
Figure 38. Changes in mass obtained during the photocatalytic degradation tests of the LDPE microplastics using both semiconductors. 97
Figure 39. Mass loss of HDPE microplastics (814 µm) after 30 h of photolysis. 99
Figure 40. Mass loss after 30 h of photocatalysis for HDPE 381.87 µm. 102
Figure 40. Mass loss after 30 h of photocatalysis for HDPE 876.26 µm. 103
Figure 42. Optical micrography of pristine HDPE (381.87 µm) and after irradiation for 30 with different semiconductors. 104
Figure 43. Optical micrography of pristine HDPE (876.26 µm) and after irradiation for 30 with different semiconductors. 106
Figure 44. ATR-FTIR for HDPE microplastics (381.87 µm), and after 30 h of photocatalytic degradation with different semiconductors. 107
Figure 45. ATR-FTIR for HDPE (876.26 µm) microplastics and after 30 h of photocatalytic degradation with different semiconductors. 108

NOMENCLATURE

µg	Microgram
$^{\bullet}OH$	Hidroxyl radical
ATR	Attenuated Total Reflectance
BET	Brunauer–Emmett–Teller theory
CB	Conduction Band
cm	Centimeters
CO_2	Carbon dioxide
DRS	Diffuse Refelctance Spectroscopy
e^-	Electron
EDS	Energy-Dispersive X-Ray Spectroscopy
EPF	Extrapallial Fluid
Eg	Band-gap energy
eV	Electron volts
FEG-SEM	Field Emission Gun-SEM
FTIR	Fourier Transform Infrared Spectroscopy
g	Grams
h	Hours
h^+	Holes
HDPE	High Density Polyethylene
hv	Photon energy

IR	Infrared
LDPE	Low Density Polyethylene
mg	Milligrams
min	Minutes
mL	Milliliter
mm	Millimeter
MPa	Mega Pascal
MPs	Microplastics
nm	Nanometers
N-TiO_2	Nitrogen doped Titanium dioxide
^oC	Graus Celsius
PBTs	Bio- accumulative Toxic Ssubstances
PCBs	Poly-Chlorinated Biphenyls
PE	Polyethylene
POP	Persisting Organic Pollutant
PP	Polypropylene
PVC	Polyvinyl chloride
rpm	Revolutions per minute
SEM	Scanning Electron Microscopy
T	Temperature
t	Time
TiO_2	Titanium dioxide
UV	Ultraviolet

VB	Valence Band
W	Watts
wt%	Weight percentage
WWTPs	Wastewater Treatment Plants
XPS	X-Ray Photoelectron Spectroscopy
XRD	X-Ray Diffraction
λ	Wavelength
μm	Micrometer

CHAPTER 1

1. INTRODUCTION

The ocean, which covers about 70% of the Earth's surface, has a great historical value for the life and humankind. The marine environment hosts a wide range of biodiversity and offers many environmental services. The sea provides essential benefits for human society, such as sustenance, transport, and recreation. Regardless of their critical role, the oceans are currently endangered because of a poor management of the anthropogenic solid wastes such as wood, metals, and, plastics [1,2].

From the total quantity of anthropogenic wastes present in the sea, plastic represents more than 80% [3]. Plastic degradation is temperature-dependent. For example, depending of the polymer type, thermal degradation takes place at temperatures higher than 200 °C [4], but the oceans have a surface temperature between 0 to 29 °C [5]. This means that plastic degradation rate is slow in cold seawaters [6] and it is estimated to take 450 years [7].

Although plastic has very valuable characteristics such as high chemical

and biological durability, low density and low cost (that is why it finds extensive use in the modern society), most of the plastics ever made have been subjected to incorrect waste disposal at the end of their useful life. As stated earlier, the plastic waste debris dispersed in the environment tends to accumulate in the ocean, where they cause severe problems to the marine species and the ocean-related anthropogenic activities [4,8,9].

There is not a standard classification for the plastic debris present in the ocean. However, plastics debris can be roughly classified by size: mega-debris (> 100 mm), macro-debris (> 20 mm), meso-debris (20-5 mm) and micro-debris (< 5 mm) [10]. This latter group is defined as microplastics by the GESAMP (Joint Group of Experts on the Scientific Aspects of Marine Environmental Protection), an Inter-Agency Body of the United Nations (UN) [11]. GESAMP recognizes two types of microplastics, the so-called primary and secondary microplastics. The primary microplastics are small (5 mm) plastic particles that are deliberately manufactured in that size, such as those found in cosmetics, personal care products and industrial abrasive products. Secondary microplastics are generated by the mechanical breakdown of macroplastics [11].

The negative impact of microplastics in the marine environment has been investigated worldwide. It is currently known that microplastics ingested by wildlife generate plastics-derived toxins that enter the trophic web, leading to significant risks to animals and humans [12,13]. Additionally, it has been reported that microplastics can carry invasive species promoting the alteration of local

ecosystems [14]. For these reasons, microplastics have been recognized as an emerging issue.

In the last decade, the monitoring, identification, and quantification of microplastics has been extensively documented. Most of these studies have been carried out in marine environments from America, Europe, Oceania and Asia [10,15]. All this information provides a global perspective regarding microplastic pollution. However, to date, limited efforts have been conducted to reduce microplastics inputs from inland into the oceans. Some examples include reducing plastic mega-debris waste generation, recycling and development of biodegradable plastics.

Photocatalysis is a reliable technology that has been investigated to provide practical application and products for environmental solutions [16]. This technology has proved to degrade, in short time periods, a wide array of pollutants such as dyes, organics, medicines and plastics, to name a few. Thus, photocatalysis can be used to reduce microplastic waste inputs from inland into the oceans. For example, photocatalysis technology can be adapted to a Waste Water Treatment Plant (WWTP) [17] to reduce or eliminate microplastic pollution from the wastewater effluents. This process is initiated when a semiconductor such as titanium dioxide (TiO_2) is irradiated with a photon with $hv \geq E_g$ (where E_g is the band-gap of the semiconductor). Holes (h^+) - electron (e^-) pairs are formed and transferred to the photocatalyst's surface; if these holes are trapped either by water (H_2O) or hydroxyl groups (OH^-), hydroxyl radicals ($OH^\bullet$) are generated.

Hydroxyl radicals are powerful and indiscriminate oxidizing agents that effectively degrade an extensive range of organic pollutants into H_2O and CO_2 [18–20]. A widely used semiconductor is TiO_2 because it has several applications and excellent properties including strong oxidizing abilities, nontoxicity, environmentally benign and low cost [21,22]. As a disadvantage, TiO_2 is only active in presence of UV light (λ = 200 – 400 nm) [23], but some modifications such as doping with nitrogen have been made to activate TiO_2 in visible light (λ = 400 – 700 nm). An additional disadvantage of nitrogen doping of TiO_2 is that the synthesis routes used to dope TiO_2 require relatively high temperature post treatments [24].

Recently, some alternative low-cost and environmentally friendly routes to form TiO_2 semiconductors by means of biomineralization have been investigated [25]. This process involves the presence of a marine or freshwater mollusk such as the triangle sail mussel or ‘Karasu’ (in Japanese) *Hyriopsis cumingii*, which synthetizes biological calcareous compounds [26].

In this research, the photocatalytic degradation of polyethylene (PE) microplastics with a nitrogen-doped TiO_2 semiconductor was investigated as an attractive alternative for microplastic pollution remediation. Photocatalysis technology was chosen because it is considered an environmentally friendly process that follows two of the twelve principles of green chemistry.

CHAPTER 2

2. PROBLEM STATEMENT

2.1 Plastic and microplastic pollution.

Plastic is a synthetic polymer formed by monomers derived from oil and gas [13]. It has transformed our daily life since the beginning of its production in ~1950 because of its valuable characteristics. Plastic possesses high durability, low density, and low cost, and these features make plastic very attractive for a wide range of uses, from medical applications to food safety.

Packaging is the largest market for plastics: 40% of plastic production is used to single-use containers which are commonly for food safety and other applications [9,27]. The most common plastics used in the packaging sector are polyethylene (PE) with low and high density (LDPE and HDPE, respectively), polystyrene (PS), polypropylene (PP), poly (ethylene terephthalate) (PET), and poly (vinyl chloride) (PVC) [28].

With the increasing demand for plastic products, their production rapidly grew in the last decades [9,29,30]. As a result, the most updated estimations

indicated 8300 million metric tons of virgin plastics globally produced in 2015 [9]. In the case of Mexico, the production value for the plastic and rubber industry in 2016 was estimated in 228 billions Mexican pesos [31].

Even though plastic is a wonderful material that has enormously contributed to the society's wellness and technologic development, its extended use in the form of single-use products has led to the generation of large quantities of plastic waste. Indeed, recently the presence of plastic waste in the environment has been suggested as a geological indicator of the Anthropocene Era [32]. In 2015, it was estimated a global production of 6300 Mt of plastic waste. In the case of Mexico, only in 2017, almost five thousand tons (4,929) of urban plastic wastes were generated [31]. Due to the poor, and in some cases inexistent plastic waste management programs, only 9% of the plastic wastes were recycled, while 12% were incinerated, and the remaining 79% ended in landfills in the natural environment [9]. The problem with these disposal methods is that recycling does not avoid the final disposal of plastic residues [33], and their incineration produce dangerous gaseous components that finally impact the environment and all living forms [34]. Moreover, plastic residues ending in the landfills release toxic leachate because of the interaction with groundwater [35,36].

A problem derived from the incorrect disposal of plastic waste is microplastic pollution. In 2004, an investigation reported by Thompson et. al.[8] mentioned for the first time the presence of small plastic debris in the marine environment. The authors reported that these plastic fragments were present in marine ecosystems and explained their size by the mechanical fragmentation of

larger plastic items. The group called microplastics to these tiny plastic particles [8] and ever since, the scientific community had brought a lot of attention to this topic, trying to find the presence, distribution and sources of microplastics, and their effect on the environment.

There are thousands of worldwide reports of microplastic contamination from the poles to the equator. This accumulation of microplastics can be found in marine sediments, the water surface of the ocean, lakes, estuaries, the Arctic sea ice, the deep sea, and other environments [6]. Indeed, currently microplastics are considered a contaminant of emerging concern (CEC) [37]. The CECs are pollutants that have been detected in water bodies that may cause ecological or human health impacts, and typically are not regulated under current environmental laws.

2.1.1 Microplastics definitions.

Thompson uses the term *microplastics* to describe small plastic particles in a ranging diameter from a few microns to several millimeters; this term includes particles of several shapes (fibers, flakes, films, and spheres) and colors [6].

On the other hand, Rillig [38] defines *microplastics* as particles smaller than 1 mm, but also includes a range of several micrometers.

The simplest definition of microplastics was proposed by the Joint Group of Experts on the Scientific Aspects of the Marine Environment (GESAMP) and the United Nations Environmental Programme (UNEP) and is by far the most used

by researchers worldwide. According to GESAMP and UNEP, *microplastics* are particles of plastic <5 mm in diameter, sampled in the environment [30,39].

2.1.2 Primary and secondary microplastics.

As already mentioned, microplastics are classified into two types depending on their source, primary and secondary. Primary microplastics, directly released to the environment, are intentionally manufactured in a specific shape and size. They are used widely in industry and manufacturing. Some examples of primary microplastics include abrasives, personal care and cosmetic products (microbeads) [6,30]. **Figure 1** is portraits two personal care products that contain primary microplastics.

Secondary microplastics are formed from the fragmentation of larger plastic products and emerge by mechanical and environmental action. In the environment, the ultraviolet light from the sun, heat, wind, and ocean waves make possible the physical fragmentation of plastic items such as food and beverage packing. The use and weathering of some items also cause the mechanical fragmentation of plastics; for example, tire wears [6,14]. **Figure 1** also shows an example of the fragmentation of plastic that becomes secondary microplastics.

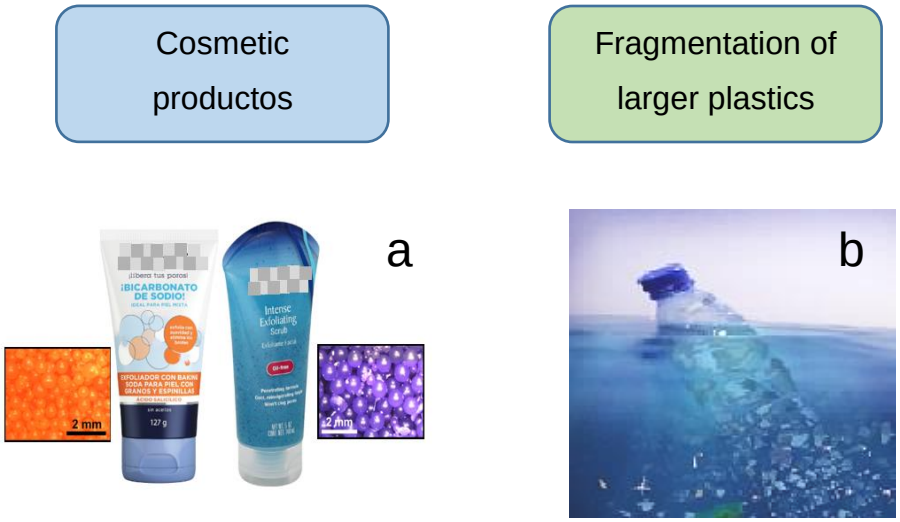

Figure 1. Example of primary (a) and secondary (b) microplastics.

2.1.3 The pathways of microplastics into the environment.

The presence of microplastics in the oceans is mostly originated from a variety of land-based sources. However, there are other entry points, such as rivers, coastal inputs, and the atmosphere [30,40].

Some primary microplastics sources are plastic pellets, industrial abrasives, injection powder, and 3D printing powders, which can get to the ocean by direct contact or by accidental or operational losses passing through WWTPs and waterways. On the other hand, there are personal care products composed of plastic microbeads, that after being used, are instantly released to drainage and go through WWTPs, arrive to a waterway and finally to the ocean [30].

Some of the sectors that cause secondary microplastic pollution are tourism industry, food and drinking retail, households, terrestrial transportation, plastic recyclers, constructions, and agriculture. The release of these microplastics occurs because of the fragmentation of packing, pots, pipes, tire wear dust, and washing fibers [30]. **Figure 2** shows some incorporation of microplastics into aquatic systems.

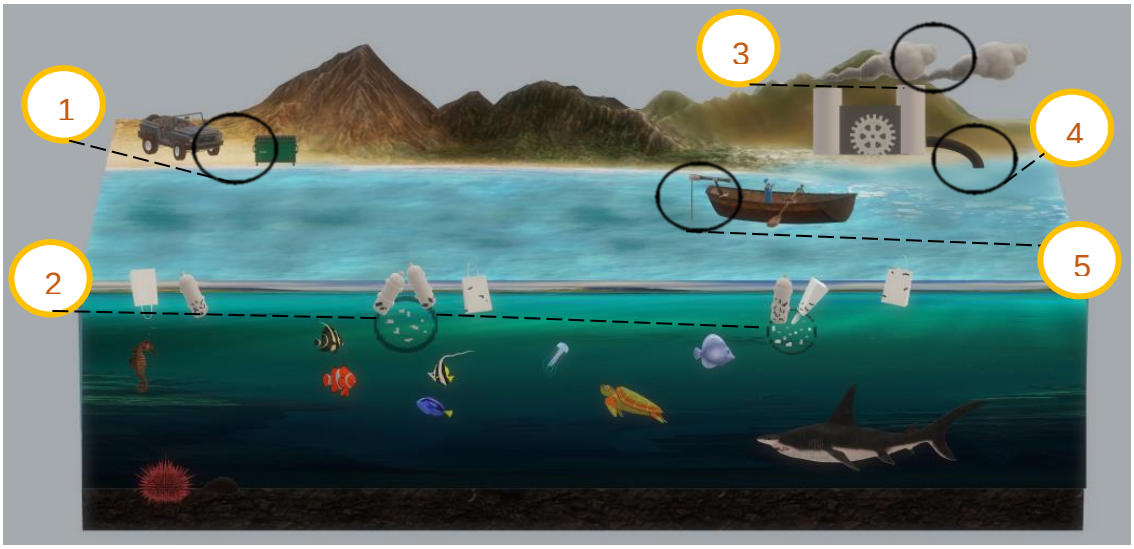

Figure 2. The entrance of microplastics to the environment. (1) fragmentation of tire wears and littering, (2) fragmentation of larger plastics, (3) atmospheric release and dispersion by wind, (4) sewage, and (5) illegal waste dumping. (Figure made by author).

In contrast with the marine systems, there are significantly fewer reports of incorporation of microplastics on terrestrial ecosystems. **Figure 2** illustrates some input paths of microplastics, for example littering along the roads and trails (1 and

2), atmospheric release (3), compost, sewage (4), sludge, and illegal waste dumping (5) [41].

Once microplastics are incorporated to the environment this are easily transported. Microplastics can travel driven by the wind, waves, ocean currents, and terrestrial or aquatic animals. Even if a small amount of plastics or microplastics is released in a specific area, it can travel thousands of kilometers. For example, microplastic released in the United Kingdom can be transported and arrive in other regions or countries [42,43].

2.1.4 Effects of microplastics in marine environments and their biota.

Currently, it is well known the negative impact of microplastics in the marine environment. It has been documented that a wide range of marine vertebrates and invertebrates such as zooplankton, seagulls, fishes, whales and turtles ingest microplastics, which cause them chemical and physical harm [14]. Due to the chemical surface characteristics of microplastics, these adsorb toxins, heavy metals, or persistent organic pollutants (POPs). When these ‘polluted’ microplastics are ingested by marine fauna, the adsorbed hazardous chemicals enter into the trophic web and eventually bioaccumulate, leading to significant risks such as bio-magnification and bio-amplification of toxic compounds, that ultimately affect the health of animals and humans [1,12–14,36,44].

Additionally, microplastics can carry invasive species promoting the alteration of local ecosystems, by the transportation of algal blooms and

pathogens [40]. The accumulation of microplastics (PVC and PET) in the seabed promotes the loss of ecosystem services, by preventing gas-exchange and creating hard-ground [13,45].

2.1.5 Effects of microplastics in terrestrial environments and their biota.

There are only a few studies about the effects, monitoring, and distribution of microplastics in continental ecosystems. Even though the ocean and soil are undoubtedly different, the ground contains many characteristics of aquatic systems. Microplastics can be ingested by micro and mesofauna such as earthworms, terrestrial snail and birds, and this led to an accumulation of microplastics in the soil detrital food web [38,46].

One of the linked mechanical impacts between the aquatic and the terrestrial is the influence of microplastics in the geochemistry and ecotoxicology [47]. Some of the hypothesized effects of microplastics on plants are the alteration of soil structure, nutrient immobilization, contaminant transport or adsorption, direct toxicity, and change of microbial communities in soil and root symbionts [48].

For all the previous discussed reasons, microplastics have been recognized as an emerging issue and there is an imperative need for the searching of technologies to reduce or eliminate microplastic pollution.

2.1.6 Current strategies for fighting microplastic pollution.

There are currently some waste-reduction strategies that are being internationally adopted to reduce the use of single-use plastics, and consequently, to reduce microplastic pollution. For example, some countries have banned the use of plastics bags and promote the usage of reusable shopping bags. These strategies can be useful for partially reducing plastic waste and environmental pollution caused by secondary microplastics. Regarding primary microplastics, there are some attempts in different countries to ban the use of plastic microbeads in cosmetics and personal care products [49]. Although these strategies can partially contribute to the reduction of microplastic pollution, they should be adopted for all, or at least, for most of the countries where those products are used to allow a real impact in the fight against this pollutant. As presented in Section 2.1.3, when microplastics are introduced into the environment, they can travel from their origin source to other places in the same country or even to different continents. Then, the plastic waste reduction politics taken by one particular state may have only a small influence in the global microplastic pollution issue.

Another strategy to fight microplastic pollution is creating public awareness about microplastics and their environmental consequences through education at the public, private, and government sector [14,50]. It is also recommended to incorporate ocean education, and waste management in different school programs to reduce plastic consumption [49]. However, this is a long-term

strategy that will take several years to make a significant impact on society and the environment.

One possible alternative to fight microplastic pollution in terrestrial ecosystems is the use of bacteria from earthworm *Lumbricus terrestris*. Lwanga et al. 2018 reported that bacteria could decay and reduce the size of low-density polyethylene (LDPE) microplastics [51]. A disadvantage of this method is that the worm generates several volatile compounds as byproducts, including octadecane, eicosane, docosane, and tricosane. The effects of these byproducts in the different terrestrial interaction (microbe-microbe and microbe-plant) remain largely unknown [51].

A probable short-term solution could be the WWTPs capable of capturing microplastics. Although these facilities are common in developed countries, there are absent or without advance technology in many developing countries [30,52].

As can be inferred from the information presented in this Chapter, there is a research gap within the field of microplastic pollution remediation. Similarly, the current fighting strategies against this problem present technological or social limitations, leading to the increase of microplastic pollution of marine and terrestrial environments.

One of the advantages of photocatalysis is that it has already proved to breakdown a wide variety of toxic or hazardous pollutants into less harmful molecules, such as CO_2 and water (a process called mineralization). Although CO_2 is a greenhouse gas, it is currently possible to capture this compound and

transform it into other products of technological interest such as low carbon fuels or chemicals for the industry. A second advantage of photocatalysis is that this technology can be easily adapted to WWTPs in developing countries by adding one step on the wastewater treatment process, making possible to reduce and/or eliminate microplastic pollution from the wastewater effluents before releasing them into the environment.

Finally, visible-light photocatalysis has the advantage of being considered a sustainable process that respects two of the twelve principles of green chemistry. In this case, our process will respect the principle number six, which is related to the rational use of energy. This will be done by (i) the generation of a semiconductor active in visible light (and hypothetically active in solar light) by (ii) a synthetic method conducted at ambient temperature and pressure, called biomineralization. The second principle that photocatalysis endorses is the number nine, which is associated with the use of a catalyst to make more efficient a process [53]. Therefore, in this work, visible-light photocatalysis is proposed as an attractive and “green” alternative to degrade microplastics and by a synthesis method call biomineralization using pearl oyster to enhance the properties of the photocatalyst.

CHAPTER 3

3. STATE OF THE ART AND CRITICAL ANALAYSIS OF THE LITERATURE

3.1 Photocatalysis of plastics.

Semiconductors obtained by several synthesis routes can be used to photocatalytically degrade a wide variety of liquid, solid or gaseous organic pollutants [54–60]. However, photocatalysis has been only scarcely used to degrade synthetic polymers such as polyethylene (PE).

Zhao et al. [61] investigated the photocatalytic degradation of PE plastic under ambient sunlight irradiation with copper phthalocyanine (CuPc) modified TiO_2 (TiO_2/CuPc) with an absorption range from 480 to 800 nm, with a proportion of 80% of anatase and 20% of rutile. In their study, composite films of PE-TiO_2 and PE/TiO_2/CuPc were exposed to sunlight for 160 h every sunny day. They authors reported that PE/TiO_2/CuPc exhibit a higher degradation rate and yield a PE weight loss of 36%. They also demonstrated that the photocatalytic reaction

of PE-TiO_2 and PE-TiO_2/CuPc films produced volatile mass products and led to polymer bond scission. This work was tested only in the solid phase, and it had low weight loss after long light exposure, which may occur due to the synthesis route (metal doping).

Fa et al. tested the photocatalytic degradation of PE-TiO_2 nanocomposite films with oxidize polyethylene wax (PE-OPW-TiO_2), they reported a good dispersion on the film, an absorption descends under 400 nm. These films were exposed to UV or solar light irradiation in ambient air for 120 h. They confirm that OPW, improve the dispersant and compatibility of TiO_2 in PE. After irradiation, the average molecular weight of PE-OPW-TiO_2 composite film decreased by 94.3% [62]. The disadvantage of using film is the low contact between the semiconductor and the contaminant.

Thomas et al. [63] studied the photocatalytic degradation of PE using PE/TiO_2 composite films under ultraviolet irradiation in ambient air for 200 h. The PE/TiO_2 films had an absorption value around 200-350 nm, with a crystalline anatase structure. The photocatalytic degradation of PE and PE-TiO_2 nanocomposite films were analyzed by weight loss, scanning electron microscope (SEM) and Fourier transform infrared spectrometer (FTIR). In this case the percentage of weight loss for the nanocomposite films of 18%. It was also observed the formation of the carbonyl index after exposure, confirming the efficiency of using Titania nanoparticles (TiO_2) for plastic degradation. In this work, the limited bad gap (3.08 eV.) of TiO_2 show an application restriction, also it was needed a long light exposure to obtain low weight, and the photocatalysis was

tested only in solid phase. The disadvantage of using film is the little contact between the semiconductor and the contaminant.

The works presented in this section have demonstrated that TiO_2 or TiO_2-based semiconductors can be used to degrade PE macro-plastics. For these particular cases, the semiconductor was dispersed in a PE matrix using organic solvents to solubilize the PE, resulting in a PE/Semiconductor film composite with limited contact between the semiconductor and the contaminant. Additionally, the use of organic solvents is undesirable in the searching of microplastic pollution remediation technologies that, as stated before, should potentially reduce the environmental impacts.

3.2 Photocatalysis of microplastics.

Photocatalysis of microplastics is a new field that was first reported in 2018 by our research group. Ariza-Tarazona et al. for example, reported the use of a bio-inspired porous N-TiO_2 for the photocatalytical degradation of primary HDPE microplastics extracted from a commercial facial scrub. The semiconductor was prepared by a hydrothermal route at 150 ºC/12 h using titanium butoxide as TiO_2 precursor and proteins from *Mytilus edulis* mussels as nitrogen dopant source. The semiconductor composed of anatase doped with nitrogen, was able to absorb visible light of 427 nm, and had a particle size between 5 and 10 nm diameter. The photocatalysis was carried out using HDPE/N-TiO_2 composites (prepared using cyclohexane solvent) in solid (25 ºC and 50 % relative humidity) and

aqueous (25 ºC, pH = 7) environments with light between 400 - 700 nm [64]. After degradation, the mass loss, FTIR, and SEM results revealed that up to 7% of the original plastic was degraded in only 20 h of irradiation in the aqueous environment. The principal limitation of this work was that photocatalysis was arrested after 20 h radiation, and this phenomenon was attributed to the limited contact between the semiconductor and the HDPE in the plastic matrix. It was hypothesized that the semiconductor in the plastic matrix presents a limited porosity and consequently, a low surface area that lead to limited degradation.

Tofa et al. [65], tested microplastic degradation of LDPE with Zinc oxide (ZnO) nanorods that was synthesized by a hydrothermal method that required 350 °C for 1 h. The deterioration of LDPE was carried out in a petri dish containing water deionized and the photocatalyst for 175 h with visible light illumination in ambient air. The semiconductor presented a surface area of 6.5, 22, 49 and 55 cm^3. These authors did not report a mass loss; however, the changes in viscoelastic properties of LDPE and the carbonyl and vinyl indices were reported. The formation of low weight compounds and cracks on the LDPE surface was reported, together with an increase of 30% in the carbonyl index, and inherent chromophoric groups as initiators of degradation. This synthesis requires a hydrothermal treatment (350 °C), and the results are only reflected in the carbonyl and vinyl index.

The same research group in the same year [66] used ZnO with a deposit of platinum (ZnO-Pt) to follow the degradation of LDPE films for 175 h. The synthesis was made by a hydrothermal process at 90 °C and after an annealed

in ambiental conditions at 350°C for 1 h. The average diameter and length of ZnO-Pt were estimated to be 55 µm and 960 µm, and the absorbance spectra were recorder over 385 to 750 nm. It was compared the chemical composition of LDPE by FTIR analysis finding new functional groups after irradiation which suggest photodegradation. Also, the carbonyl and vinyl index were measured, and it was shown an increase by 13% and 15% respectively. Visual observation verified cavities and wrinkles in microplastics after photocatalysis. This study does not report a mass loss, and the synthesis method require a hydrothermal treatment.

In 2019 and 2020, Ariza-Tarazona et al. [67] test microplastic degradation of HDPE in different environmental conditions in the aqueous and solid phase. The main variables were temperature and pH, testing condition of 0, 20, and 40 °C with a pH of 3, 7, and 11. The semiconductor used was N-TiO_2 synthesized by a bio-inspired rout, were anatase phase, the nitrogen dopant and an absorption value of 427 nm was confirmed. The result stated that after 50 h the higher degradation was obtained in conditions of 0 °C and pH 3 that show a loss weight of 72.3%, and in contrast, the lowest degradation was obtained with 20 °C and pH 7 with a weight loss of 0.11%. These results showed that the semiconductor N-TiO_2 is an effective method to degrade HDPE obtained from commercial scrubs. However, it is needed extreme environmental conditions (low temperature of 0 °C and pH 3) to archived functional degradation, which limits its practical application.

From the previous reports, it appears that some progress in the remediation of microplastic pollution by photocatalysis in aqueous environments

have been made. However, there are two major gaps in this field. The first one is the lack of reports dealing with the effect of microplastic's particle size in the photocatalytic degradation process. As previously stated, the GESAMP and UNEP definition for microplastics include a wide range of particle sizes (from few microns up to 5 mm). Photocatalysis is a surface-related phenomenon where the interaction between the semiconductor and the pollutant is key during degradation, being the particle size the factor governing the effective interaction area between the components. Thus, the influence of the microplastic's particle size in the degradation process may not be negligible and should be taken into account to design an efficient degradation process.

The second gap involves the use of relatively high energy-consuming synthesis routes (thermal treatment 350 °C) for the semiconductors applied in the degradation of microplastics. The current trend in the development of strategies for pollution remediation dictates that the environmental impacts associated with the remediation process must be as lower as possible. In this regard, the previous reports of Ariza-Tarazona et al. show that the only approach that have been used to reduce the energy consumed during the synthesis of the semiconductor is a hydrothermal route at 150 ºC/12 h. However, even this route requires heating for a relatively long period of time. Thus, searching for synthesis routes of TiO_2 or TiO_2-based semiconductors should be done to reduce the environmental impact of the photocatalytic remediation of microplastic pollution.

In this thesis work, the previous gaps were fulfilled by (i) using the biomineralization synthesis procedure to obtain a TiO_2-based semiconductor

through a low energy-consumption process called biomineralization and (ii) by carrying out photocatalysis using two primary HDPE microplastics of different particle sizes. As there are no reports regarding the effect of microplastic's size in the photocatalytic process, the next section only presents the works that have been conducted to biomineralize TiO_2-based materials.

3.3 Biomineralization of semiconductors.

Xie et al. [25] evaluated the direct implantation or pasting of an amorphous TiO_2 precursor (in the form of a tablet) into living freshwater mussels *Cristaria plicata* at room temperature. The fundament of the synthesis process relies on a natural process occurring in all mollusk species called 'biomineralization' relative to the formation of all components of the shell, including the external (periostracum), middle (prismatic layer) and internal (nacre layer) (Fougerouse et al. 2008; Awaji and Machii 2011). The synthesis procedure was designed based in the pearl cultivation process, as *C. plicata* has been previously used to biomineralize artificial pearls. The authors found that after mineralization in the mussel's body for 15 – 90 days, the amorphous TiO_2 precursor was transformed into N-doped anatase TiO_2 with a hierarchical porous microstructure after day 60. In other words, the living mussels acted as a "reaction chamber" where the disordered atoms of the amorphous TiO_2 material were rearranged into its anatase crystalline form; and where nitrogen was incorporated into the crystal structure during mineralization. The incorporation of nitrogen in the TiO_2

microstructure and the presence of hierarchical porosity in the final materials was explained by the interaction of the amorphous TiO_2 with the intracellular proteins of the mussels. On the other hand, the crystallization of TiO_2 was attributed to the intracellular proteins which directed the amorphous-anatase transition of the semiconductor.

Regarding the photocatalytic properties of the biomineralized material, authors reported that the N-TiO_2 incubated for 90 days had a superficial area of 206 $m^2 g^{-1}$ and a pore volume of 0.22 $m^3 g^{-1}$ with a hierarchically porous structure that improved the photocatalytic activity. The synthesized N-TiO_2 displayed an improved photocatalytic activity in visible-light reporting absorption from 380 – 650 nm owing to the nitrogen doping and exhibit superior degradation of RhB that pristine TiO_2.

The analysis of the previous work revealed that there has been only one effort to obtain a visible-active semiconductor by the low energy-consuming biomineralization process using a Chinese freshwater pearl mussel. However, other bivalve species of commercial interest or that are already used in pearl cultivation have not been tested for semiconductor obtainment. Therefore, there is a research gap for the determination of the ability of bivalve pearl-forming species other than *C. plicata* for production visible-active semiconductors. To fill this gap, the Mexican pearl oyster *Pteria sterna*, which is already used in commercial pearl cultivation in Mexico, was tested for the obtainment of a crystalline N-TiO_2 semiconductor.

CHAPTER 4

4. HYPOTHESIS AND OBJECTIVES

4.1 Hypothesis.

The N-TiO_2 semiconductor obtained by a natural biomineralization process within a Mexican pearl-forming oyster will photocatalytically degrade PE microplastics in an aqueous environment.

4.2 General objective.

Evaluate the reliability of an N-TiO_2 semiconductor formed by biomineralization within one Mexican pearl-forming oyster and test the photocatalytic properties of the obtained material for the degradation of PE microplastics in an aqueous environment.

4.3 Specific objectives.

1. Synthetize an N-TiO_2 semiconductor through biomineralization using the wing pearl oyster *Pteria sterna*.
2. Characterize the biomineralized semiconductor in terms of crystallographic composition, chemical composition, light absorption properties and microstructure and morphological characteristics.
3. Evaluate the photocatalytic degradation of PE microplastics in an aqueous medium using the N-TiO_2 semiconductor synthesized by biomineralization.

4.4 Scientific contribution.

Use of one pearl-forming Mexican pearl oyster for the synthesis of N-TiO2 semiconductors, as well their application for the photocatalytic degradation of polyethylene (PE) microplastics in an aqueous medium.

.

CHAPTER 5

5. THEORETICAL FRAMEWORK

In this Chapter, the theoretical framework of all the physicochemical phenomena involved in this thesis research is presented.

5.1 Photocatalysis.

Photocatalysis is defined as a photochemical reaction at a solid surface in presence of a catalyst, usually a semiconductor, and light. Since the early 70's, photocatalysis has been investigated to be applied in the development of new technologies such as environmental bioremediation, alternative green energy, self-cleaning materials, and wastewater treatment [68,69].

Photocatalysis is based in the interaction of a semiconductor with a pollutant adsorbed on its surface and light, as presented in **Figure 3**.

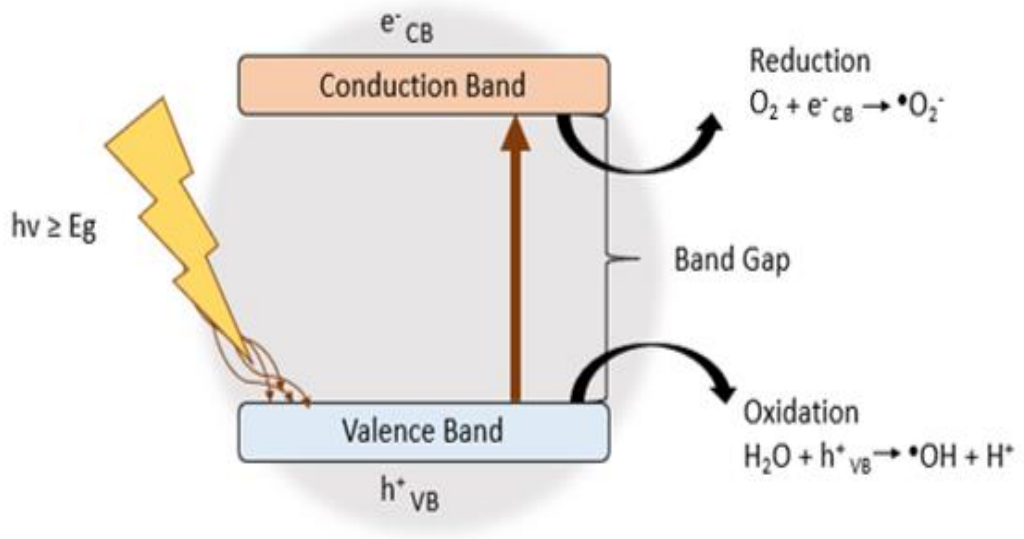

Figure 3. Mechanism of photocatalysis. The scheme took from Byrne et al., [70].

When the semiconductor is bombarded with photons with energy equal or higher than its band gap ($E \geq E_g$); the electrons (e^-) on the valance band are transferred into the conduction band, leaving behind a positive hole (h^+) (Equation 1) [71]

$$TiO_2 \xrightarrow{hv} e^-_{CB} + h^+_{VB} \qquad \text{Equation 1}$$

After separation of the electron-hole pair, if each one separately migrates to the surface, a reaction of reduction or oxidation can successfully occur. The holes react with water in a liquid or vapor state or hydroxyl groups adsorbed in the surface of the semiconductor, generating hydroxyl radicals ($OH^•$) (Equation (1.1) [71]

$$h^+ + H_2O_{ads} \rightarrow OH^{\bullet}_{ads} + H^+$$ Equation 1.1

The hydroxyl radicals can be detached from the surface and interact with molecules in the bulk of the solution, whereas direct capture of holes requires adsorption of the donor species [72]. Electrons react with adsorbed oxygen to form superoxide anion radicals ($O_2^{-\bullet}$) [73,74], this phenomena is shown in Equation 1.2 [71].

$$e^-_{CB,surf} + O_{2(ads)} \rightarrow O_2^{\bullet -}$$ Equation 1.2

From hydrogen ions or water molecules the protons are transferred to the superoxide molecules, these yields the neutral hydroperoxyl radical $HO_2^{\bullet}$

$$O_2^{\bullet -} + H^+ \rightarrow HO_2^{\bullet}$$ Equation 1.3

To produce hydrogen peroxide H_2O_2 the hydroperoxyl radical reacts with the superoxide molecules and hydrogen ions. Superoxide and hydroperoxyl radicals are reactive oxygen species (ROS) and are essential in degradation.

$$H^+ + O_2^- + HO_2^{\bullet} \rightarrow H_2O_2 + O_2^{\bullet}$$ Equation 1.4

Photoconversion of hydrogen peroxide gives more $OH^{\bullet}$ free radical groups.

$$H_2O_2 + hv \rightarrow H_2O_2 + hv \rightarrow 2\ \ OH^{\bullet}$$ Equation 1.5

In the surface of the titanium dioxide particles the $OH^{\bullet}$ radicals oxidize organic adsorbed pollutants (RX_{ad}).

$$OH_{ad}^{-} + RX_{ad} \rightarrow Intermediates \qquad \text{Equation 1.6}$$

Because of the reactivity of the $OH^{\bullet}$ radicals, they attack the molecules of the pollutant, carrying out the degradation into simpler or less hazardous molecules or mineralize it into carbon dioxide and water and the eventual mineral acids [68,71,75].

The reduction or oxidative abilities are determined by the energy level at the conduction and valence band. The efficiency of the process can be limited by the e^{-} – h^{+} pair recombination, which wastes the photon energy necessary for the reaction [68].

5.2 Semiconductors.

Semiconductor materials are neither fully conductor nor insulators. The energy gap for electronic excitations lies between zero and about four electron volts (eV). This means that the band-gap of semiconductors is more than of conductor and less that of insulators [76,77].

The electronic structure of a semiconductor consists of a valence band filled with electrons while the conduction band is empty, this has a significant

influence on its photocatalytic performances. This characteristic allows the semiconductors to act as sensitizers for light-reduced redox processes. A photon with a higher or equal energy of the semiconductor's band-gap can promote an electron from the valence band, into the conduction band, leaving a hole behind [78].

Another characteristic of semiconductors is that their electronic properties can be modified by the controlled addition of impurities known as dopants. The doping of semiconductor for photocatalysis is considered a viable alternative to improve visible light absorption and yields new properties [79].

A semiconductor photocatalyst needs a list of characteristics to be considered an ideal material. It should be chemical and biological inert (nontoxicity), easy of prepare, low cost, be activated by sunlight, and have long term stability and photocatalytical activity (strong oxidative) [70,80].

There are several semiconductors with different properties used in photocatalysis, but as already stated, an ideal photocatalyst does not exist. **Table 1** shows some photocatalytic semiconductors used for photocatalysis [81].

Table 1. Conventional photocatalytic semiconductors, band-gap energy, and the corresponding absorption edge.

Semiconductor	Band gap (eV)	Absorption edge (nm)
TiO_2	3.2	388
ZnO	3.2	388
WO_3	2.8	443
Fe_2O_3	2.3	539
Cu_2O	2.0 – 2.2	564 – 620
Fe-TiO_2	2.97	417
Ag-TiO_2	3.2	388
N-TiO_2	2.8	443
C-TiO_2	3.0	413

Titanium dioxide (TiO_2) is close to reaching all the criteria for an ideal semiconductor and it is well known that TiO_2 has a lot of properties that make it the most attractive photocatalyst. Some of these characteristics are the wide operating pH range, is biologically inert, environmentally benign, biocompatible, highly stable, available, and a low-cost metal oxide photocatalyst that can degrade a spectrum of contaminants efficiently [70].

5.2.1 TiO_2 photocatalyst.

TiO_2 have three different well-known crystalline phases: rutile, anatase, and brookite. The three types are composed of octahedra (TiO_6,) but with various distortions.

All three phases have different characteristics because of the Ti-O bond. For instance, the most stable phase is rutile, yet anatase is the most photoactive phase. The difference between them provides a useful application in diverse fields. For photocatalysis proposes anatase and rutile phase are used, but anatase is preferred because it improves charge-carrier mobility and the higher number of surface hydroxyl group [75].

The biggest disadvantage of anatase TiO_2 is its large band-gap [82]. To address this problem, researchers started to consider the doping TiO_2 with non-metal atoms such as nitrogen, carbon, sulphur, phosphorous, boron, oxygen, fluorine and combinations of these elements to obtain visible light photoactivity [83]. Doping TiO_2 modifies the semiconductor energy band-gap effectively and accelerate electron-hole separation. Similarly, it can lead to a redshift in the optical absorption edge of TiO_2 to lower energy, leading to an improvement in the photocatalytic activity under visible light [84].

The doping of TiO_2 with nitrogen (N-TiO_2) is one of the most studied system [69] to address the problem of the restrictive photoactivity, researchers started to consider the doping TiO_2 with non-metal atoms in order to obtain visible light photoactivity.

There are different types of synthesis routes for the obtainment of TiO_2 or visible-active TiO_2-doped materials. The sol-gel method is one of the most used because it allows the preparation of semiconductors in the form of powders and films. It involves a relatively simple procedure, not requiring sophisticated equipment and enabling control of the final characteristics of the product by modification of the precursor solution [85,86].

Usually, sol-gel synthesis routes are considered as "environmentally friendly" because of the use of post-heating thermal treatments at relatively low temperatures, which allow crystallization of the TiO_2 photocatalytic phases. However, depending of the desired characteristics of the semiconductor or the specific photocatalysts targeted, thermal treatments at temperatures up to 600 ºC are needed.

As stated earlier, the current trends in semiconductor design involves the development of low-energy consumption synthesis procedures. In this work, the biomineralization process using pearl-forming oysters was investigated for the crystallization and doping of an amorphous TiO_2 semiconductor. To understand this process, Section 5.2 presents a brief summary regarding the differences between amorphous and crystalline materials, and Section 5.3 presents the known fundamentals of biomineralization.

5.3 Crystalline and amorphous solids.

Solids can be amorphous or crystalline. It is considered a crystalline solid when it contains a rigid lattice of molecules, atoms or ions at a specific location. In other words, a crystalline material contains billions of unit cells, which periodically repeat in all three dimensions, and these arrangements are characteristics for every material. The crystals have a regularity in their internal structure that results in characteristic crystal shape, surface, grow, and planes [87].

An amorphous solid presents a random arrangement of their molecules, while the regular order of molecules in crystalline solids allow most of them to have mechanical, electrical, magnetic or optical proprieties according to the direction in which is measured these proprieties can vary. These enhanced properties make the crystalline solids an exciting topic for research to develop new technologies as solutions to some modern problems [87].

Amorphous solids can be subjected to the rearrangement of their atoms to become crystalline. Thermal methods are typically applied to crystallize the amorphous solids. These methods require a considerable quantity of energy due to high operating temperatures. The crystallization temperature is the temperature at which an amophous solid crystalize. The amount of temperature in the form of energy plays a crucial role in the final morphology of the crystalline structure. The crystallization temperature can vary depending on the material. Since some thermal treatments need ≥ 800°C for long time periods to obtain a crystallization,

finding better crystallization methods should involve the consumption of renewable energy [88].

5.3.1 Crystallization of solids by biomineralization.

The crystallization of solid materials by biomineralization is common in nature. This method allows some marine organisms, particularly those with calcareous structures (e.g. shell, spines), to accumulate and form minerals that eventually are transformed into biological structures or body tissues [89,90]. A good example of mineralization occurring in marine environments is bironite, the most stable carbonate dolomite obtained from marine calcareous environments, and in terms of chemical composition, has many similarities with calcium carbonate and with nacre [91].

In nature, it is well known that amorphous calcium carbonate (ACC) phase is a precursor for calcite and aragonite crystals. The chemical structure of these two inorganic compounds is the same ($CaCO_3$), yet the solid crystalline structures are different, as shown in **Figure 4**.

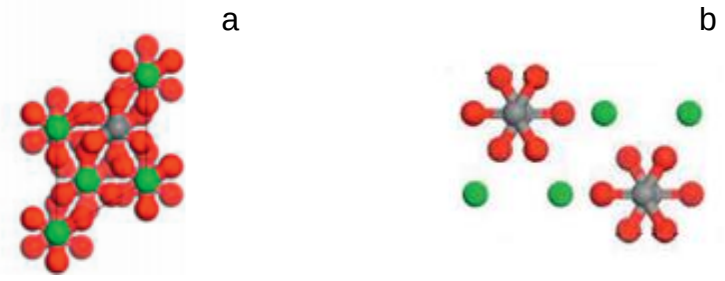

Figure 4. Calcite (a) and aragonite structure (b). Ca (green), O (red), and C (gray). Structures taken from Omair et al. [92].

Both compounds can be found in abundance in most marine and freshwater mollusks (e.g. oysters, mussels, scallops, clams, conchs, snails, abalone, etc.) and resembles a model of a brick wall (blue) and cement (red lines) (**Figure 5**). The figure resembles a model of construction; the polygonal crystals or aragonite are the bricks and the polysaccharide and protein framework orthogonally intermingled with the calcite crystals are the cement. Still, the molecular details of their mechanisms for nucleation and growth are still under investigation [90,93].

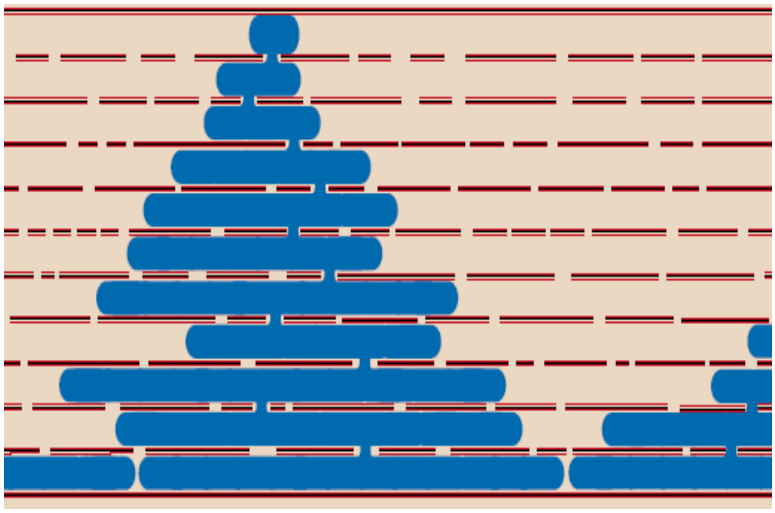

Figure 5. Architectural arrangement of the shell of a marine pearl oyster of the genus *Pinctada*, (Taken from Levi *et al.* [94]).

An advantage of the crystallization of solids by biomineralization is that it allows the organisms to obtain minerals from nature with the precise shape, texture, size, crystallinity, composition, and expansion factor at environmental temperature. If the biomineralization mechanisms are investigated and correctly

understood, they can led to the production of new materials for medical and other technological applications [95].

5.4 Biomineralization (fundamentals).

Biomineralization is the process by which minerals are directly formed by a living calcareous organism. This process is conducted by precipitation and reactions that convert ions taken from the environment into solid minerals within the animal's body tissues. Biomineralization involves the manipulation of the inorganic crystal nucleation, growth, and molecular arrangement to produce mineral with enhanced optical, mechanical or magnetic properties.

Biomineralization process is divided into two distinct categories, including biologically-induced and biologically-controlled. The Bio-induced biomineralization is more "primitive" and forms biominerals that usually lack a unique morphology and are disorganized and irregular. In contrast, in the bio-controlled biomineralization, the nucleation, growth, morphology and final location of the deposited minerals are directed by the cellular activities of the organism. This process occurs in an isolated environment, and the result is a specie-specific product that gives to the organism a specialized biological function.

The mechanisms of biomineralization are still under investigation because they are involved in different biological systems. This system is complex and has a vast diversity because each organism produces and exploits minerals with different purposes, and more than 60 different types of biominerals. The

composition of biominerals include calcium phosphate, calcium carbonate, and oxidation silicon [90]. This considerable diversity of forms having a different mechanism and final products [90].

Some examples of biominerals formations that have been identified are bones that support movement in vertebrates, shells that protect the soft tissue in bivalves, magnetosomes found in magnetotactic bacterial that allows them to perceive the changes of the geomagnetic field, raphides as a protective device in plants, otoliths in fishes for balancing movements [90,95].

In gastropods and bivalve (marine and freshwater) mollusks, the relevance of biomineralization is clearly represented in the formation of the shell. The shell is a hard structure that provides symmetry, support and protection to soft body tissues and allows the mollusk to grow. Growth, together with shell formation and repair, are strongly dependent on calcium ions ($CaCO_3$), which originate from calcium and bicarbonate present in the extrapallial fluid. All these ions are transported from the pallial cavity to the shell via the mantle tissue that acts as a repository of nutrients that are either stored and mobilized according to the needs of the mollusk [96].

Anatomically, mantle tissue is organized in three distinctive zones: marginal (formed by the external, middle, and internal lobes), pallial (or sub-marginal) and central [89]. In turn, the lobes from the marginal zone participate in forming the three constitutive layers of the shell, periostracum (external layer), mesostracum (middle layer), and endostracum (internal layer). The internal layer

gives the distinctive species-dependent micro-arrangement of calcite and aragonite compounds that display luster or opacity of the nacre layer [94,97].

Histologically, mantle tissue is formed by an internal and external covering epithelium separated by connective tissue layers, nerves, and collagen and muscle fibers [98]. In the marginal zone in particular, several kinds of cells with high enzymatic activity participate in the transport of ions ($CaCO_3$, calcite, aragonite), synthesis of polysaccharides and proteins (cochiolin) that participate in the formation of the shell and nacre. Nacre is the polymorphic arrangement most studied by man for cultivating pearls [89]. This marginal mantle also plays a key role in the defense mechanism of mollusks, which has also been imitated by man to develop the original grafting technique. This technique is aimed to provoke an injury to the mollusk receiving the nuclei and mantle allograft, under the assumption that the animal will respond secreting nacre to disable these external agents [93,94].

5.4.1 Biomineralization with pearl oysters.

Among mollusks, pearl oysters represent one of the best examples of biomineralization tied to the synthesis of nacre material during the process of pearl production [90,99,100]. The members of the genus *Pinctada* (*Pinctada fucata*, *P. margaritifera*, *P. maxima*) and *Pteria* (*Pteria penguin*, *P. sterna*) produce multicolor iridescent nacre that is highly valued in the pearling industry [101].

The mantle secreted complex calcified layers that are subdivided into the periostracum, prismatic, and nacreous layer that are shown in **Figure 6**.

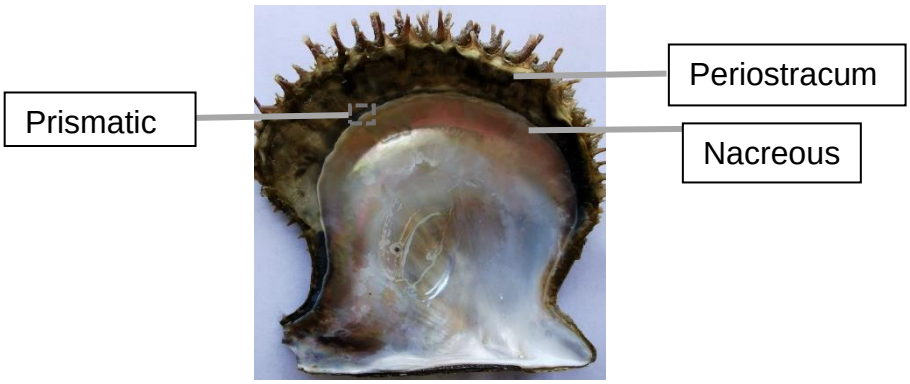

Figure 6. The shell of *Pteria sterna* and the layers subdivision.

In the black-lip pearl oyster (*P. margaritifera*), the nacreous layer is composed of aragonite tablets that regulate the formation and growth of the shell, as a result a light and resistant material is formed. There are six different types of crystal structures for $CaCO_3$, calcite, aragonite, vaterite, $CaCO_3 \cdot H_2O$, $CaCO_3 \cdot 6H_2O$ and amorphous calcium carbonate (ACC). This ACC is considered the precursor in shell formation, and the biomineralization involves the formation, destabilization and transformation of ACC, which is controlled by the organism [90]. Additionally, some pigments provide the structural and chromatic elements related to the hardness, opacity or bright of the nacre layer. In general, calcite prisms are black, while the nacreous layers are white [100]. Finally, the nacreous layer plays an essential role in enhancing mechanical properties by spreading the force in the aragonite and significantly improving the shell force [95].

Biomineralization in pearl oyster can be seen in the pearl and shell formation. The process of pearl formation in oysters involves nacre biomineralization which is very complex [99,102]. However, in general terms the process formation of the shell can be described in three steps, the first is the absorption of calcareous materials inside the organism, the second is the secretion from the mantle of the shell material and the third is the transformation of the secreted material into $CaCO_3$ crystals where the organic matrix help in the cementation of the crystals [103].

CHAPTER 6

6. EXPERIMENTAL PROCEDURES

Due to the relatively long processing times of biomineralization, the operational parameters for the photocatalytic tests were determined at the same time that biomineralization by using two semiconductors with the characteristics expected for the biomineralized materials.

A sol-gel derived and a hydrothermal derived porous N-TiO_2 semiconductors with anatase phase, high surface area and active in visible light were used to set the operational parameters that were used in the photocatalytic experiments with the biomineralized materials. Those parameters were the model pollutant (HDPE or LDPE), the shape (films or spheres) and size (two sizes for each one) of the pollutant and the semiconductor presentation (film or powders). The last parameter was tested because it is known that using coatings instead of powders avoids practical limitations in the eventuality of the scalation of photocatalysis for application in WWTPs.

6.1 Microplastics obtainment and characterization

Two types of microplastics were used in this work. The primary high-density polyethylene (HDPE) microplastics in form of beads were extracted from three different commercial facial scrubs according to the procedure reported by

Napper et al. [104]. For each brand, 500 ml of distilled boiling water and 60 g of the scrub were mixed and the solution was cooled down for a couple of minutes. The warm mixture was then filtered with a cloth filter with an approximated pore size of 500 µm. The microplastics obtained after filtration were repeatedly washed with distilled water, dried at 30 ºC for 24 h and stored until use.

The secondary low-density polyethylene (LDPE) microplastics in the form of films with dimensions of 5x5 cm and 3x3 cm were obtained by mechanical fragmentation of a commercially available LDPE plastic bag.

The shape and the size of the microplastics was evaluated by optical microscopy (OM) using a Leica ICC50 W camera incorporated in a Leica DME optical microscope (30 measurements). For the analysis of the polymer type and the functional groups present in the plastics, Fourier-transformed infrared spectroscopy (FTIR) was used in a BRUKER Alpha II spectrometer equipped with a diamond ATR accessory. The obtained spectra were compared to a spectral database of synthetic polymers. The crystalline microplastics were also analysed by X-ray diffraction, using a PANAlitycal X'Pert Pro diffractometer with Cu Kα1 radiation.

6.2 Biomineralization.

The biomineralization synthesis was performed following the methodology reported by Xie *et al.* [25] in the facilities of the commercial pearl farm *Perlas del Cortez S. de R.L. M.I*, located in Pichilingue, Baja California Sur, Mexico (**Figure**

7a). For incubation, the organisms were placed in a cage and sited in “the line”, as illustrated in **Figure 7b**.

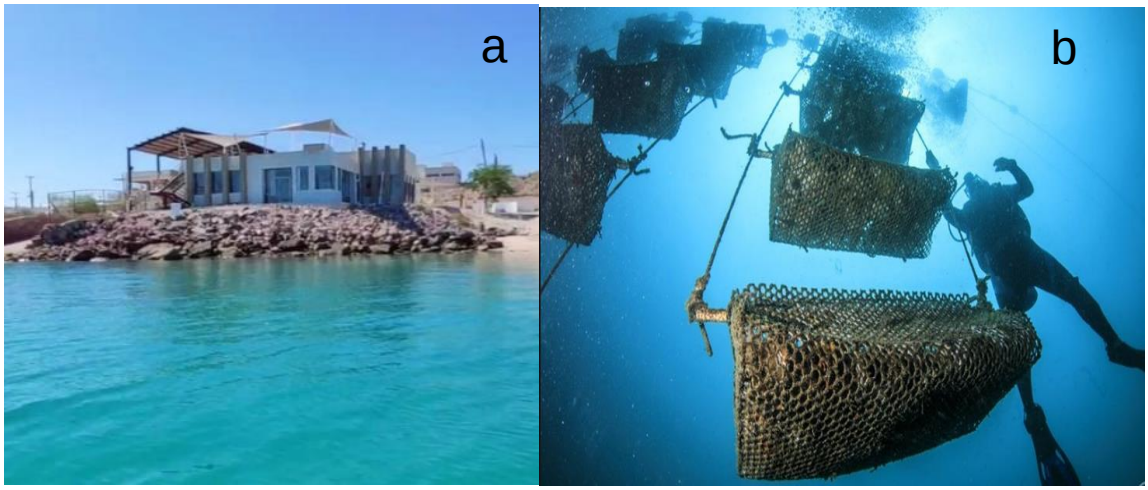

Figure 7. Facilities of *Perlas del Cortez* (a) and the line (b).

6.2.1 Amorphous TiO_2 obtainment.

The amorphous precursors of TiO_2 were prepared by a typical sol-gel method (without heat treatment for anatase crystallization) with titanium (IV) butoxide (TBT) (97%, Sigma Aldrich), ethanol (99.6%, Aldrich), and acetic acid glacial (99.8%, Aldrich). 5 mL of TBT were diluted in 20 mL of ethanol; after this, 1mL of acetic acid was added. The solution was kept in continuous stirring at 300 rpm for two h at room temperature; hereafter, a transparent homogenous gel was obtained. The gel was dried at 100 °C for 24 h, and the obtained yellow amorphous agglomerated powders were ground in an agate mortar. The amorphous powders (500 mg) were compressed using a mechanical press

CARVER, model 4350-L with a pressure of 18,000 Pa for 25 minutes to form the tablets. The amorphous TiO_2 precursor tablets had a diameter of 13 mm and a thickness of 3 mm.

6.2.2 Organism obtainment and characterization.

The pearl oyster specie (a marine bivalve) that was used was *Pteria sterna (P. sterna),* also called nacre shell. **Figure 8** shows the pearls oyster.

Figure 8. Pearls oyster *Pteria sterna*.

Sixteen organisms were purchased from the pearl farm *Perlas del Cortez S. de R.L. M.I*. This company owns permission from SEMARNAT to collect and use these organisms.

The individuals were viable juveniles with a size between 12 and 16 cm of high. The main characteristics of this specie include its small size, the wing shape

of the shell and the extensive range of colors of their nacreous shell. Their natural habitat distribution goes from the interior of the Gulf of California and the Pacific, going from Mexico to Peru.

The oysters were kept in their natural environment inside oyster pearl culture cages (**Figure 9a**), in the line of the pearl farms (**Figure 9b**).

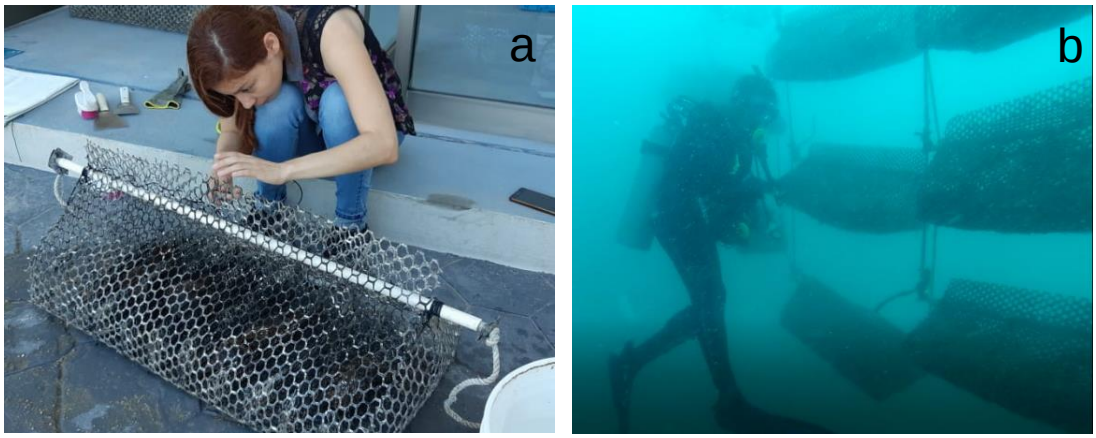

Figure 9. Culture cages (a) and the line were organism were kept (b).

6.2.3 Relaxation methodology.

Tablet implantation (or nucleus implantation in artificial pearl cultivation) is considered a surgical intervention and the organisms must be relaxed before being subjected to this process. Benzocaine was used to proceed with the relaxation of the organisms. Details regarding the concentration and dispersion medium are not presented due to industrial secret. The animals were submerged in the benzocaine solution between 20-30 minutes up to total relaxation. When the organisms started to show some indicators of looseness (slightly opening of the valves), the valves were carefully opened with a shell opener and a plastic

wedge was placed between the valves to encourage total relaxation of the animal, like illustrated in **Figure 10**. This procedure was made while the organisms were submerged in the benzocaine solution.

Figure 10. Relaxation methodology.

6.2.4 Tablet implantation.

After total relaxation of the organism, the mantle was distended. The mantle was retracted carefully to expose the nacreous layer and the whole layer of periostracum. Once these two layers were uncovered, a sponge was used to dry the area to proceed with the implantation. To attach the precursors tables to each organism, a commercial cyanoacrylate glue with a brush was used. Three precursor tablets were attached to each organism. The implantation was made between the nacreous and the periostracum layer (see **Figure 11**), placing two

tablets in different sites of one valve and if possible, another tablet in the center of the other valve.

Figure 11. Implantation of one precursor tablet.

After the attachment, the animals were kept in a recuperation chamber with warm saltwater (the chamber was exposed to natural solar light) until they were recovered from the relaxation. Afterwards, the organisms were returned to their natural environment inside a pearl oyster culture cage. The cage was placed in the pearl production line of the farm. The precursor tablets were incubated inside the *P. sterna* for 20, 32, 77, and 90 days.

6.2.5 Tablet extraction.

After incubation, the precursor tablets were extracted from the organisms. and the nacreous layer was removed from the biomineralized TiO_2 materials. Tablet extraction was made using two different approaches. In the first one, the animal was sacrificed in order to completely recover the tablet. This approach is

the one used in artificial pearl cultivation. In the second approach, the animal was relaxed using the procedure described in Section 6.2.2, and the nacreous layer was broken to recover the biomineralized tablet. The second approach was performed to determine if the organism can survive to a complete cycle of *relaxation – tablet implantation – incubation (biomineralization) – relaxation - tablet extraction* and if the organism can be further used by the pearl farm for pearl cultivation.

6.3 Semiconductor characterization.

In this section, the analytical techniques that were used to characterize all the semiconductors used in this work are presented.

The crystallographic composition of the semiconductors was evaluated by X-Ray Diffraction (XRD), using a Siemens D5000 diffractometer with Cu Kα1 radiation. The presence of functional groups and carbon or nitrogen doping was determined by attenuated total reflectance-Fourier transform infrared (ATR-FTIR) spectroscopy using a BRUKER ALPHA II FTIR spectrometer, by averaging 32 scans between 4000 and 400 cm^{-1} with a 4 cm^{-1} spectral resolution.

The Eg value was calculated from the Diffuse reflectance spectra (DRS), measured in the 200-800 nm range on an Agilent technologies Cary 5000 spectrometer equipped with an integration sphere for solids. Ba_2SO_4 was used as 100% reflectance reference. The data from the DRS spectrum was transformed using the Kubelka-Munk theory:

$$F(R) = (1-R)^2/2R \qquad \text{Equation 2}$$

Where the F(R) is the transformed reflectance and R is the reflectance [105], and the E_g value was obtained from the intercept of a straight line from linear region with the abscissa axis of a Tauc plot.

The microstructure was determined using a FEI Nova NanoSEM 450 Field Emission SEM (FEG-SEM), in immersion lens mode.

6.4 Determination of the pollutant model, particle shape and size and semiconductor presentation.

The photocatalysis of microplastics is a new field that was reported for the first time in 2019. Thus, to date there is limited information regarding the operational parameters of the reaction that may improve photocatalytic degradation.

To set the operational parameters for the determination of the photocatalytic activity of the biomineralized materials, preliminary tests were carried out. Two N-TiO_2 semiconductors with the same properties expected for the biomineralized materials were used: one derived from a typical sol-gel process (identified as sol-gel N-TiO_2) and the other derived from mussels' proteins (identified as bioinspired N-TiO_2). The tests were carried out using these semiconductors because the following three reasons:

(i) the relatively long times for biomineralization (compared with the available experimental time during a two-year postgraduate program);

(ii) the quantity of the obtained biomineralized materials was not enough to conduct both preliminary and photocatalytic tests, and

(ii) the physicochemical characteristics of both the sol-gel and bioinspired semiconductors were similar to those expected for the biomineralized materials.

6.4.1 Sol-gel and bioinspired synthesis for preliminary tests.

The sol-gel derived N-TiO_2 was obtained by the EISA (evaporation-induced self-assembling) method, which uses surfactants as pore forming agents and leads to the formation of a mesoporous material with relatively high surface area. The semiconductor was directly obtained in the form of a coating. It was prepared by mixing 2.0 mL of titanium tetrachloride ($TiCl_4$), 42.5 mL of anhydrous ethanol, 1.1375 g of Pluronic F127, 3.3 mL of distilled water, and 1.2 g of urea. The sol was stirred at room temperature for 5 min and the films were deposited on a clean glass substrate by dip coating using an immersion and emersion speed of 100 mm/min, and a dip duration of 60 s. The fresh films were exposed to water vapors for 30 s (by previously boiling distillated water) and then subjected to thermal treatment at 200 ºC during 2h to stabilize the mesoporous structure. After that, a thermal treatment at 500 °C for 3 h was performed to crystalize the anatase polymorph of TiO_2 [106]. The powders of this semiconductor were obtained using the same synthesis, procedure but drying the gel at 100 ºC for 24 h and then calcinating the obtained powders at 500 ºC for 3h.

The bioinspired N-TiO_2 was prepared by mixing 20 mL of the extrapallial fluid (EPF) of a mussel called *Mytilus edulis* (the EPF contains proteins that act

as pore forming agents and nitrogen-doping source) and 4 mL of titanium butoxide (TBT) for 2 h [107]. Hydrolysis was performed for 2 h at room temperature with constant stirring. Mineralization was then performed at room temperature for 4 h without stirring. Finally, the mixture was transferred to a Teflon-lined steel autoclave and subjected to a hydrothermal treatment at 150 °C for 12 h. The obtained crystalline powder was washed with distilled water and an aqueous dispersion of the powder (5g/50 mL) was prepared and used to prepare the coatings over the clean glass substrates by dip coating. The obtained coating was dried at 100 ºC for 1 h.

Both materials were characterized using the analytical techniques and procedures described in Section 6.3.

In this work, the model pollutant, the size and shape of the microplastics and the semiconductor presentation were considered important operational factors that may affect the photocatalytic degradation process. Thus, these factors were investigated during the preliminary tests, in order to set the most favorable test conditions for the determination of the photocatalytic properties of the biomineralized semiconductors.

6.4.2 Model pollutants for preliminary tests.

Two different types of microplastics (HDPE and LDPE), with different particle sizes and shapes were tested. The spherical HDPE microplastics were extracted from two commercially available facials scrubs, according to Napper et al. procedure [104]. Depending of the commercial brand, two sizes were obtained:

814.21 ± 90.61 µm (blue spheres) for Brand A and 381.87 ± 153.69 µm (orange and white spheres) for Brand B. The LDPE microplastics were obtained by cutting a commercial LDPE bag in squared films of 5x5 cm and 3x3 cm.

6.4.3 Preliminary photocatalytic tests.

The preliminary photocatalytic tests with the semiconductor's coatings were performed using a 100 mL glass container. First, a dispersion of 200 mg of the microplastics in 50 mL of the pH 3 buffer was prepared. The coated substrates were immersed in the dispersion and the glass container was placed inside a closed reactor chamber equipped with a stirring plate, a temperature thermostat and a 50 W Visible led lamp (Artilite, Slim LED, 400 – 800 nm). The experimental setup is presented in **Figure 12**.

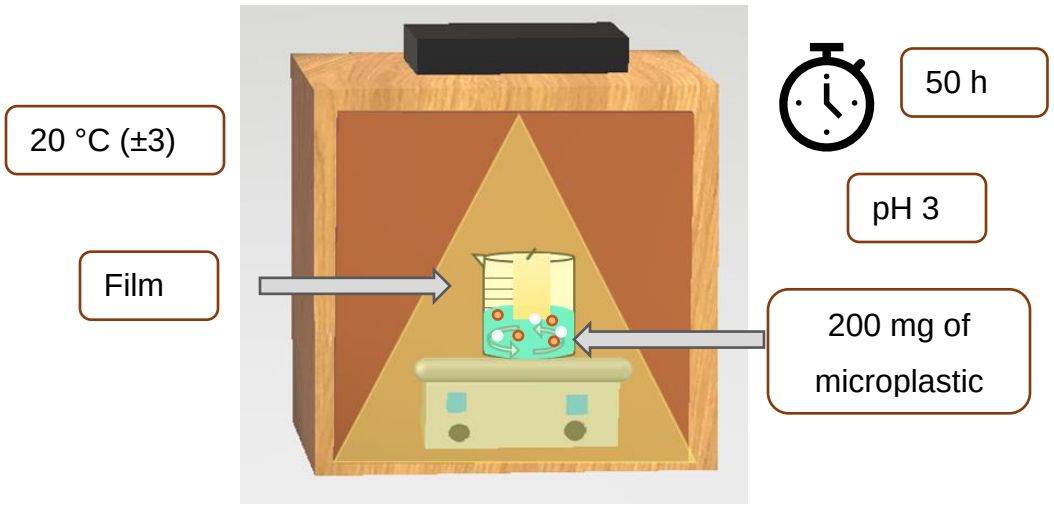

Figure 12. Experimental procedure for preliminary photocatalytic tests.

The tests were performed at 20 °C (± 3 °C), and pH 3 [108]. The pH was kept constant using a buffer made of acetic acid (CH_3 COOH) (0.1M) and sodium acetate ($C_2H_3NaO_2$) (0.1M). The irradiation source was kept at 22 cm from the samples. The system was irradiated for 50 h. Degradation was followed by changes in the mass of the microplastics. The mass was determined using a (ACZER, CY224C) analytical balance [108].

Mass loss was calculated using the following Equation:

$$\text{Mass loss (\%)} = [(M_0 - M)/M_0] \times 100 \qquad \text{Equation 3}$$

where M_0 is the initial mass of the MPs and M is the mass remaining after irradiation.

In the case of the preliminary tests using the semiconductors in the form of powders, the same procedure was followed by substituting the N-TiO_2-coated substrate with 200 mg of the powder materials. These tests were only performed for the film-shaped microplastics, as the research group has experimental evidence that the photocatalysis of spherical particles using a semiconductor in the form of powder is possible [108].

The different preliminary test conditions are summarized in **Table 2**. The preliminary tests of the “small” HDPE and LDPE microplastics for the bioinspired N-TiO_2 were not performed due to systematic errors and experimental time limitations.

Table 2. Description of the preliminary photocatalytic tests with a constant temperature of 20°C ± 3, and pH3.

Semiconductor	Type of microplastic	Size	Irradiation time
Mesoporous (coating)	HDPE	381.87 ± 153.69 µm	50 h
		814.21 ± 90.61 µm	
	LDPE	5 x 5 mm	
		3 x 3 mm	
Bioinspired (coating)	HDPE	814.21 ± 90.61 µm	50 h
	LDPE	5 x 5 mm	
Bioinspired (powder)	LDPE	5 x 5 cm	50 h
		3 x 3 mm	30 h

6.5 Photocatalysis of microplastics with the biomineralized materials.

From the results obtained in the preliminary tests, the operational conditions for the photocatalytic degradation of microplastics using the biomineralized semiconductors were set. The selected model pollutant was the HDPE in spherical form, and two sizes were tested (381.87 or 814.21 µm). The photocatalyst was used in the form of powders.

Two biomineralized semiconductors labelled as PS32N and PS90N were selected for the photocatalytic tests. The samples were incubated in *P. sterna* for 32 and 90 days, respectively and both were found to be coated with nacre (N)

when extracted from the oyster. The semiconductors were selected based in (i) the available quantities of powder after biomineralization and (ii) the light absorption properties of the biomineralized materials. The sol-gel derived amorphous precursor (not subjected to biomineralization) was also tested (labelled as “amorphous”).

The photocatalytic experiments were carried out in the same reaction system described in Section 6.4.3. The tests were performed by adding 45 mg of the semiconductor and 45 mg of the HDPE microplastics to 50 mL of distilled water (pH 7-8) in a glass container. The container was placed inside the chamber at 12 cm from the lamp. The temperature was set at 33 °C (± 3 °C). The reaction was performed under Visible light using a 50 W visible LED lamp (Fari, IP65) and continuous stirring. The photolysis experiments were carried out at the same conditions without semiconductors. The whole experimental setup is presented in **Figure 13**.

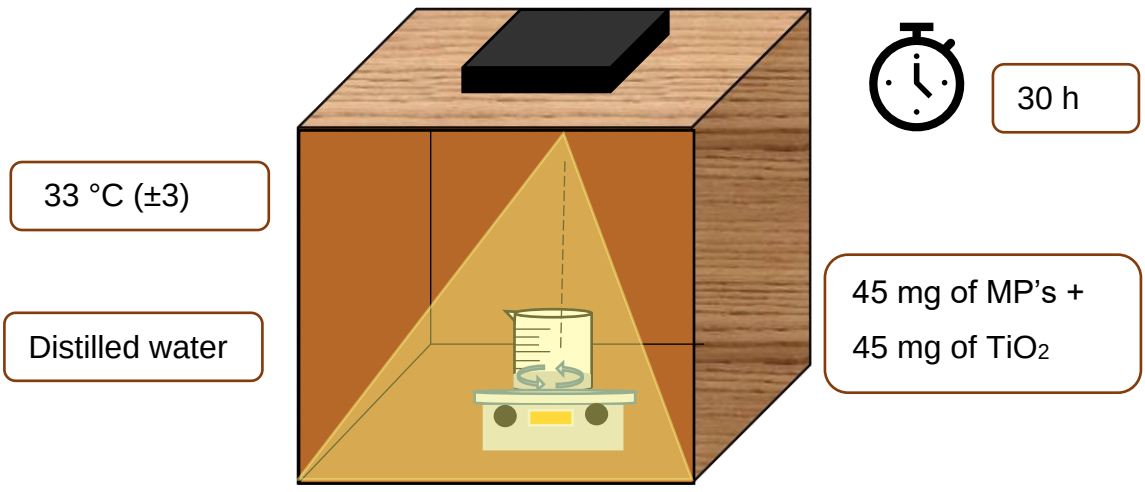

Figure 13. Experimental procedure for photocatalytic tests.

Degradation was followed by changes in the mass loss, the surface morphology and the infrared spectrum of the microplastics. The mass was determined using an analytical balance and the mass loss was calculated using Equation 5. The surface morphology of the microplastics was observed by optical microscopy using a Leica EZ4 stereomicroscope instrument. Infrared spectra were recorded in a Vertex 70 ATR-FTIR Bruker spectrometer by averaging 32 scans between 4000 and 400 cm^{-1}. Vinyl and unsaturated vinylidene indexes were calculated from the FTIR spectra of the microplastics after photocatalysis using equations 4 and 5 [109,110].

$$\text{Vinyl index (VI)} = A_{899}/A_{2920} \qquad \text{Equation 4}$$

$$\text{Unsaturated vinylidene index (UVI)} = A_{888}/A_{2920} \qquad \text{Equation 5}$$

The different microplastics, semiconductors and conditions used in the experiments are summarized in Table 3.

Table 3. Description of the photocatalytic tests using the biomineralized materials.

Microplastic	Semiconductor	Temperature	Irradiation time
HDPE (381.87 ± 153.69 µm)	Amorphous PS32N PS90N	33°C (+/- 3°C)	30 h
HDPE (814.21 ± 90.61 µm)	Amorphous PS32N PS90N	33°C (+/- 3°C)	30 h

6.6 Generated waste disposal.

The waste disposal was made according to the regulation of FCQ. Table 4 shows the wastes and the disposition containers for the project.

Table 4. Wastes and disposition containers.

Waste	Container
LDPE	G
HDPE	G
N-TiO_2	B
Photocatalysis Waste	C

CHAPTER 7

7. RESULTS AND DISCUSSION

7.1 Microplastics characterization.

7.1.1 Microplastics used in the preliminary tests.

The optical micrographs of the microbeads extracted from the two commercial scrubs are shown in **Figure 14**.The **Figure 14a** shows that the spherical blue microbeads extracted from Brand A have an average diameter of 814.21 ± 90.61 µm. **Figure 14b** present the spherical orange and white microbeads extracted from Brand B, which have an average diameter of 381.87 ± 153.69 µm.

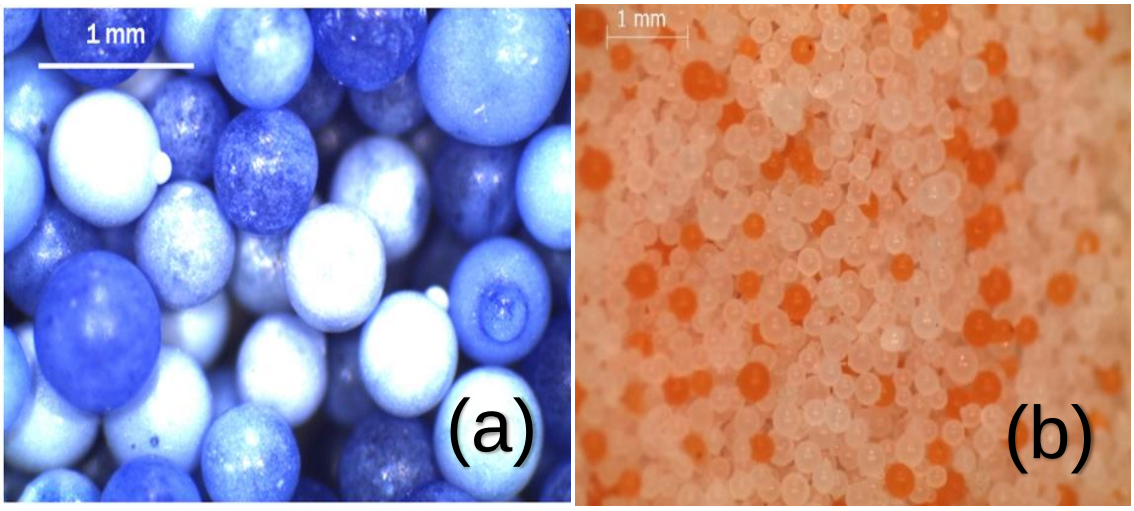

Figure 14. Optical micrograph of the microbeads obtained from the two commercial scrubs. (a) Brand A, (b) Brand B.

Since the label of the commercial scrubs do not specifies the composition of the microbeads, IR spectroscopy was used to confirm if they were made of plastic. **Figure 15** presents the obtained results. Both samples presented the same spectrum with absorption bands at 2912/2910, 2842/2849, 1465 and 716/731 cm^{-1} that correspond to the long alkyl chains of HDPE [111]. More specifically, the bands at 2912/2910 and 2842/2849 cm^{-1} were assigned to the C-H bond stretching vibration, while the bands 1465, and 716/731 cm^{-1} correspond to the CH_2 bending vibration.

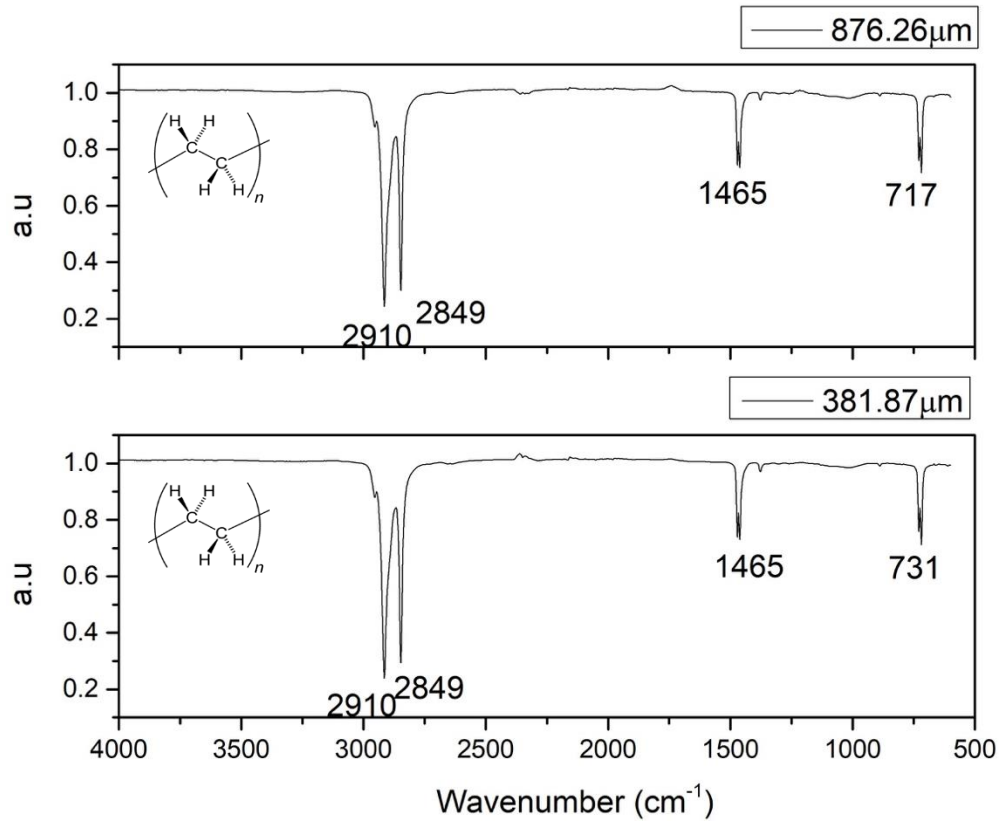

Figure 15. FTIR spectrum of microbeads extracted from the commercial facial scrubs.

As HDPE is a crystalline polymer, X-ray diffraction analysis was used to further confirm the polymer composition of the extracted microbeads. **Figure 16** shows the obtained XRD patterns. Both patterns presented the characteristics peaks at 20° and 25° [112] that correspond to the (110) and (200) crystalline planes of the orthorhombic crystal structure of HDPE.

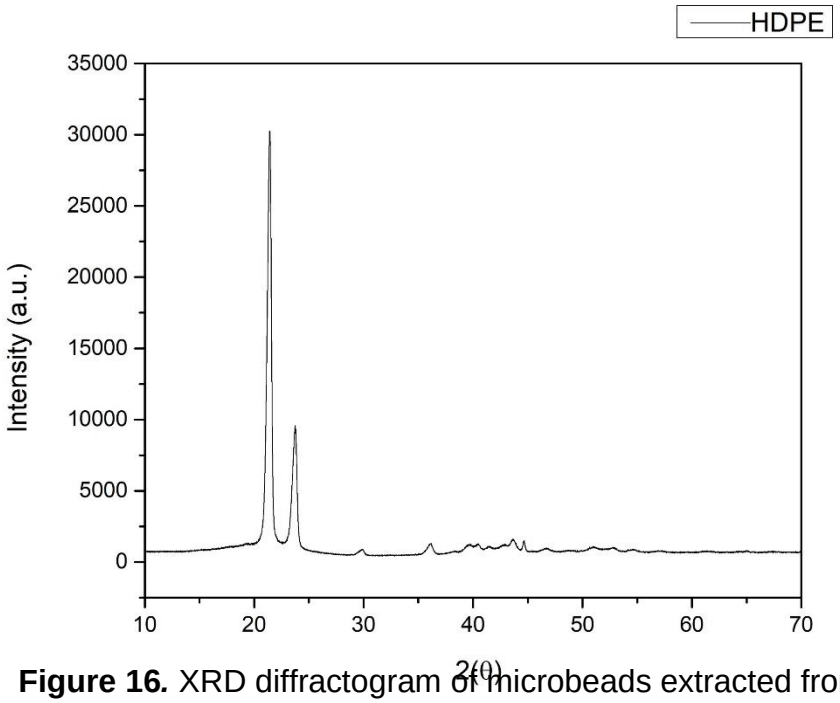

Figure 16. XRD diffractogram of microbeads extracted from the commercial facial scrubs (a) Brand A and (b) Brand B.

From the results of the microbeads characterization, it was found that the commercial scrubs of brands A and B contain HDPE microplastics, with a particle size of 814.21 ± 90.61 and 381.87 ± 153.69 µm, respectively.

n **Figure 17a** and **17b** are present the LDPE microplastics obtained from the plastic bag manually fragmented. The obtained sizes were 5x5 mm 17(a), and 3x3 mm 17(b).

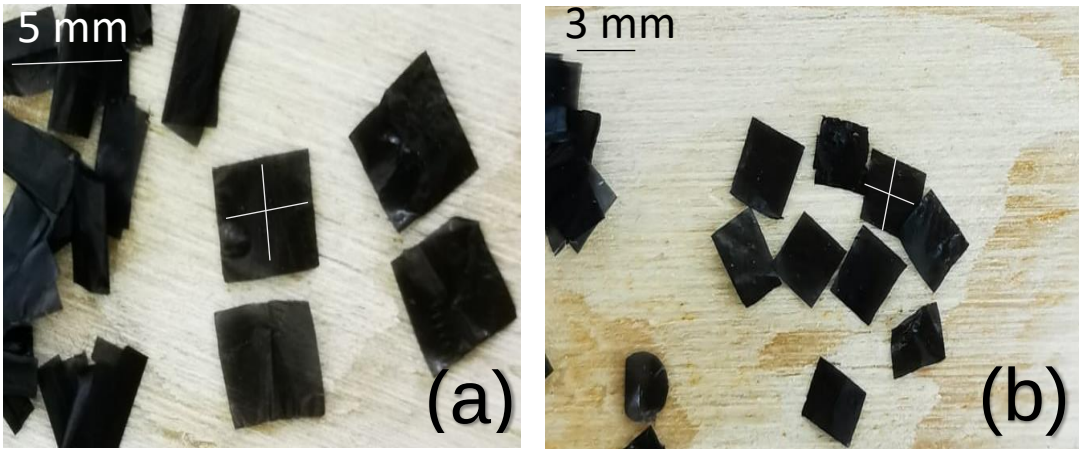

Figure 17. Microplastics in the form of films obtained from the commercial bag. (a) Films of size 5x5 mm, (b) Films of size 3x3 mm.

Although the label of the commercial bag specified that the product was formed by LDPE, the material was subjected to IR analysis to confirm the polymer composition. **Figure 18** shows that the FTIR spectrum of the plastic bag presents absorption bands at 2912, 2850, 1462, 718 cm^{-1}, which are characteristic of the long alkyl chains of LDPE [111]. The bands at 2912 and 2850 cm^{-1} were assigned to the C-H bond stretching vibration while the bands 1462, and 718 cm^{-1} correspond to the CH_2 bending vibration.

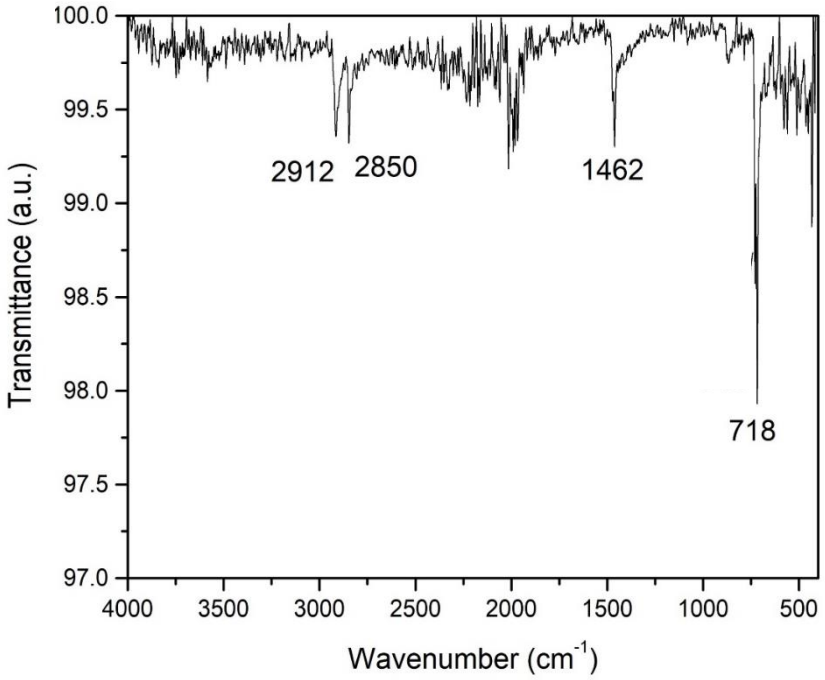

Figure 18. FTIR spectrum of microplastics extracted from the commercial plastic bag.

From the results of the plastics bag characterization, it was found that the commercial bag was effectively composed of LDPE, and that microplastics in the form of films can be obtained by mechanical fragmentation of this product.

7.1.2 Microplastics for testing the photocatalytic activity of the biomineralization-derived TiO_2 materials.

During the preliminary tests, it was found that the higher degradation (in terms of mass loss) was obtained for the spherical HDPE microplastics (see further details below, in Section 7.4.1). Thus, this plastic model was selected for testing the photocatalytic activity of the biomineralized TiO_2-based materials. Two

sizes were used, but due to availability limitations, Brand A was not found, and Brand C was used instead.

Figure 19 shows the optical micrograph of the microbeads extracted from the commercial facial scrub of Brand C. It was found that the purple microbeads present spherical shape with an average diameter of 876.26 ± 113.98 μm.

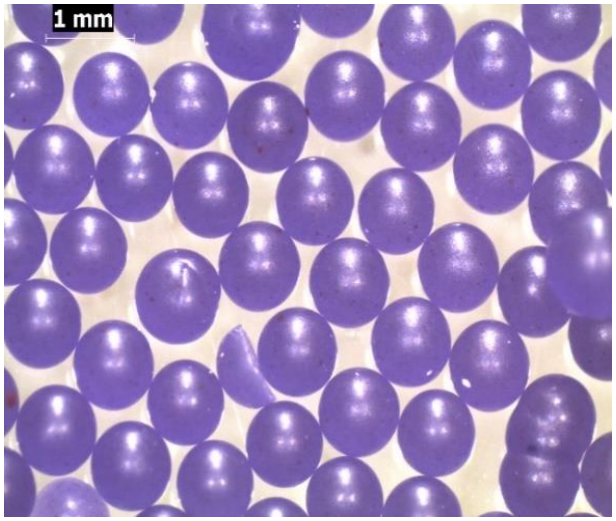

Figure 19. Optical micrograph of the microbeads from the commercials facial scrub of Brand C.

Figure 20 shows the FTIR spectrum of the microbeads extracted from the scrub C. The spectrum presents the absorption bands at 2910, 2849, 1465, 731 and 717 cm^{-1}, which are characteristic of the long alkyl chains that compose the high-density polyethylene (HDPE).

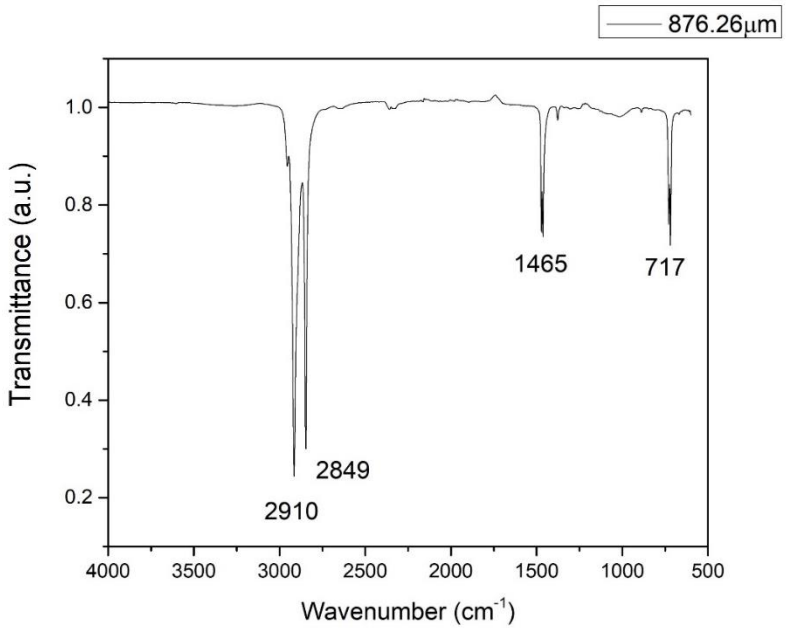

Figure 20. FTIR spectrum of microbeads extracted from the commercial facial scrubs.

7.2 Amorphous TiO_2 characterization.

Figure 21 presents the XRD pattern of the TiO_2 amorphous precursor. The diffractogram predominantly corresponds to the one characteristic of an amorphous material, i.e., a material where the atoms do not follow a periodic order. However, some “peaks” corresponding to a crystalline material can be observed in the region of 10 - 25º 2θ. The presence of those peaks can be explained by the crystalline organic intermediaries (between the reagents and TiO_2) that were formed during from the sol-gel synthesis of the TiO_2 precursor. However, this is only an assumption, as the peaks are greatly overlapped by the pattern of amorphous phase.

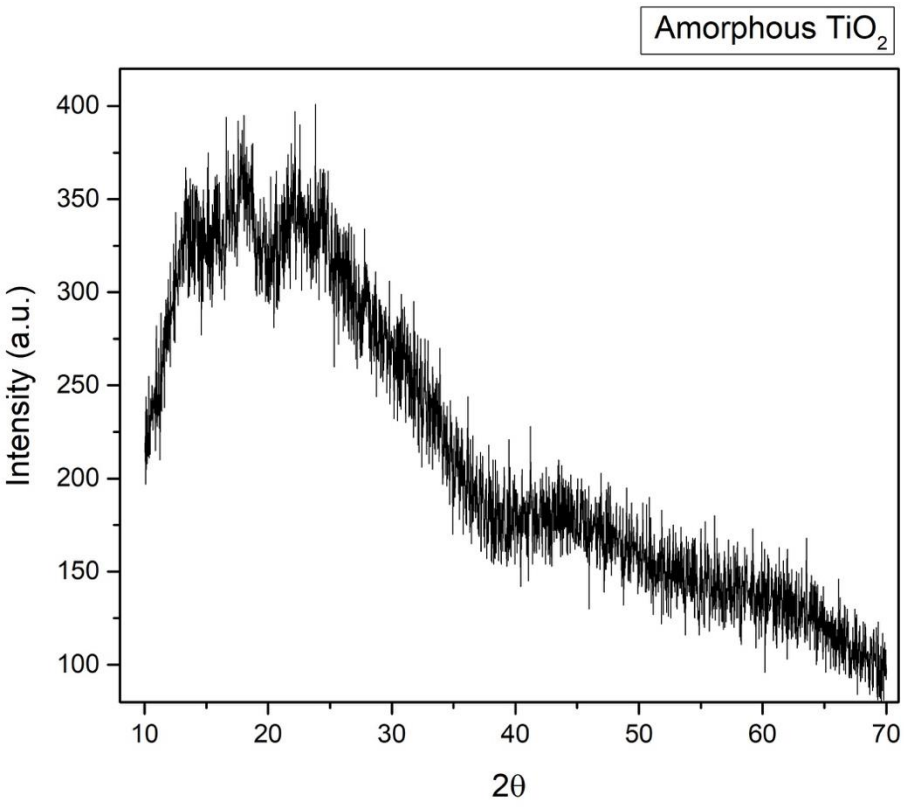

Figure 21. XRD diffractogram of the amorphous TiO_2 precursor.

Figure 22 shows the FTIR spectrum of the amorphous TiO_2 precursor. As this material is obtained the sol-gel process (without calcination), it was considered that the adsorption bands of the spectrum came from the synthesis residues (in sol-gel process, usually these bands disappear after thermal treatment). The band 3189 cm^{-1} was attributed to the -OH bond, probably from the ethanol used in the reaction. The peaks 1520 cm^{-1} and 1413 cm^{-1} were attributed to the stretching vibrations of the C=O bond, coordinated to Ti as bidentate ligands. Finally, the band 810 cm^{-1} is attributed to the Ti-O bond [25,90]

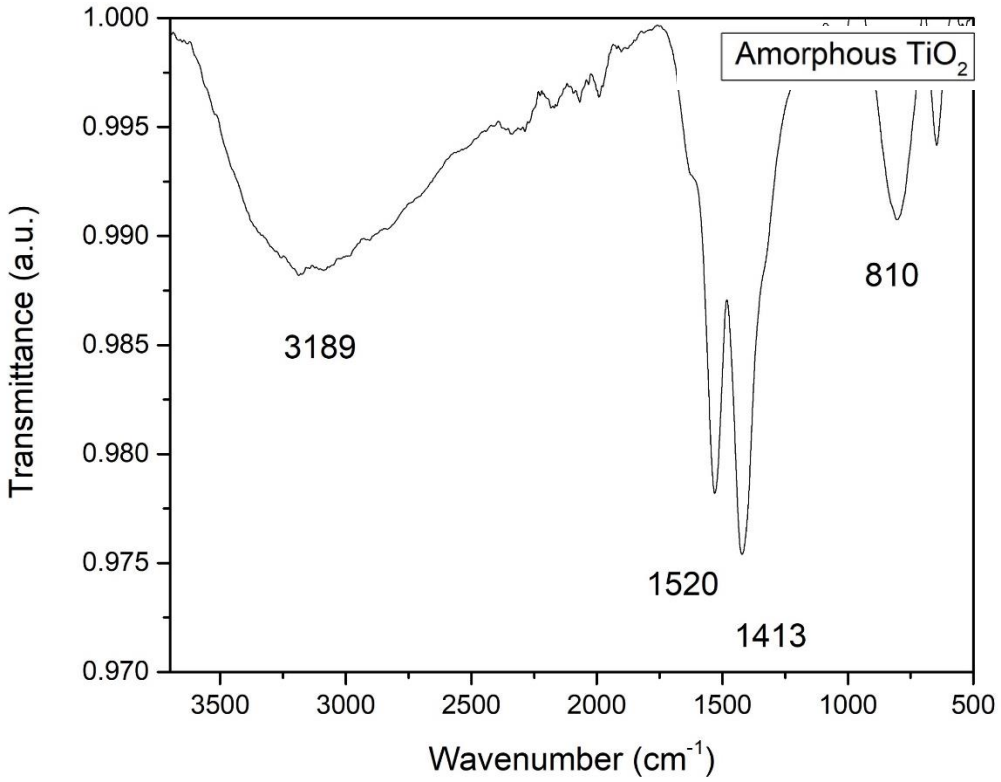

Figure 22. FTIR spectrum of amorphous TiO_2 precursor

Figure 23a presents the diffuse reflectance spectrum of the amorphous TiO_2 precursor and Kubelka-Munk transformation that was applied for Eg calculation. As observed in **Figure 23b**, the calculated Eg value was 3.0, which means that this sample absorbs light at 413 nm, in the visible range of the electromagnetic spectrum. It has been reported that the both the amorphous and crystalline TiO_2 are active only under UV light owing to its relatively large band-gap (3.2 – 3.3 eV). The lower Eg value obtained for the amorphous TiO_2 precursor prepared in this work was explained by the presence of the synthesis residues in the sample. As stated in section 6.2.1 at the end of the amorphous TiO_2 synthesis,

the powder is color yellow, which indicate that the materials absorb light in the visible region.

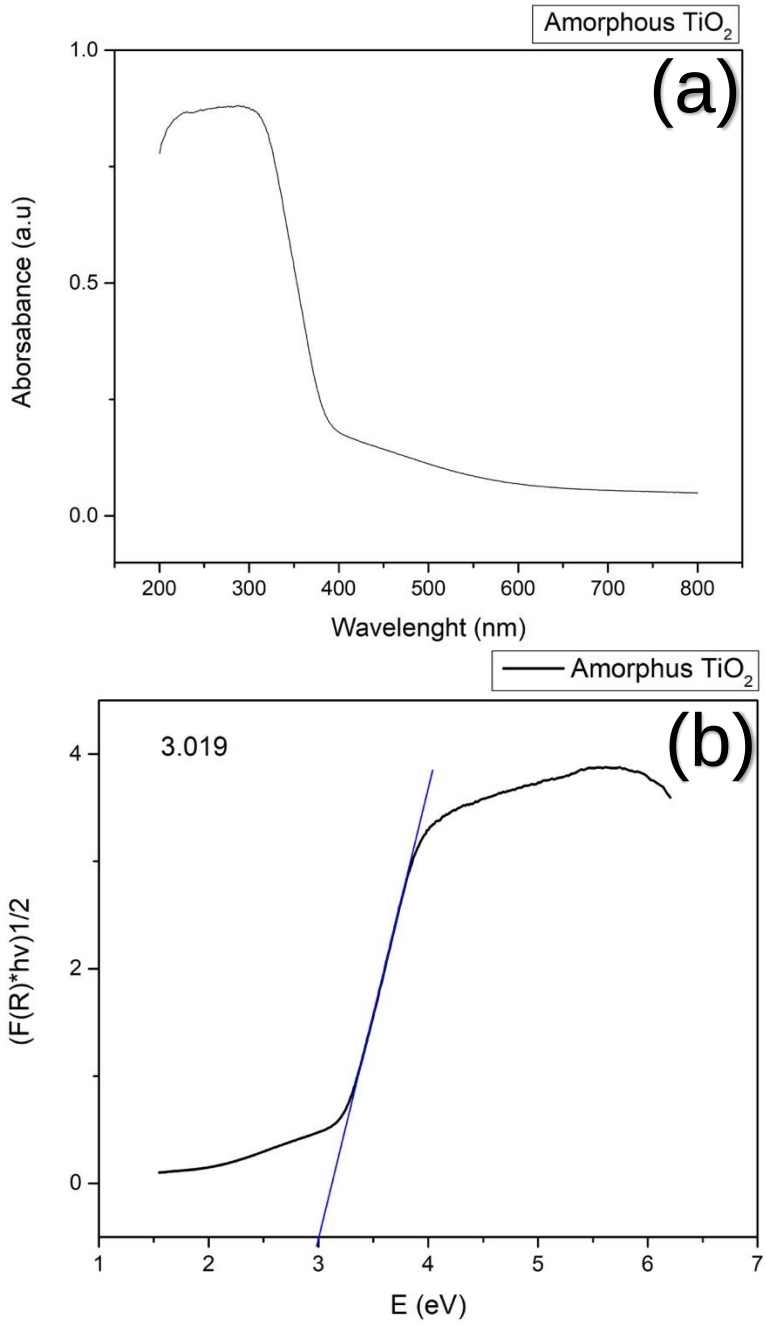

Figure 23. (a) Diffuse reflectance spectrum of the amorphous TiO_2 precursor and (b) Kubelka-Munk transformation for Eg calculation.

Figure 24 presents a SEM micrograph of the amorphous TiO_2 precursor, which is formed by irregular particles of variable sizes between 3 – 10 μm. The shape and particle sizes of the amorphous material obtained here are similar to those obtained for the TiO_2 amorphous precursor used in the work of Xie et al., (2016).

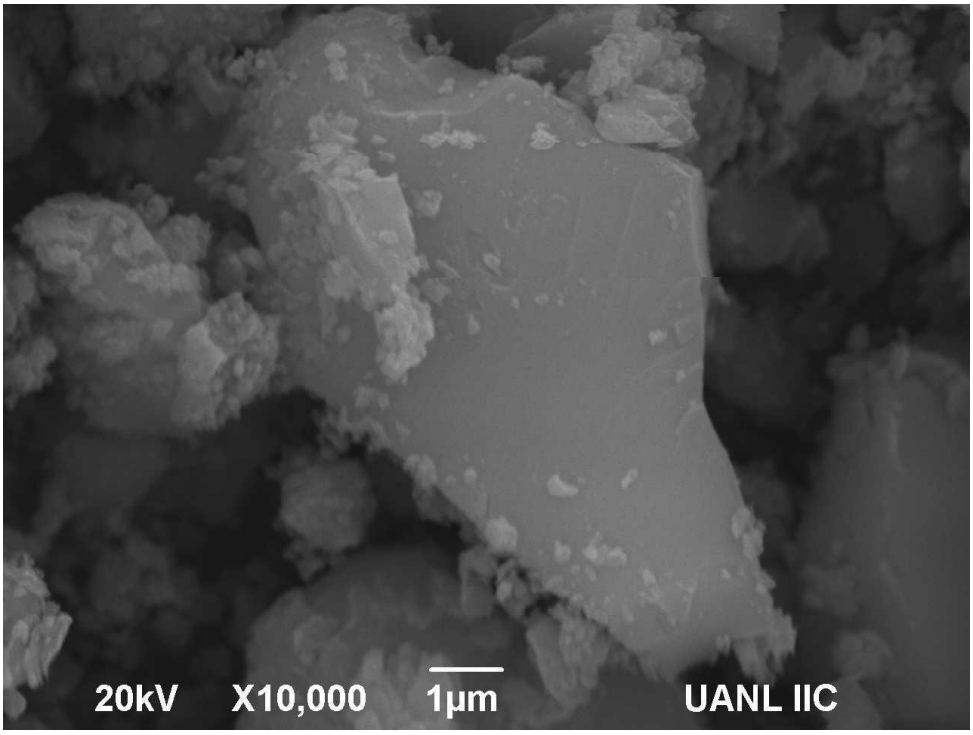

Figure 24. SEM micrograph of the amorphous TiO_2 precursor.

Figure 25 displays the nitrogen adsorption-desorption isotherm of the amorphous TiO_2 semiconductor. The Brunauer-Emmett-Teller (BET) model was used to calculate the BET surface area. The figure shows isotherm pseudo-type II, it is characteristic to no porous solids or microporous absorbent. This isotherm is associated to the metastability of the absorbed multilayer and delayed capillary condensation. This phenomenon is caused by the low aggregation structure.

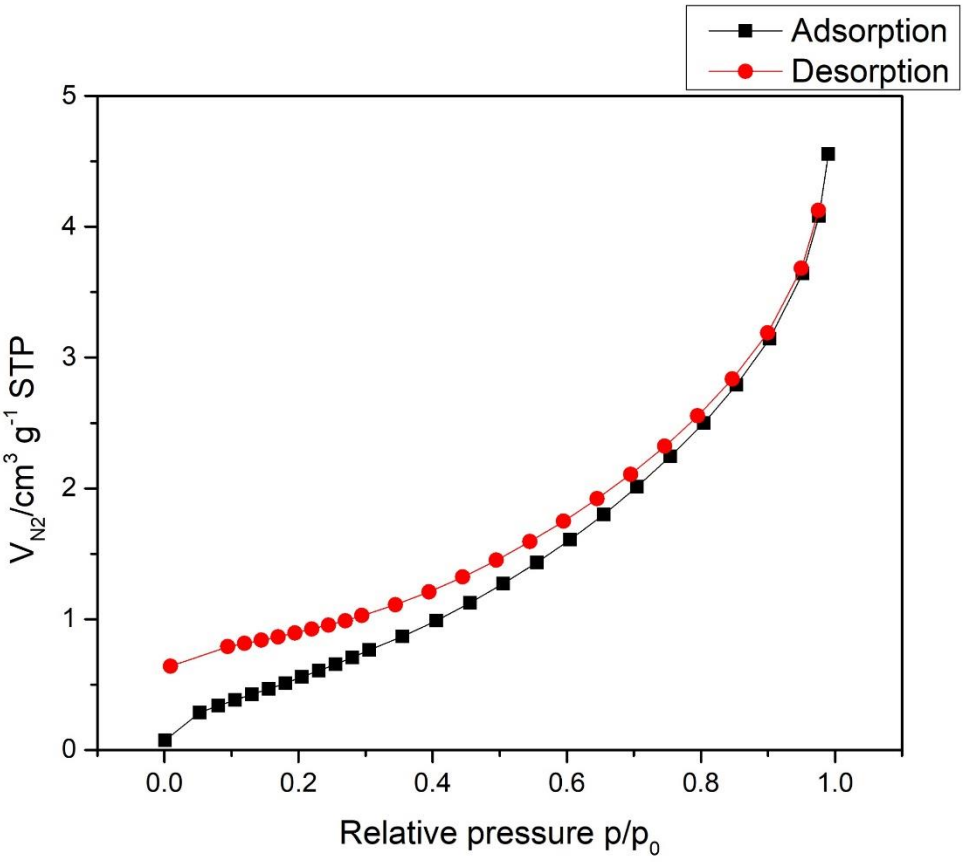

Figure 25. N_2 adsorption-desorption isotherm of amorphous precursor TiO_2.

The hysteresis has a shape of H3 loop is also linked with a non-rigid nature of the adsorbent and the location of the characteristic should be consistent with the destabilization of condensation at the limiting P/P_0 value.

From the BET model, it was found that the amorphous TiO_2 precursor has a surface area of 2.68 $m^2\ g^{-1}$. Compared with the commercial TiO_2 Degussa P25 of nano-spherical particles (51.4 $m^2\ g^{-1}$), the sample has a very low surface area and has a band-gap of 3.14 (eV), a surface area of, and a morphology [25,113].

From the characterization presented in this section, it was found than the precursor material is composed by a mixture of amorphous titanium dioxide with

some (maybe crystalline) synthesis residues that promotes the yellow color of the powders. Also, the powders are hydrated and present very low surface area. As stated before, this amorphous TiO_2 precursor was pressed in form of tablets that were implanted in the *P. sterna* oysters. The results related to the complete biomineralization process are presented in the next section

7.3 Biomineralization results.

The biomineralization of the amorphous TiO_2 precursor in *P. sterna* presented some difficulties such as organism mortality and tablet rejection. In the next two following sections, further details of these difficulties are presented.

7.3.1 Organisms survival ratio.

The organism survival ratio was calculated using the following equation (Eq. 6):

$$\text{Survival ratio (\%)} = (O_T\text{-}O_D)/O_T)*100 \qquad \text{Equation 6}$$

Where O_T is the number of organisms that were implanted, and O_D is the number of organisms that not survived

The first eight organisms obtained from Perlas del Cortez S. de R.L. M.I. were purchased in their facilities, but the relaxation and tablet implantation procedures were performed in the Centro de Investigaciones Biológicas del Noreste S.C. (CIBNOR). After the implantation, the organisms were returned to the oyster farm to perform the biomineralization process in their natural

environment. After two days, it was found that the survival ratio was 25%, as only two animals survive to the procedure. *P. sterna* oysters are commonly used for artificial pearl formation, where a plastic nucleus is implanted in the organisms by the same technique used in this work. Thus, it was considered that the implantation process cannot be related to the mortality of the organisms. The possible explanation considered to justify the low survival ratio is related to the significant stress induced to the oysters during by the round trip from Perlas del Cortez to CIBNOR.

A second tests was performed using eight new organisms. To reduce their stress during the implantation procedure, they were relaxed and implanted in the facilities of *Perlas del Cortez*. After implantation, the oysters were returned to their natural environment. This resulted in a survival ratio of 87.5%, as seven oysters survived during the whole procedure, including the incubation time. These results indicate that it is very likely that the cytotoxicity of the pressed nanoparticles of amorphous TiO_2 does not promote the death of the *P. sterna* oysters, and that the low survival ratio obtained for the first group of organisms was related with the stressful relocation procedure.

7.3.2 Tablet rejection ratio.

Due to TiO_2 precursor availability, two tablets were implanted in each organism. During the extraction process, it was found that some tablets were detached during the incubation process, as zero, half, one, or one and a half tablets were found inside the oyster at each incubation period. It was

hypothesized that the precursor material irritates the organism causing the expulsion of the tablets. This latter phenomenon may be promoted by the porosity of the tablets (due to particle aggregation during pressing), which lead to poor attachment to the oyster's shell.

The total rejection ratio (considering the whole biomineralization process for 90 days) was calculated by the following equation:

$$\text{Total rejection ratio (\%)} = 100 - [(I_T - R_t)/I_T)*100] \qquad \text{Equation 7}$$

where I_T is the number of implanted tablets and R_T is the number of recovered tablets. Using equation 7, it was found that the total rejection ratio of the TiO_2 tablets using *P. sterna* oysters is 40%, as from a total of 20 tablets, only eight were extracted after biomineralization.

To reduce this rate[1], we suggest to paste the precursor in a flat plastic disks polished from both sides. Then, perform the implantation of the tablet by attaching the plastic side of the tablet to the shell, between the mantle and periostracum layer.

7.3.3 Biomineralized TiO_2 materials.

7.3.3.1 XRD analysis.

[1] The suggested procedure was not performed in this work due to oyster limited availability in the farm.

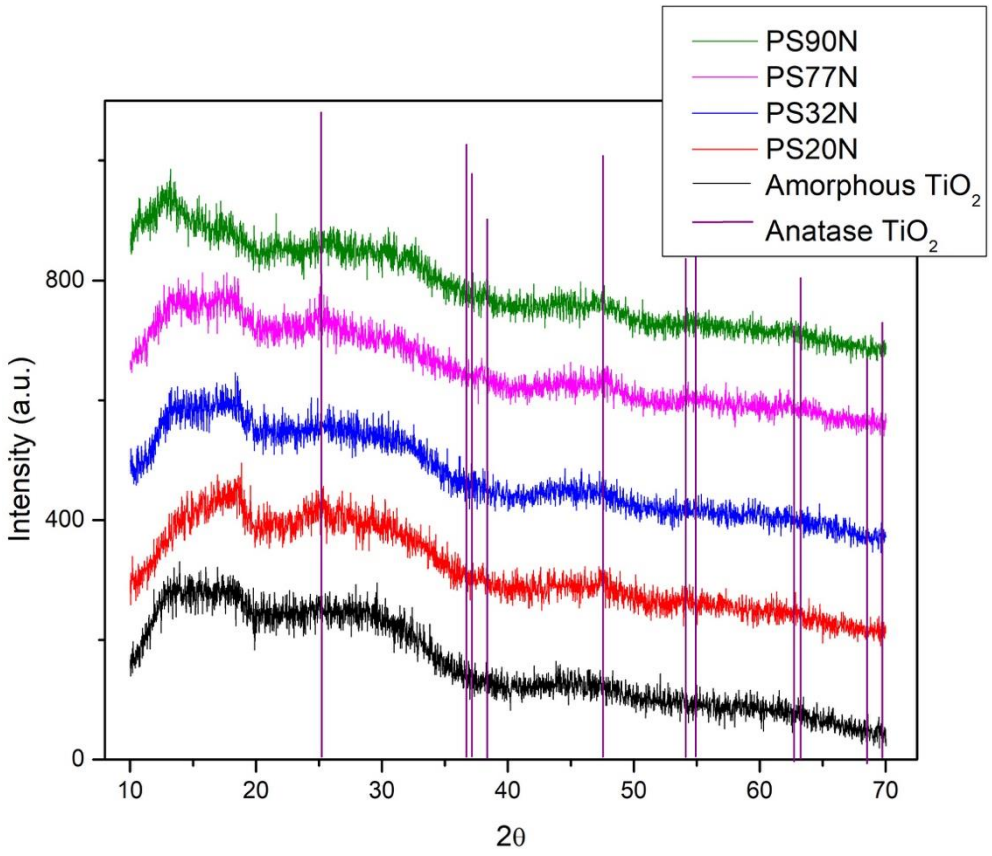

Figure 26. XRD patterns of the TiO_2 materials biomineralized inside the *P.sterna* oysters for PS20N, PS32N, PS77N and PS90N days. For comparison, the spectrum of the TiO_2 amorphous precursor was included. Also, the characteristic peaks of the anatase phase are shown (ICDD file 21-1272).

After the incubation periods, the TiO_2 biomineralized tablets were extracted and the nacreous layer was removed before characterization. **Figure 26** shows the XRD spectrum for each biomineralized material. In that figure, the spectrum of the amorphous TiO_2 precursor was also included. A first comparison of the spectra shows that there are only slight changes in the crystalline structure of the

biomineralized materials. All the biomineralized TiO_2 tablets remain predominantly amorphous, although some diffraction peaks at 25º, 38º, 47º and 54º 2θ that can be attributed to the (101), (004), (200) and (211) crystalline planes of anatase TiO_2 are visible in the patterns of the samples incubated for 20, 77 and 90 days (PS20N, PS77N and PS90N, respectively). The presence of this polymorph of titanium dioxide is a good characteristic of the biomineralized materials, as it is well known that anatase has high photocatalytic activity [83,114].

The incomplete crystallization of anatase TiO_2 was an unexpected result, as according to Xie et al. (2015) [25], complete crystallization of an initially amorphous TiO_2 material was accomplished after incubation for 60 days inside *Cristaria plicata* mussels.

The incomplete crystallization of TiO_2 in this work can be related to the differences between (i) the organic matrix and (ii) the nacreous layer of *P. sterna* oysters and the same components of *C. plicata* mussels.

As exposed in Chapter 2, the organic matrix of mollusks, which is basically a mixture of proteins, glycoproteins, chitin and lipids, oversees the growth and the regulation of the crystal formation among the nacreous layer. This matrix controls the shape, the deposition, and the crystalline form (e.g. calcite, aragonite, vaterite) of the biominerals that are synthetized by the mollusks. On the other hand, the nacreous layer arranges the nanostructures of crystallization in a different pattern. It is known that the composition of the organic matrix and the nacreous layer varies between different species of mollusks, leading to biomaterials with different properties.

For example, in the work of Xie et al. [25], *C. plicata* mussels accomplished the complete crystallization of an amorphous TiO_2 material. *C. plicata* is a freshwater mussel and this is an essential difference with the seawater oysters used in this work. In their natural environment, each one of these species are subjected to a wide gamma of components and molecules that enrich the difference in their organic matrix [90]. Additionally, the differences in the arrangement of the nanostructures addressed by the nacreous layer can be seen in the different appearance of the final product in the case of pearl formation: *C. plicata* produces withe pearls while and *P.sterna* produces pearls in various colors [90].

The wide peaks in the 2θ interval of 10º – 20º of the XRD spectra of all the biomineralized materials could not be identified. However, they may correspond to the Ti-acetate complexes or other synthesis residues that were formed during the sol-gel preparation of the amorphous precursor, and, as shown in **Figure 26**, were not removed or transformed during the biomineralization process.

7.3.3.2 FTIR analysis.

Figure 27 shows the FTIR spectra of the TiO_2 biomineralized inside *P.sterna* at different time laps. The amorphous TiO_2 was also included for comparison

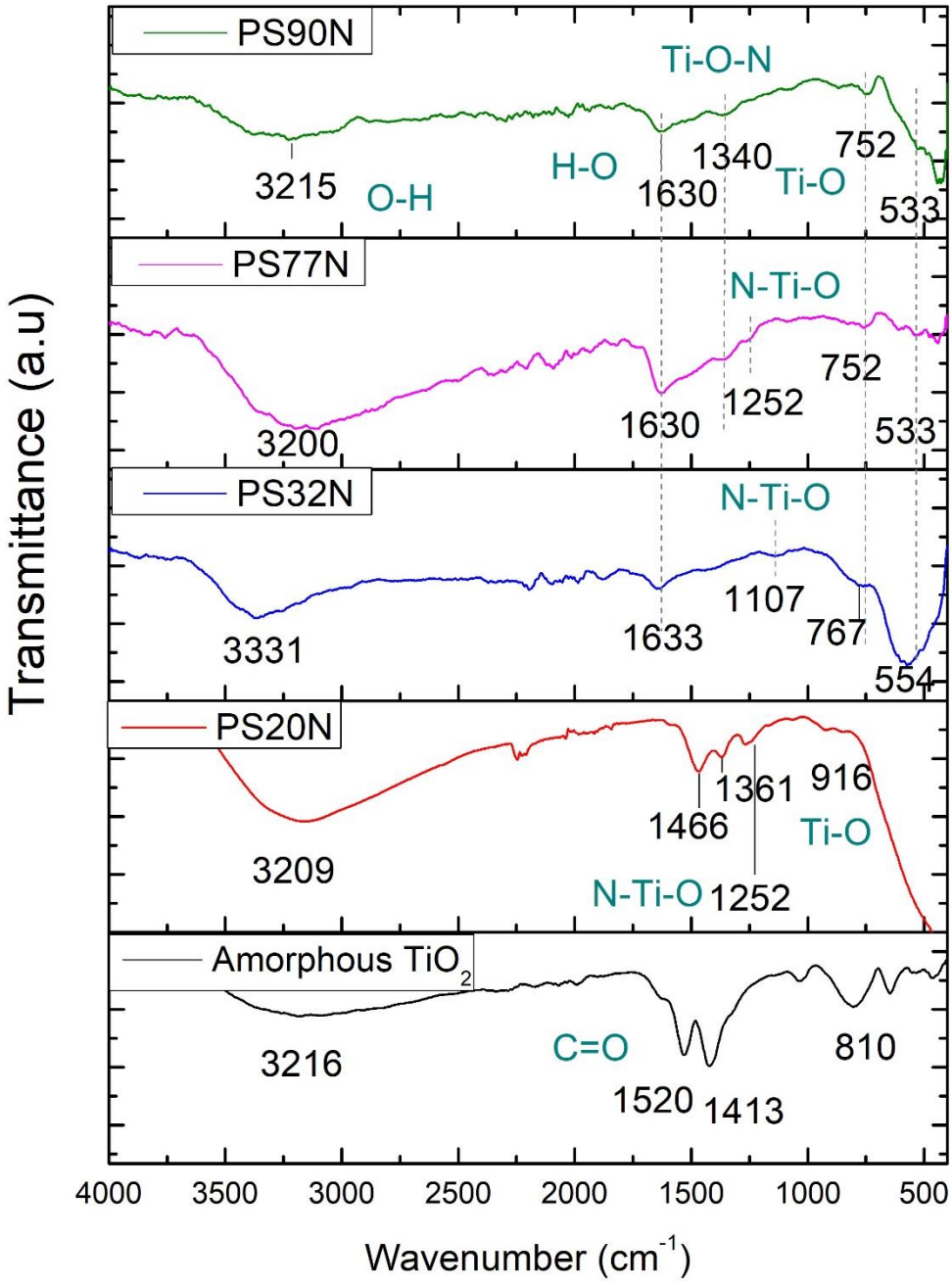

Figure 27. FTIR spectra of the TiO_2 biomineralized inside *P. sterna* oyster for 20, 32, 77 and 90 days.

Figure 27 shows the FTIR spectra of the TiO_2 biomineralized inside *P.sterna* at different time laps. The amorphous TiO_2 was also included for comparison.

The red spectrum of the TiO_2 material incubated for 20 days, labelled as PS20N, shows the same four principal adsorption bands that were present in the amorphous TiO_2 precursor (black spectrum). The two adsorption bands at 1466 and 1361 cm^{-1} can be attributed to the symmetric stretching of the C=O bond of the Ti-acetate complexes. The intensity of these bands is lower respect to the amorphous TiO_2 precursor (black spectrum), indicated that the Ti-acetate complexes disappear with biomineralization. The band at 916 cm^{-1} correspond to the Ti-O stretching and Ti-O-Ti bridging stretching bonds while the broad band at 3209 cm^{-1} correspond to the OH groups that are attached to the sample. As shown by the red spectrum, the TiO_2 biomineralized for 20 days is more hydrated than the amorphous precursor is beneficial in the photocatalytic process during the hydroxyl radical formation.

The samples biomineralized for PS32N, PS77N and PS90N days present similarities, and four main adsorption bands can be found in the range of 3311-3200, 1633-1630, 767-752 and 553-533 cm^{-1}. The broad band 3311-3200 cm^{-1} is assigned to the stretching vibration -OH a hydroxyl groups bond and the adsorbed H_2O. The 1633-1630 cm^{-1} band is attributed to the bending vibration H-O bond. The 767-752 cm^{-1} band is the stretching vibration of the Ti-O stretching, and the 553-533 cm^{-1} band is the Ti-O-Ti bridging streching bond [115–117]. The additional weak bands at 1107 cm^{-1} (PS32N), 1252 cm^{-1} (PS20N and PS77N) and 1340 cm^{-1} (PS77N and PS90N) were are attributed to the vibrations of the N-Ti-

O and Ti-O-N bonds [117–119] , suggesting that the N species were incorporated into the TiO_2 lattice. However, these results may be confirmed by other characterization techniques such as XPS or elemental analysis.

From the infrared analysis, it was observed that the TiO_2 changes during biomineralization. These changes were attributed to the interaction of TiO2 with the organic matrix and the nacreous layer. As biomineralization time increases, **Figure 27** shows that there is a gradual despairing of the C=O bond and an increase of the hydration of the sample (except for sample BS90N). This latter characteristic is beneficial in the photocatalytic process during the hydroxyl radical formation, as –OH group reacts with the photoexcited holes (h+) to form hydroxyl radical (·OH). These are powerful oxidant agents that degrade organic pollutants into less complicated and harmful molecules, or CO_2 and H_2O. Furthermore, the incorporation of nitrogen species in the TiO_2 lattice will lead to adsorption of light in the visible region of the electromagnetic spectrum.

7.3.3.3 UV-Vis analysis.

Figure 28 shows the UV-visible spectra of biomineralized and amorphous TiO_2. Almost every sample absorb radiation in the visible range of the electromagnetic spectrum, including the amorphous TiO_2 precursor. The absorption profiles of all samples are similar. The semiconductor biomineralized for 77 days shows absorption in a higher interval of the spectrum (pink curve in Fig.28) that other samples.

In the figure, it can be seen an increase in the ranges of absorption, the only sample that doesn't follow this in the amorphous TiO_2 precursor (black line) because it already archives the visible spectrum which is an unexpected result.

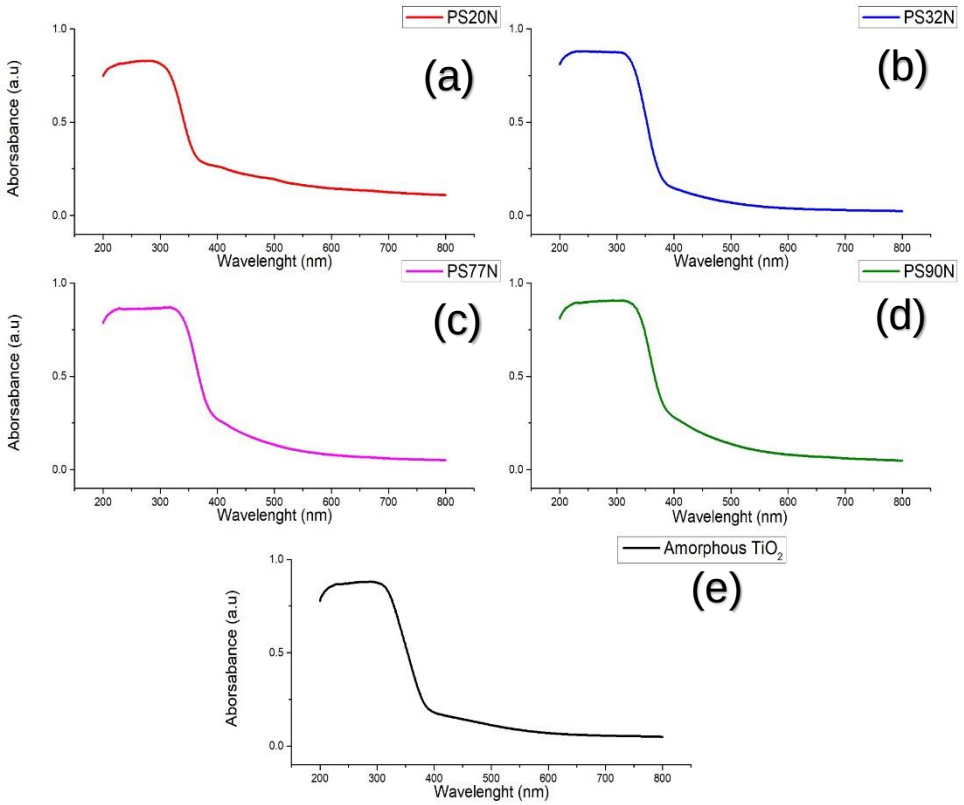

Figure 28. UV-Vis absorption spectra of biomineralized (a-d) and amorphous TiO_2 (e) semiconductors.

For the band-gap calculation, it was used the Kubelka Munk function. The Eg values were obtained from the intersection of a straight line from the linear region with the abscissa axis of a plot $(F(R)*hv)^{1/2}$ vs hv as shown in **Figure 29**. The Eg values obtained for each sample with their corresponding wavelength of absorption are present in Table 5.

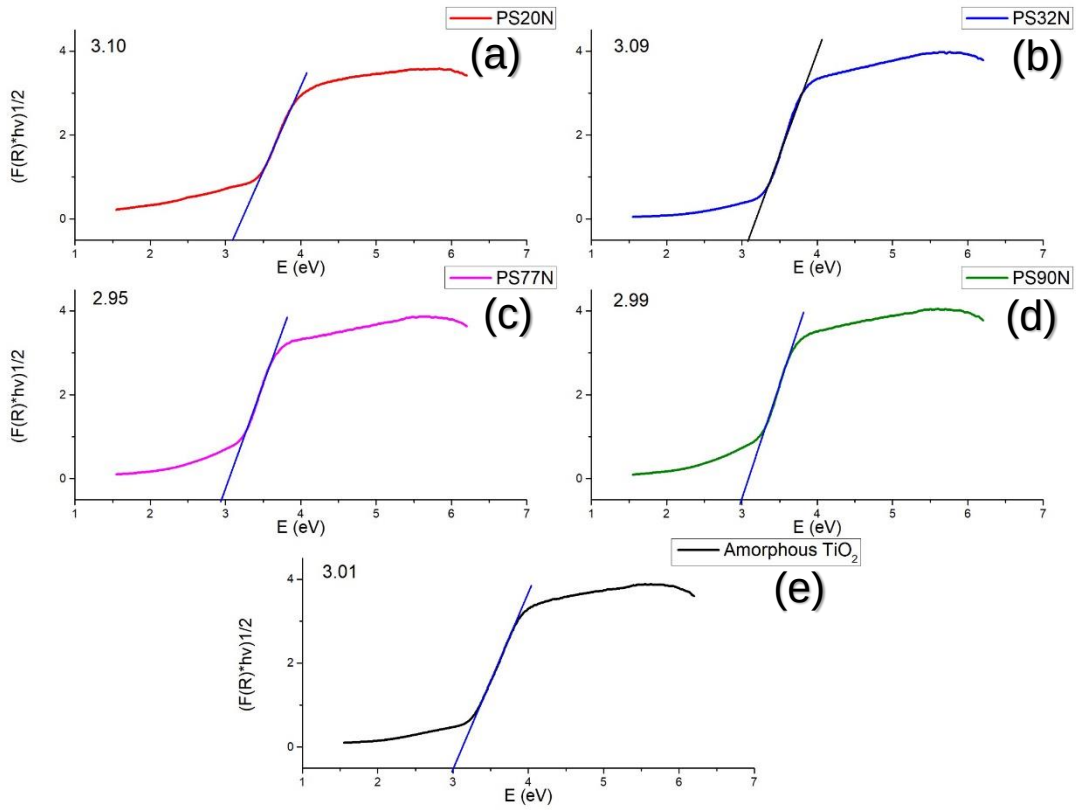

Figure 29. Plots $(F(R)*hv)^{1/2}$ vs hv of biomineralized (a-d) and amorphous TiO_2 (e) semiconductors.

The biomineralized TiO_2 sample that shows a higher absorption in visible light is PS77N (420 nm), then the PS90N (414 nm), after the amorphous (410 nm), the PS32N (401 nm), and the one with the lowest value is the sample 20N (399 nm). These values mean that, although almost all samples absorb visible radiation (as confirmed in Fig. 29), the samples biomineralized have a progressive increment in the absorption of a higher wavelength. These results suggest that the biomineralization, improve the optical properties of the semiconductor precursor. These results are in good agreement with those obtained by FTIR, as

the vibration bands from the FTIR spectrum are gradually more visible in the samples biomineralized, in sample SP90N is the band at 1340 cm^{-1} attributed to the bond Ti-O-N. Sample PS77N and PS32N present a band at 1252 and 1107 cm^{-1} respectably, attributed to the bond N-Ti-O.

Table 5. E.g. calculation using Kubelka Munk function.

Sample	**E.g. (eV)**	**The wavelength of photon absorption (nm)**
Amorphous	3.01	410.97
20N	3.12	399.97
32N	3.09	401.52
77N	2.95	420.58
90N	2.99	414.12

From the previous semiconductor characterization, it was found that complete crystallization of the amorphous materials does not occur during incubation inside *P. sterna* for up to 90 days. However, partial crystallization of TiO_2 was achieved. Additionally, the most of the biomineralized semiconductors presented high levels of hydration and were doped with nitrogen, making them active in visible light.

7.4 Preliminary tests for the selection of the operational conditions of the photocatalytic tests for the biomineralized materials.

In this section, the results from the preliminary photocatalytic tests are presented. As stated in the previous Chapter the preliminary tests were performed with two N-TiO_2 semiconductors (with similar characteristics to those expected for the biomineralized ones) to set the most favorable test conditions for the determination of the photocatalytic properties of the biomineralized semiconductors.

7.4.1 Semiconductor characterization.

Figure 30 shows the X-ray diffraction of the bioinspired TiO_2 to evaluate the crystallization process of the sample. The powder contains the TiO_2 anatase phase (JCPDS file No. 02-021-1272), that has higher photocatalytic performance than rutile and brookite TiO_2. The pattern indicates that the proteins contained in the EPF used as a doping source do not interfere with the crystallization of the sample. The proteins took from *Mytilus edulis* promotes the crystallization of anatase TiO_2. Two small peaks at 36 and 44° are shown in the pattern, which are characteristic of the rutile crystalline phase TiO_2 (JCPDS file No. 01-076-0317). It is well known that this polymorphs mixed-phase has a synergetic effect, when rutile and anatase are combined it promote the increase of the photocatalytic activity due to interfacial charge separation between the two phases, which inhibit the detrimental electron-hole recombination process.

However, the results reported by Zeng et al. (2015) [25] are in disagreement with the obtained in our study. In that work, it was used as EPF source a freshwater mussel (*Cristaria plicata*). There, the brookite TiO_2 phase was present in the semiconductors synthesized with a low concentration of proteins, suggesting that the EPF protein controls the crystalline phase and significantly prevents the formation of brookite [107]. Here, the EPF was extracted from marine *Mytilus edulis* mussels, which habit in marine environments with saltwater. Then, the difference obtained here was attributed to the differences in the EPF physical properties of both mussels' families.

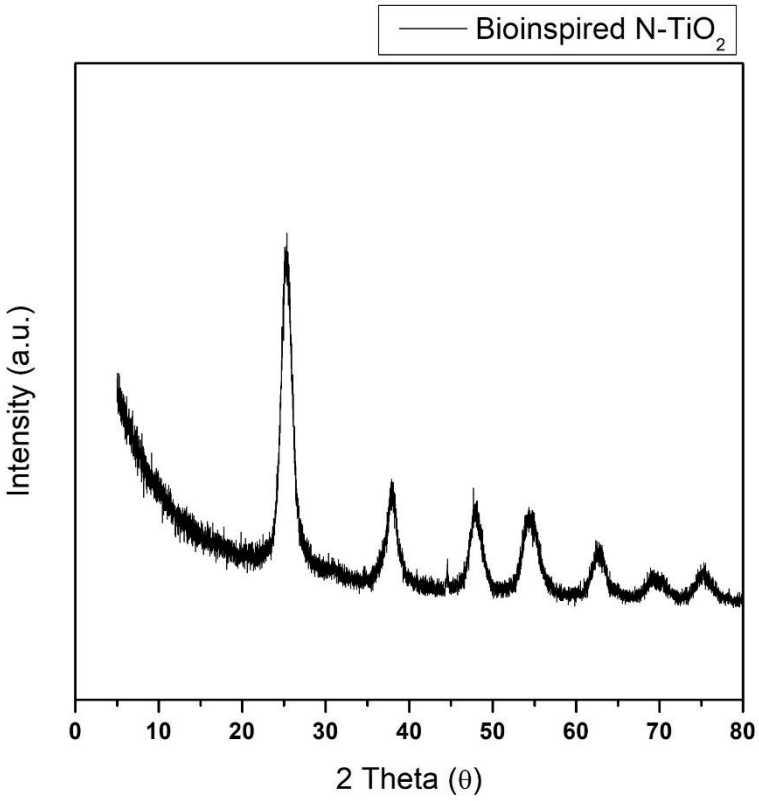

Figure 30. XRD of the bioinspired N-TiO_2.

Figure 31 presents the XRD pattern of the sol-gel derived sample N-TiO_2 coating. It can be observed that the coating is only composed by the anatase polymorph of TiO_2, (ICDD file 21-1272), known for its high photocatalytic activity [120]. The X-ray structural analysis of the samples did not show any detectable dopant-related peak [118].

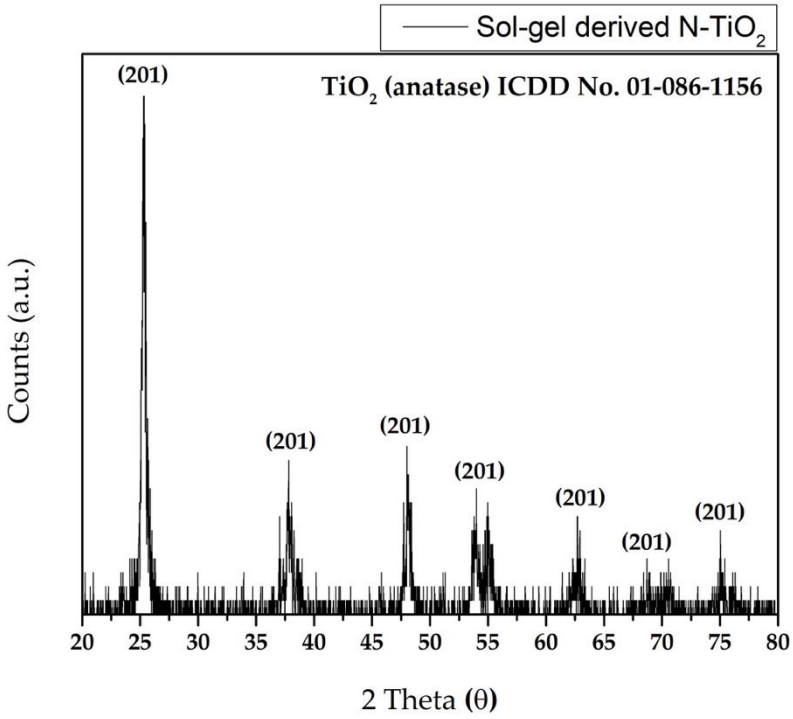

Figure 31. XRD of the sol-gel derived N-TiO_2.

The FTIR of the bioinspired synthesis route is shown in **Figure 32**. In the spectrum there are five characteristics peaks, most of them were already mentioned in Fig. 32. The two distinct peaks that portray the presence of nitrogen are the bands around 1415 cm^{-1}, and 1080 cm^{-1} correspond to the vibrations of the Ti–N bond. The bands of the O-H group are present at 3230 cm^{-1}, and 1630

cm^{-1}. The Ti-O and Ti-O-Ti stretching vibration of TiO_2 is attributed to the band 755 cm^{-1} [25,116,119].

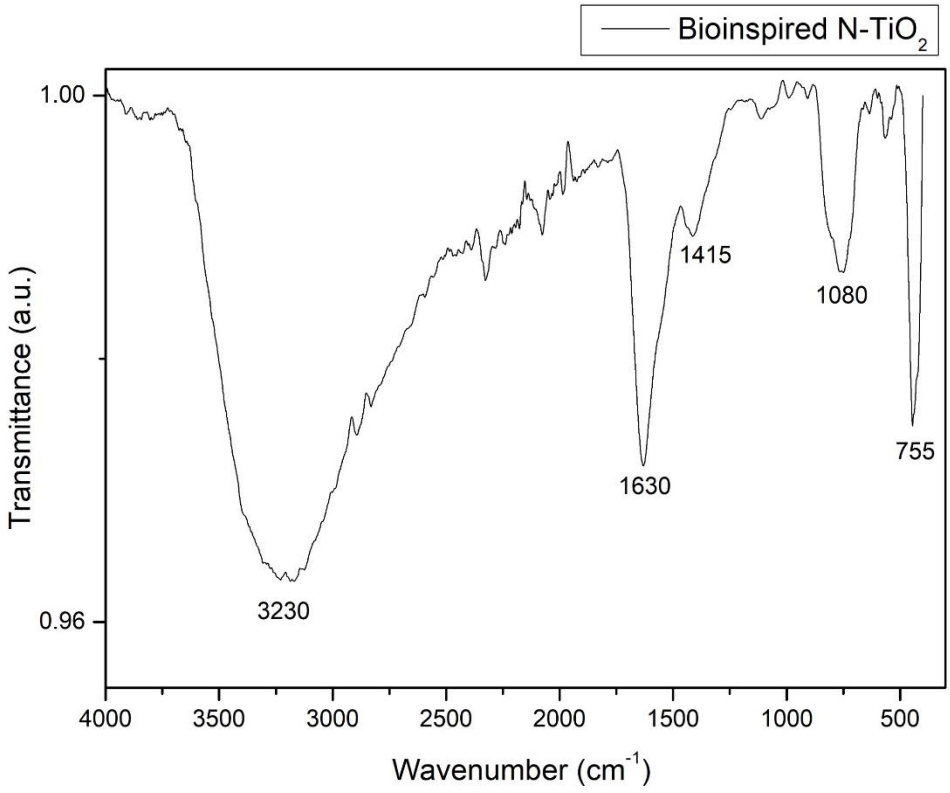

Figure 32. ATR-FTIR spectrum of the bioinspired N-TiO_2.

Figure 33 shows the FTIR spectrum of the sol gel derived sample. The bands at 3157 cm^{-1} and 1630 cm^{-1} were attributed to the stretching and bending vibration of the water and O-H groups. The band around 1450, 1340, 1252 and 1104 cm^{-1} correspond to the vibrations of the N-Ti-O and Ti-O-N bonds confirming the nitrogen doping. In the range of 1000-600 cm^{-1} were found the bands attributed to the Ti-O and Ti-O-Ti stretching vibrations of TiO_2, and the band at 2864 cm^{-1} may be attributed to the C-H stretching mode from organic residuals

associated to the incomplete thermal degradation of Pluronic F127 during calcination [107,115–117,121].

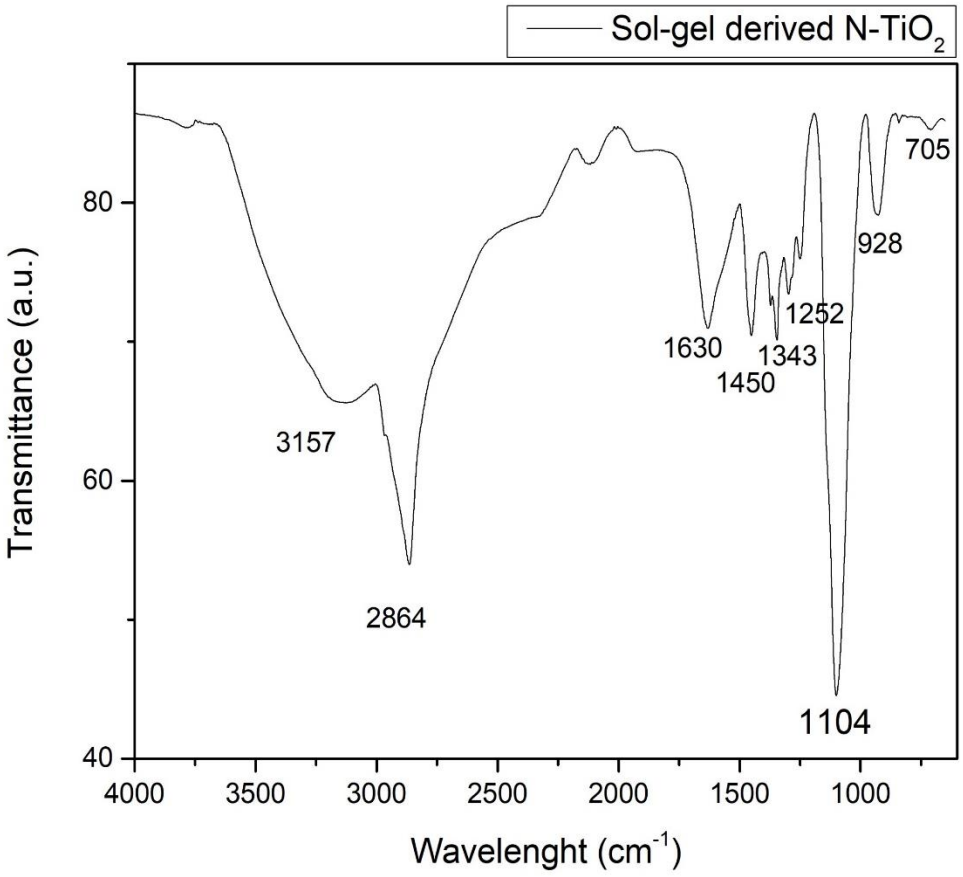

Figure 33. ATR-FTIR spectrum of the sol gel derived N-TiO_2.

Table 6 shows the Eg value of the semiconductors prepared with different synthesis rout, the Kubelka Munk function was used to calculate the band-gap of both samples. The bioinspired N-TiO_2 have an Eg value of 2.90 eV, and the sol gel derived TiO_2 has an Eg = 3.10 eV. These values mean that both samples absorb visible radiation. These results are in good agreement with those obtained by FTIR.

Table 6 . Eg calculation using Kubelka Munk function.

Sample	Eg (eV)	Wavelength of photon absorption (nm)
Bioinspired N-TiO_2	2.90	428
Sol gel derived N-TiO_2	3.10	400

Figure 34 shows the FEG-SEM micrographs of both N-TiO_2. The micrographs of the bioinspired route N-TiO_2 is shown in **Figure 34(a)** this semiconductor has agglomeration with different diameters and less homogeneous porosity, the large particles are formed by small particles approximately of 10 nm. This morphology promotes a high surface area, which is 219.42 ± 1.82 m^2/g. However, grains contain several dislocations and defects, that interrupts the periodicity of the crystalline nature. The sol gel derived N-TiO_2 is portrayed in **Figure 34(b)**; it shows a uniform porosity distribution over the glass substrate [122]. The thickness of 146 ± 3 nm, it is composed of nanoparticles of 12 ± 3 nm and has a grid-like structure. The pores have an approximated diameter of 10 ± 2 nm. The Pluronic F127 make possible the homogeneous distribution of the porosity, because these co-polymer is used as pore-forming agent. The high porosity is associated with a high surface area, which is 74.7 ± 0.2 m^2/g. The surface area value is lower than the bioinspired N-TiO_2 but is higher that the value reported for Degussa P25 TiO_2.

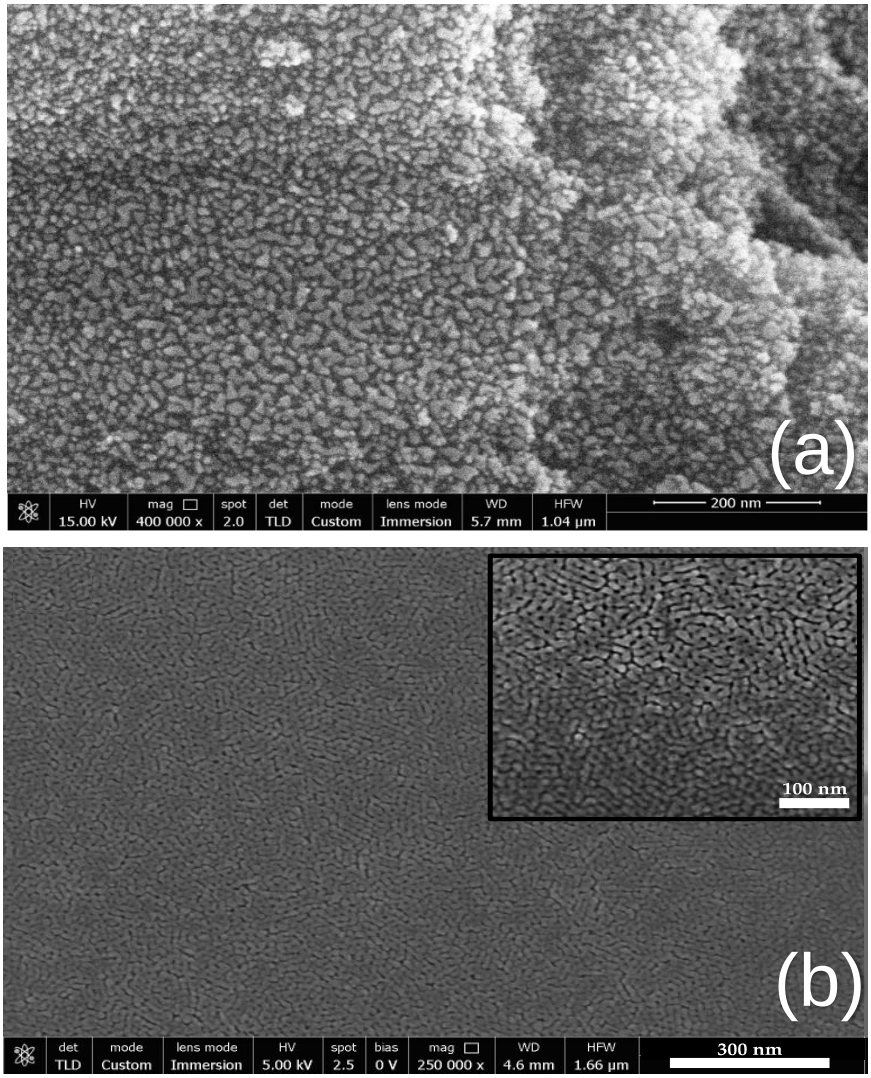

Figure 34. FEG-SEM micrographs of the N-TiO_2 bioinspired (a) and sol gel derived (b) coating.

7.4.2 Photocatalytic test with the semiconductors in the form of coatings.

The previous N-TiO_2 semiconductors in the form of films were used for the photocatalytic degradation of four microplastics pollutant models.

In **Figure 35** is the degradation plot (in terms of mass loss) for the four contaminant models using the mesoporous film. It can be observed that there is an effect of the particle size and type of contaminant in the mass loss process due to photocatalytic degradation

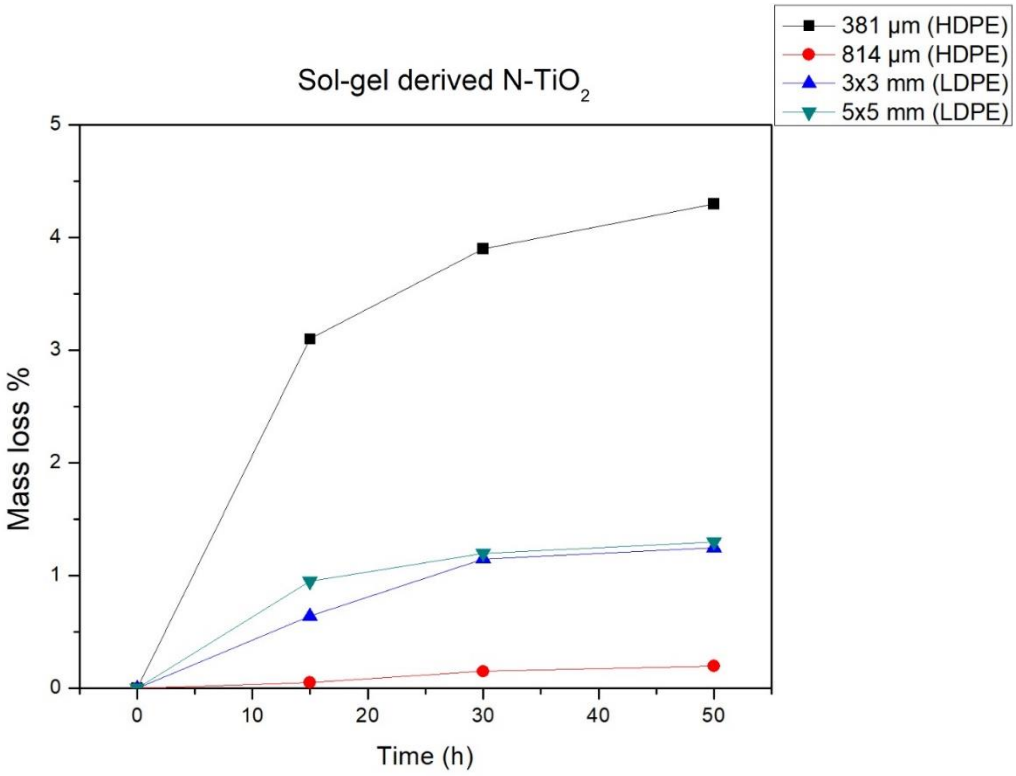

Figure 35. Mass loss after 50 h of photocatalysis using the mesoporous N-TiO_2 coating.

In the figure, the plots that corresponds to the LDPE shows that 1% of microplastics were degraded after 50 h of visible irradiation. The particle size of LDPE does not influence degradation. The low degradation is owing to the physical morphology of LDPE these were agglomerated in the surface. These

agglomerations avoid the interaction of light with the N-TiO_2 film and it may alter the diffusion of oxygen from air into the liquid phase limiting the generation of hydroxyl radicals for degradation, as it is illustrated in **Figure 36.**

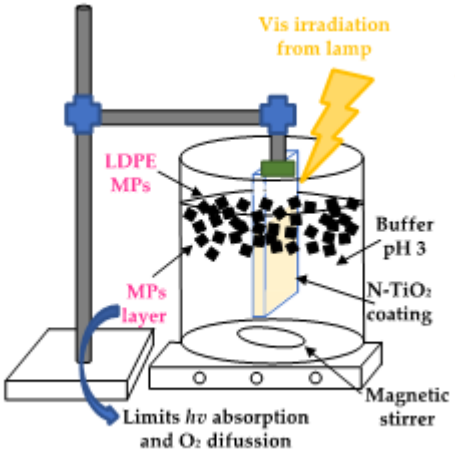

Figure 36. Formation of a LDPE MP's layer.

The trend of deterioration in HDPE by the same film is influenced by particle size. Degradation of the smaller microplastic after 50 h of photocatalysis is almost four times larger than the one of a bigger size. This result can be explained by the higher surface area to volume ratio of the smallest microplastic, which allows a better interaction of the hydroxyl radicals from the semiconductor with their surface, which in turn promotes degradation. Also, it is important to state that when a semiconductor is deposited on a substrate the superficial area of the photocatalyst is not totally used, these explain the limited degradation after 50 h. It is known the influence of the pH in degradation of microplastics [108], however in this study the pH did not have a great effect in degradation due to deposition of the semiconductor in a substrate and the environmental conditions (temperature).

The results for the bioinspired film are portrayed in **Figure 37**. In the case of the sol gel derived N-TiO_2 sample, degradation of the HDPE is higher than that obtained for the LDPE.

The results for the bioinspired film are portrayed in figure 37. Due to technical problems, only the experiments with the biggest microplastics with each type of polymer were performed. In the case of the mesoporous sample, degradation of the HDPE is higher than that obtained for the LDPE. The low degradation is owing to the physical morphology of LDPE these were agglomerated in the surface. These agglomerations avoid the interaction of light with the N-TiO_2 film, limiting the generation of hydroxyl radicals for degradation.

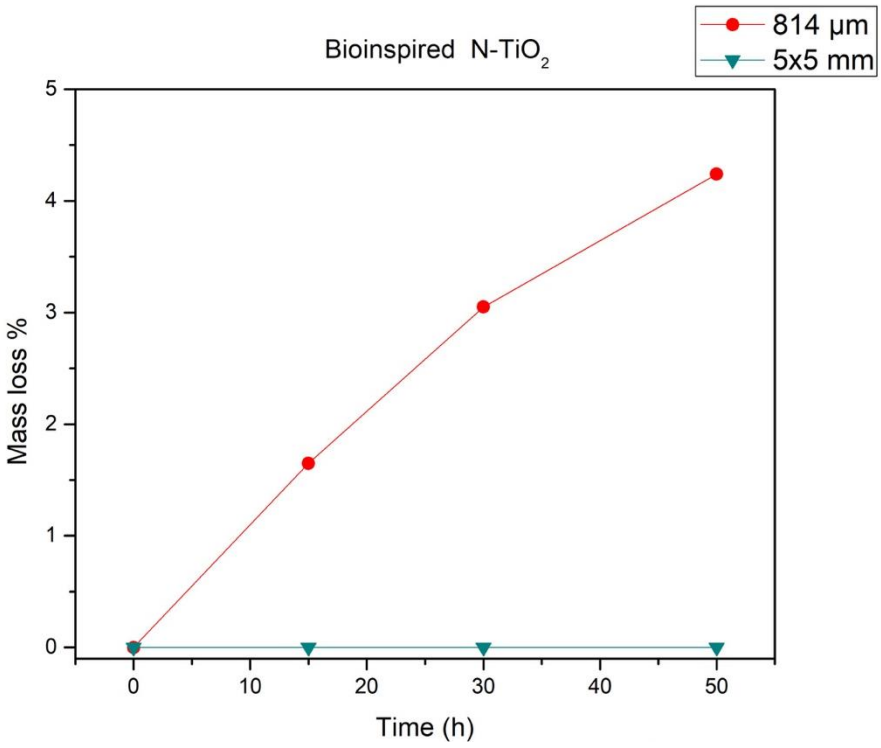

Figure 37. Mass loss after 50 h of photocatalysis with microplastics using the bioinspired N-TiO_2 coating.

7.4.3 Photocatalytic test with the semiconductors in the form of powders.

As stated before, the preliminary tests using the semiconductors in the form of powders were only performed for the film-shaped microplastics, as the research group has experimental evidence that the photocatalysis of spherical particles using a semiconductor in the form of powder is possible. With these conditions, mass losses up to 70% can be achieved depending of the reaction conditions. Further information [67,108].

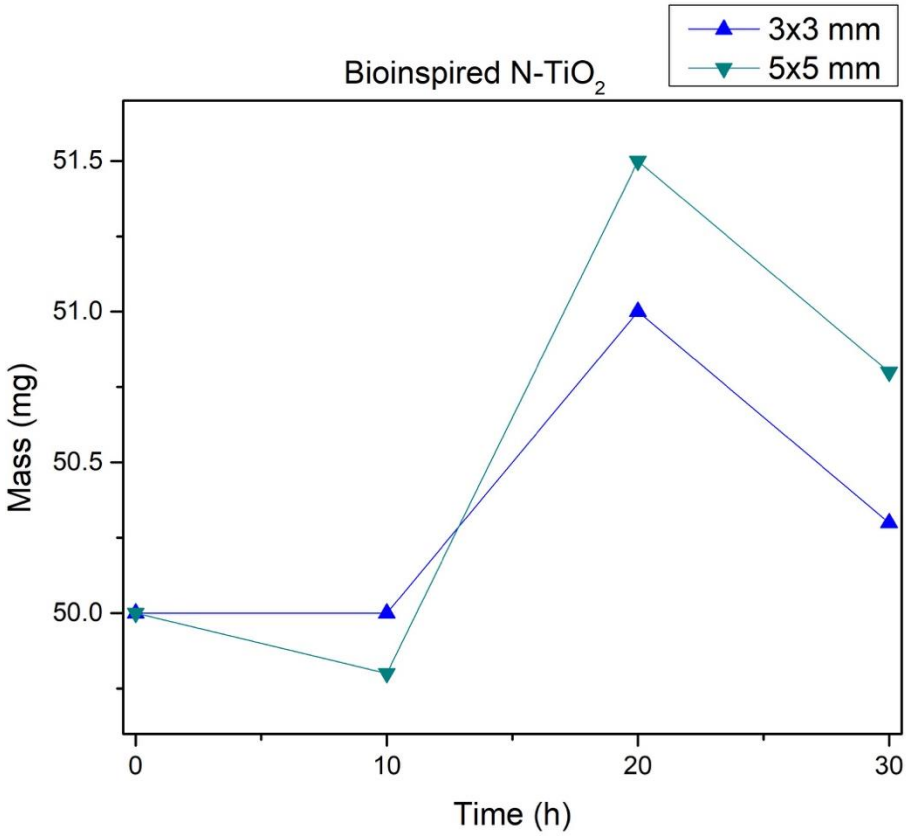

Figure 38. Changes in mass obtained during the photocatalytic degradation tests of the LDPE microplastics using both semiconductors.

Figure 38 shows the changes in the mass of the microplastics obtained during the photocatalytic degradation tests of the LDPE films using only one

semiconductor the bioinspired N-TiO_2 as powders. As observed in the plots, for all samples, mass increases with time.

It was visually confirmed during experiment by sight and optical micrography that the semiconductor powder was deposited over the LDPE films during the experiments. To avoid this deposition, the microplastics were repeatedly washed with distilled water and subjected to ultrasound treatment to remove the semiconductor from the LDPE films. However, no one of these approaches worked and the mass of the microplastics registered after photocatalysis was always higher than their initial mass.

From the results obtained from the preliminary photocatalytic tests, it was found that the LDPE microplastics, in both sizes, are not adequate for testing the photocatalytic activity of semiconductors, at least with the methodology used in this work. Additionally, comparing the results obtained here with those previously reported by the research group, it was found that performing photocatalysis with the semiconductor in the form of powders should lead to higher photocatalytic degradation of microplastics, as the system takes advantage of the whole surface area of the semiconductor, and the generation of the OH radicals for degradation is maximized.

Thus, for testing the photocatalytic activity of the biomineralized materials, the following conditions were selected: semiconductors in the form of powders and HDPE microplastics in two sizes (381 and 876 μm). Additionally, the test was performed in distilled water with pH = 7 ± 1. This was done to avoid the modification of the surface chemical composition of the biomineralized semiconductors (as they were prepared in a “natural” environment, where they were in contact with the organic matrix of the oysters).

7.5 Photocatalysis with biomineralized semiconductors.

Before testing the photocatalytic activity of the new semiconductors, photolysis of the of the model pollutants are usually were carried out in a closed

reactor chamber at room temperature (20 ± 3 °C), with a pH of 7, by just the radiation of the lamp for 30 h to study the influence of the conditions. In this work because of the problems caused by the sanitary emergency, the photolysis experiments couldn't be concluded. However, according to bibliography and other results already published by the research group [67,108], the mass loss plot portrayed in **Figure 39** was build.

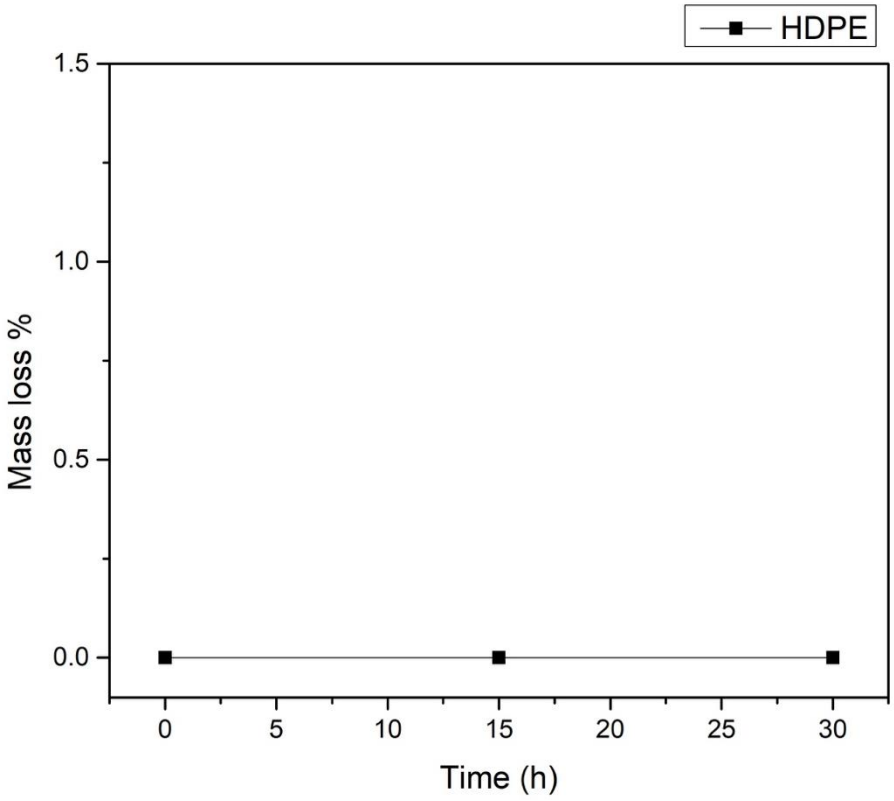

Figure 39. Mass loss of HDPE microplastics (814 μm) after 30 h of photolysis.

According to **Figure 39**, the mass of the HDPE microplastics do not change after 30 hours of radiation. This result is not surprising, it is well known the high

durability of PE and HDPE [61,108]. Indeed, this characteristic of high durability of the PE plastic is promoting its persistence in the environment.

Figure 40 shows the degradation plots (in terms of mass loss) for the HDPE microplastics of the smallest size (381.87 μm). The microplastics subjected to photocatalysis by the amorphous TiO_2 precursor (not subjected to biomineralization) presented a 5.89% of mass loss after 30 h of visible irradiation. On the other hand, the HDPE microplastics subjected to photocatalysis by the PS32N and PS90N semiconductors presented mass losses of 26.93% and 23.76%, respectively.

The general mechanism proposed for PE degradation are present in the next equations (equations. 8 - 12).

$$(-CH_2CH_2-)_n + OH^{\bullet} \rightarrow (-{}^{\bullet}CHCH_2-)_n + H_2O \qquad \text{Equation 8}$$

$$(-{}^{\bullet}CHCH_2-)_n + O_2 \rightarrow (-CH_2-HCOO^{\bullet}-CH_2)_n \qquad \text{Equation 9}$$

$$(-CH_2-HCOO^{\bullet}-CH_2)_n + (-CH_2CH_2-)_n \rightarrow (-CH_2-HCOOH-CH_2-)_n + (-{}^{\bullet}CHCH_2-)_n$$

Equation 10

$$(-CH_2-HCOOH-CH_2-)_n \rightarrow (-CH_2-HCO^{\bullet}-CH_2-)_n + OH^{\bullet} \qquad \text{Equation 11}$$

$$(-CH_2-HCO^{\bullet}-CH_2-)_n + (-CH_2CH_2-)_n \rightarrow (-{}^{\bullet}CHCH_2-)_n + (-CH_2-HCOH-CH_2-)_n$$

Equation 12

According to Equation (8), degradation initiate when the photogenerated hydroxyl radicals generate polyethylene alkyl radicals at the frail spots of the

polymeric chains [65]. The reaction of the alkyl radical $(-^{\bullet}CHCH_2-)_n$ with oxygen promote the propagation of degradation by forming a peroxy radical $(-CH_2-HCOO^{\bullet}-CH_2)_n$ (Equation (9)). This latter abstracts an hydrogen atom from another polymer chain to form the hydroperoxide specie $(-CH_2-HCOOH-CH_2-)_n$ (Equation (10)). Equation (11) shows that once hydroperoxide is formed is further cleavaged into two new free oxy ($(-CH_2-HCO^{\bullet}-CH_2-)_n$) and hydroxyl ($OH^{\bullet}$) radicals by the scission of the weak O–O bond [123,124]. These radicals are far more reactive than peroxy radicals [123] and can abstract labile hydrogens from other polymer chains (Equations (8) and (12)).

The mass loss can be explained in the following way; even when the biomineralized semiconductors did not express the result expected. These semiconductors have better properties than the amorphous and interact better with this size of microplastic. In the case of the amorphous, the band-gap is higher than the 32N, but degradation is higher with the samples biomineralized. These mean that biomineralization enhances the properties of the semiconductor TiO_2.

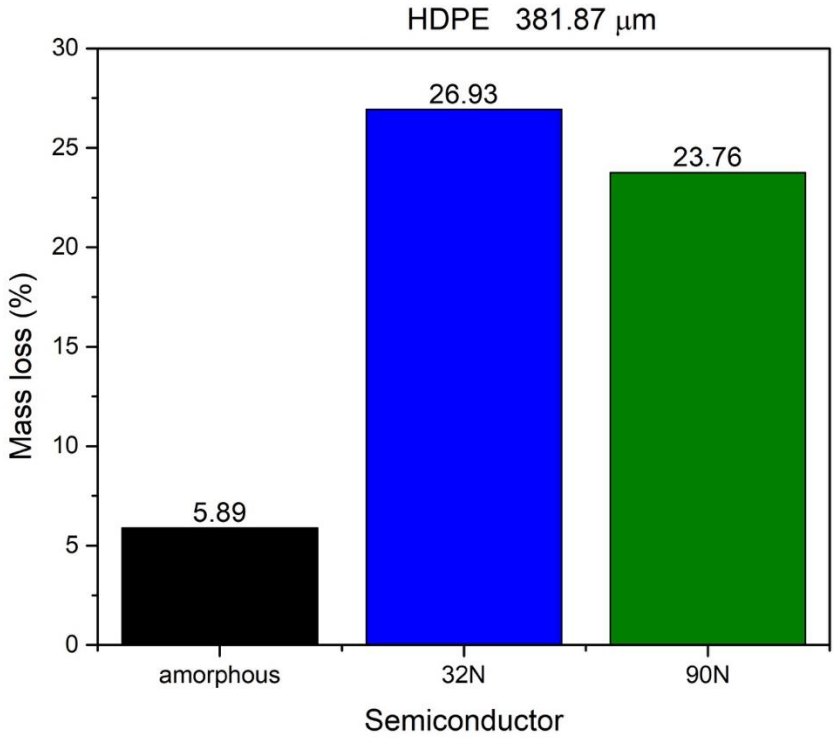

Figure 40. Mass loss after 30 h of photocatalysis for HDPE 381.87 µm.

Figure 41 display the mass loss for each semiconductor after 30 h for HDPE with the size 876. 26 µm. A higher degradation can be observed in sample 90N with 19.51%, then is amorphous with 3.98%, and at least is sample 32N with 3.50% of mass loss. This result corroborates that higher degradation is observed with smaller size particle. Also, it is shown that biomineralization change in a certain way, the properties of the semiconductor favoring the degradation.

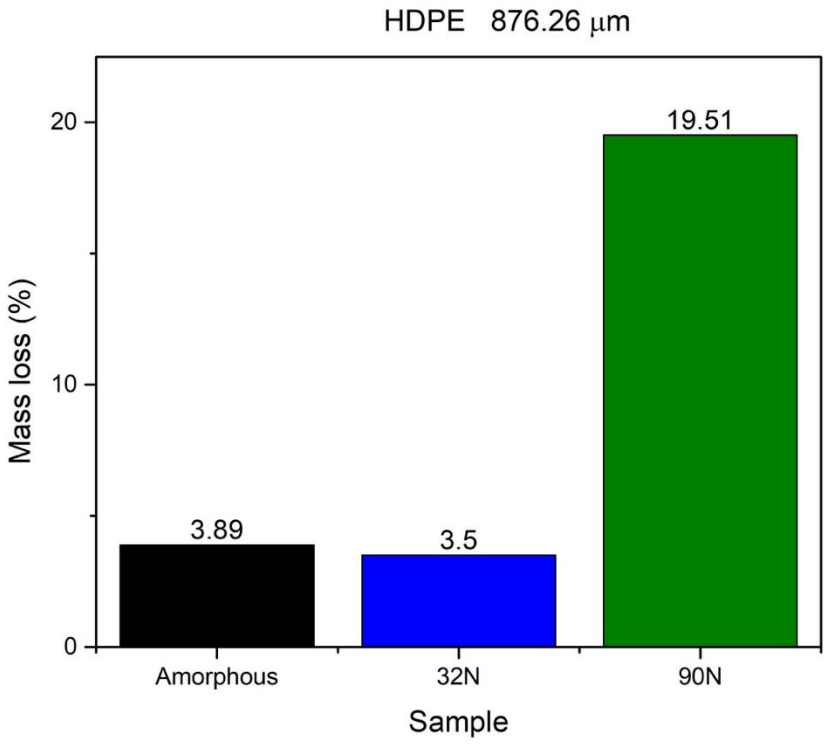

Figure 41. Mass loss after 30 h of photocatalysis for HDPE 876.26 μm.

After photocatalytic experiments, optical micrography of HDPE was made to corroborate degradation. **Figure 42** (a) shows the pristine HDPE of size 381.87 μm, also in the figure (b-d) are the microplastics after treatment for 30 h with a semiconductor. It is shown that HDPE with treatment has powder on the surface; this is more visible in the amorphous treatment (b). Part of the semiconductor is attached to the pollutant, which influences the weight and the total mass loss.

Figure 42 (c) and (d) represent the treatment with sample PS32N and PS90N, respectively. In the micrography, the HDPE are pulverized in some proportion, this fragmentation can be associated with degradation. In both cases, there are some semi-spherical microplastics almost complete but with physical

changes. These types of physical damage have been usually associated with degradation of plastic. In all samples treated with the biomineralized semiconductor a physical change appears in the microplastics.

The high probability of collision is improved by the continuous stirring of the HDPE microplastics, and the N-TiO_2 adsorbed hydroxyl radicals. During those collisions, hydroxyl radicals can interact with microplastics and promote degradation, and it can be seen the fragmentation in the figure. The fragmentation changes the mechanical properties of plastic.

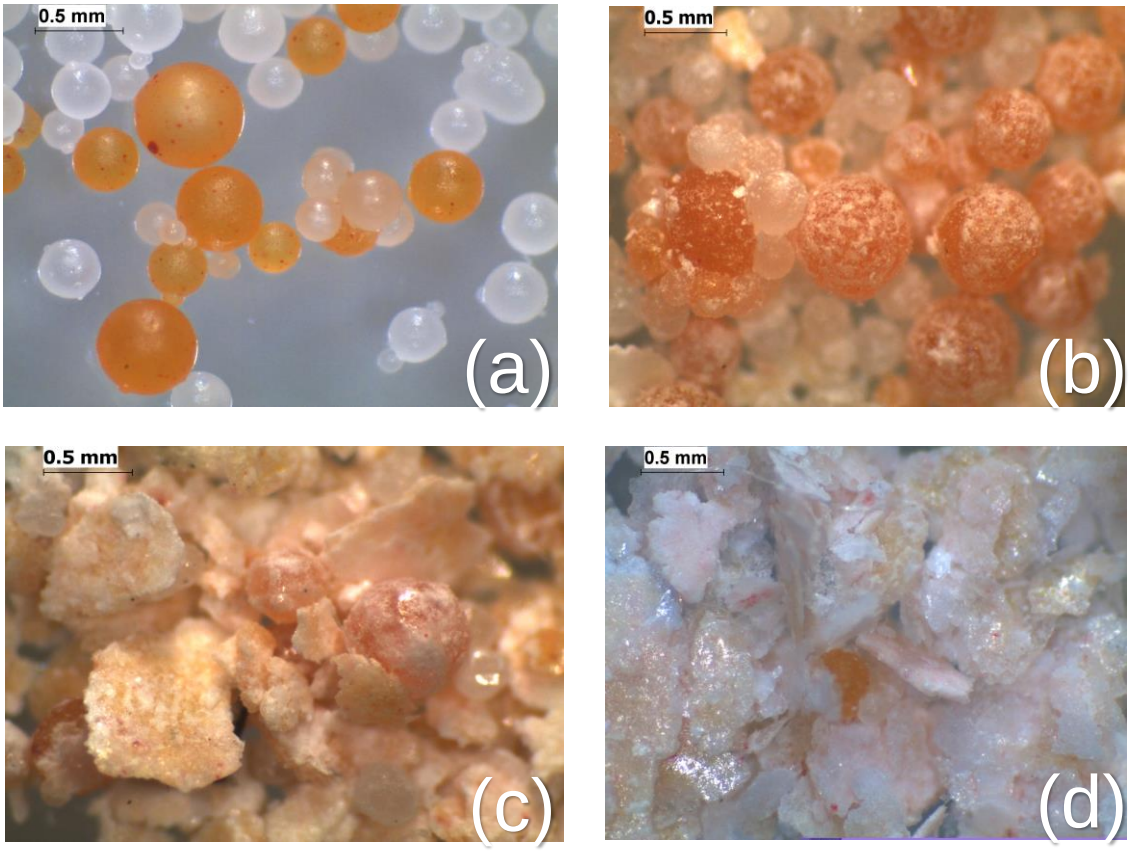

Figure 42. Optical micrography of pristine HDPE (381.87 μm) (a) and after irradiation for 30 h with different semiconductors (b) amorphous, (c) PS32N and (d) PS90N.

Figure 43 shows the pristine HDPE of size 876.26 μm (a), and this microplastics after 30 h of irradiation with a semiconductor (b-d). The HDPE after the experiment using the amorphous (b) and PS32N (c) are alike, both shown adhesion of semiconductor and no fragmentation. In the case of the microplastic with PS32N (c), the addition of the semiconductor to the surface look more uniform, and the pattern is smaller than the amorphous (b), this can be explained with the different optical properties between the semiconductors. The HDPE with 90N (d) shows fragmentation and deformation of the spherical shape of HDPE; this can be explained with the constant collision between the HDPE and PS90N, absorbing hydroxyl radicals that benefit degradation.

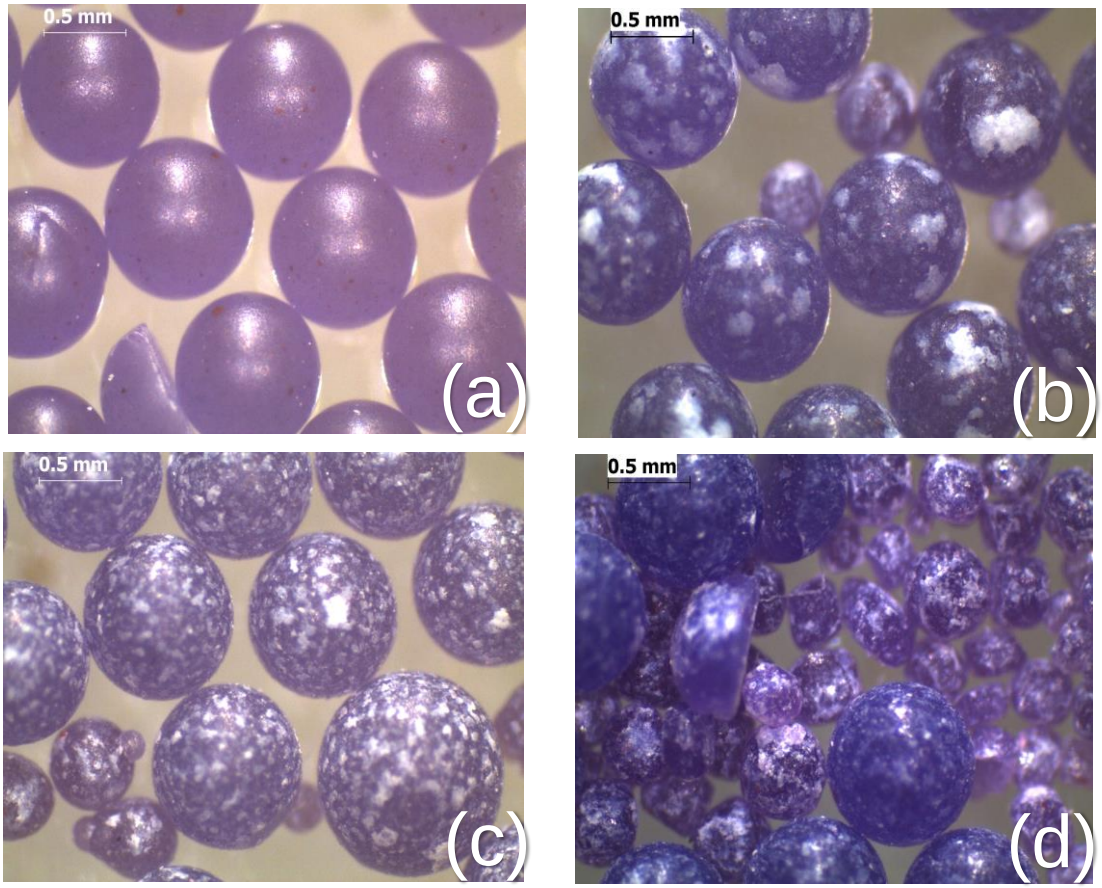

Figure 43. Optical micrography of pristine HDPE (876.26 µm) (a) and after irradiation for 30 h with different semiconductors (b) amorphous, (c) PS32N and (d) PS90N.

The microstructure changes in HDPE microplastics after treatment were measured with ATR-FTIR. The spectrums are present in **Figures 44 and 45**, they showed the HDPE of the size 381.87 µm and 876.26 µm respectively, after irradiation for 30 h with a semiconductor.

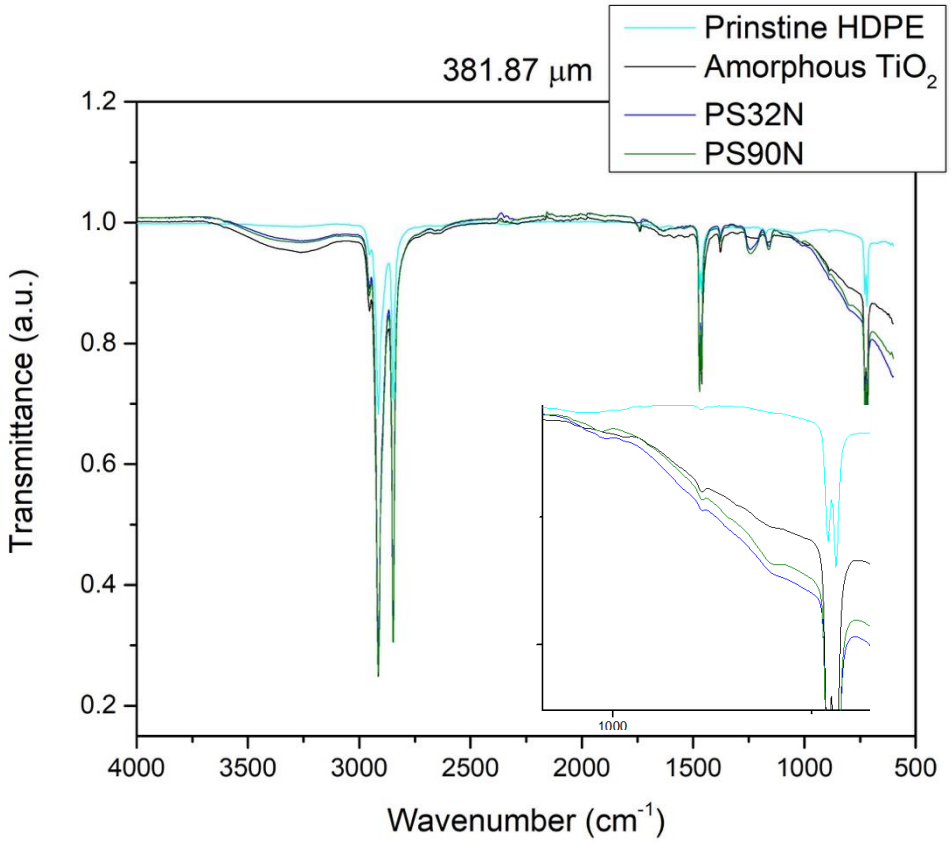

Figure 44. ATR-FTIR for HDPE microplastics (381.87 μm), and after 30 h of photocatalytic degradation with different semiconductors.

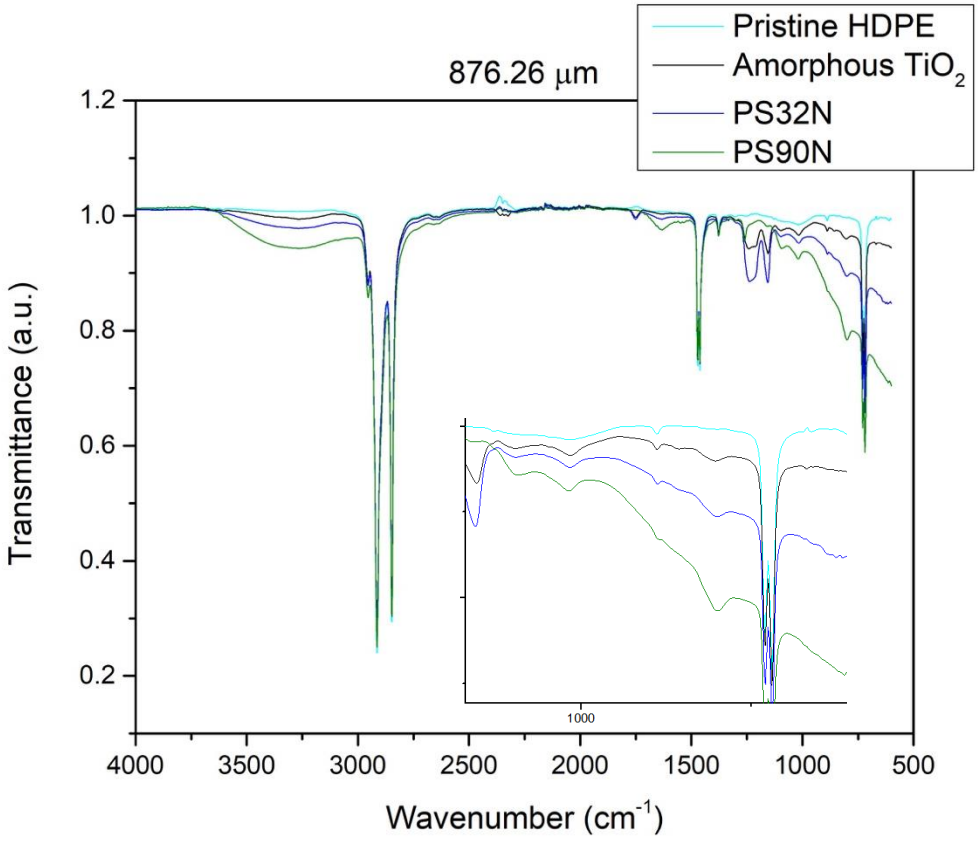

Figure 45. ATR-FTIR for HDPE (876.26 μm) microplastics and after 30 h of photocatalytic degradation with different semiconductors.

An indicator of the degradation of polyethene is the vinyl index since ketones, aldehydes and carboxylic acids are formed the late steps of the photodegradation process. Previous reports suggest that photo-oxidation of ketones results in the formation of unsaturated vinylidene and vinyl groups at 888 cm^{-1} and 899 cm^{-1}. In both ATR-FTIR, these bands are more intense [109,110].

It was used the Equation 4 and 5 to calculate the vinyl index, the absorption band located at 899 cm^{-1} was used, and the reference band is located at 2920

cm^{-1}. And to calculate the unsaturated vinylidene, the absorption band located at 888 cm^{-1} and the same reference band was used. The calculated vinyl index is presented in Table 7 and 8 for HDPE of the size 381.87 µm and 876.26 µm, respectively.

$$\text{Vinyl index (VI)} = A_{899}/A_{2920} \qquad \text{Equation 4}$$

$$\text{Unsaturated vinylidene index (UVI)} = A_{888}/A_{2920} \qquad \text{Equation 5}$$

Table 7. Calculation of VI and UVI for HDPE 381.87 µm.

Treatment	Mass loss (%)	(VI)	(UVI)
Pristine	0	0.041	0.052
Amorphous	5.89	0.069	0.081
PS32N	26.93	0.097	0.109
PS90N	23.76	0.080	0.093

Table 8. Calculation of VI and UVI for HDPE 876.26 µm.

Treatment	Mass loss (%)	(VI)	(UVI)
Pristine	0	0.001	0.009
Amorphous	3.89	0.018	0.028
PS32N	3.50	0.061	0.072
PS90N	19.51	0.125	0.141

According to the results from table 6 and 7, the vinyl index calculations are in concordance with the mass loss obtained in the experiments. We can conclude that with higher mass loss yields a higher vinyl index is expressed, the vinyl index is a useful tool to determine the degradation. Nevertheless, it doesn't have into account if the degradation is in early steps (formation of hydroxides) or if there was complete mineralization (CO_2 and H_2O).

To summarize the results from the preliminary tests, the most effective way to perform the photocatalytic degradation of PE microplastics is in aqueous medium and using the semiconductors as powders. Also, it was shown that using HDPE involves less experimental errors, because this pollutant model has a practical size and does not require a high quantity of sample to reach a specific weight. These characteristics improve the diffusion of visible light and O_2 during the photocatalytic experiments.

In summarize the characterization of the biomineralized semiconductors shown that even though complete crystallization of anatase phase was not archived, the materials are photocatalytically active in visible light. This was explained by the changes in the functional groups of the materials during incubation inside the oysters, which promoted the incorporation of nitrogen into the materials.

Summarizing the photocatalytic results it was shown that using the biomineralized semiconductors, it is possible to reach a mass loss of 26.93% and 19.51% of HDPE microplastics with particle sizes of 381.87 μm and 876.26 μm,

respectively. These results are in concordance with the vinyl index and the optical micrographs, which were used to further confirm degradation.

CHAPTER 8

8. CONCLUSIONS

Microbeads are present in different facial scrub commercially available in supermarkets and beauty shops in Mexico. The microbeads were identified as HDPE small microplastics of different diameters 814.21, 876.26 and 381.87 µm.

From the photolysis experiments of the PE microplastics, it was seen that it is a stable polymer with high durability under visible light irradiation. No high degradation evidence was found in the obtained results.

From the preliminary test, it was confirmed that, both N-TiO_2 materials contain anatase crystalline phase and absorb visible light. In the case of the HDPE MP's, their size affects degradation (sol gel derived sample) with larger particle size, lower degradation.

In the same preliminary test, it was concluded that the bioinspired N-TiO_2 film degrades 4.4% of the HDPE MP's in 50h of visible radiation. No degradation was obtained for the LDPE MP's, probably due to the limited interaction of the N-TiO_2 film with light. With the mesoporous N-TiO_2 film degrades 1.3% of the LDPE MP's and 4.3% of HDPE in 50h of visible light radiation and it was observed that LDPE MP's particle size does not influence degradation.

The precursor's tablets were successfully implanted in *Pteria sterna* to archive biomineralization. Even though after characterization, results showed some amorphous phase remains at the end of incubation time, but the biomineralization enhances the properties of TiO_2 that contribute to the degradation of HDPE: The FTIR analysis showed the presence of nitrogen, and the Eg value indicate that samples biomineralized are active under visible light.

For the photocatalysis experiments with HDPE of size 381.87 μm and biomineralized semiconductors, the results showed higher degradation in sample biomineralized PS32N with 26.96%, after sample PS90N with 23.76% and then amorphous precursor with 5.89%. These results confirm that biomineralization enhanced properties of the semiconductor TiO_2 showing 4.5 times more degradation in the case of PS32N.

In the photocatalysis test with HDPE of size 876.26 µm and biomineralized semiconductors, the results displayed a higher degradation in sample biomineralized PS90N with 19.51% of degradation, after the amorphous precursor with 3.89%, and then sample PS32N with 3.50%. The enhanced properties of the semiconductor PS90N showed 5.5 times more degradation than other samples

For the experiments with different semiconductors biomineralized it can be concluded size influence degradation, with larger particle size lower degradation.

Photocatalytic degradation of microplastics was attributed to the action of hydroxyl radicals, where the decomposition of hydroperoxides took place.

REFERENCES

[1] D. Eerkes-Medrano, R.C. Thompson, D.C. Aldridge, Microplastics in freshwater systems: A review of the emerging threats, identification of knowledge gaps and prioritisation of research needs, Water Res. 75 (2015) 63–82. https://doi.org/10.1016/j.watres.2015.02.012.

[2] D.A. Segar, E.S. Segar, Introduction to Ocean Sciences, 2007.

[3] UNEP-MAP, Assessment of the Status of Marine Litter in the Mediterranean, (2011) 25–27.

[4] B. Singh, N. Sharma, Mechanistic implications of plastic degradation, Polym. Degrad. Stab. 93 (2008) 561–584. https://doi.org/10.1016/J.POLYMDEGRADSTAB.2007.11.008.

[5] D.A. Segar, Introduction to Ocean Sciences, Fourth Edi, 2018.

[6] A.A. Koelmans, E. Besseling, W.J. Shim, T. Kiessling, L. Gutow, M. Thiel, Marine Anthropogenic Litter, 2015. https://doi.org/10.1007/978-3-319-16510-3.

[7] UNEP, Marine Litter Assessment in the Mediterranean, 2015.

[8] R.C. Thompson, Y. Olsen, R.P. Mitchell, A. Davis, S.J. Rowland, A.W.G. John, D. Mcgonigle, A.E. Russell, Lost at Sea : Where Is All the Plastic ?, Science (80-.). 304 (2004) 2004.

[9] R. Geyer, J.R. Jambeck, K.L. Law, Production, use, and fate of all plastics ever made, Sci. Adv. 3 (2017) e1700782. https://doi.org/10.1126/sciadv.1700782.

[10] A.A. Horton, A. Walton, D.J. Spurgeon, E. Lahive, C. Svendsen, Microplastics in freshwater and terrestrial environments: Evaluating the current understanding to identify the knowledge gaps and future research priorities, Sci. Total Environ. 586 (2017) 127–141.

https://doi.org/10.1016/j.scitotenv.2017.01.190.

[11] H. Kershaw, P.J., Leslie, GESAMP Working Group 40 – Sources, fate and effects of micro-plastics in the marine environment- a global assessment: Report of the Inception Meeting, 13–15th March 2012, UNESCO-IOC, Paris, pp. 45., Paris, 2012.

[12] E. Huerta Lwanga, J. Mendoza Vega, V. Ku Quej, J. de los A. Chi, L. Sanchez del Cid, C. Chi, G. Escalona Segura, H. Gertsen, T. Salánki, M. van der Ploeg, A.A. Koelmans, V. Geissen, Field evidence for transfer of plastic debris along a terrestrial food chain, Sci. Rep. 7 (2017) 14071. https://doi.org/10.1038/s41598-017-14588-2.

[13] M. Cole, P. Lindeque, C. Halsband, T.S. Galloway, Microplastics as contaminants in the marine environment: A review, Mar. Pollut. Bull. 62 (2011) 2588–2597. https://doi.org/10.1016/J.MARPOLBUL.2011.09.025.

[14] H.S. Auta, C.. Emenike, S.. Fauziah, Distribution and importance of microplastics in the marine environment: A review of the sources, fate, effects, and potential solutions, Environ. Int. 102 (2017) 165–176. https://doi.org/10.1016/j.envint.2017.02.013.

[15] S. Lambert, M. Wagner, Microplastics Are Contaminants of Emerging Concern in Freshwater Environments: An Overview, in: 2018: pp. 1–23. https://doi.org/10.1007/978-3-319-61615-5_1.

[16] N. Serpone, Photocatalysis, in: Kirk-Othmer Encycl. Chem. Technol., John Wiley & Sons, Inc., Hoboken, NJ, USA, 2000. https://doi.org/10.1002/0471238961.1608152019051816.a01.

[17] S. Ziajahromi, P.A. Neale, L. Rintoul, F.D.L. Leusch, Wastewater treatment plants as a pathway for microplastics: Development of a new approach to sample wastewater-based microplastics, Water Res. 112 (2017) 93–99. https://doi.org/10.1016/j.watres.2017.01.042.

[18] R. Ameta, S.C. Ameta, Photocatalysis : principles and applications, 2017.

https://doi.org/10.15713/ins.mmj.3.

[19] E.I. Cedillo-González, R. Riccò, M. Montorsi, M. Montorsi, P. Falcaro, C. Siligardi, Self-cleaning glass prepared from a commercial TiO2 nano-dispersion and its photocatalytic performance under common anthropogenic and atmospheric factors, Build. Environ. 71 (2014) 7–14. https://doi.org/10.1016/J.BUILDENV.2013.09.007.

[20] E.I. Cedillo-González, C. Mugoni, M. Montorsi, C. Siligardi, Evaluation of the correlations between temperature, humidity, incident UV light and the photocatalytic activity of TiO2 films using a rationale approach, Appl. Surf. Sci. 378 (2016) 73–79. https://doi.org/10.1016/J.APSUSC.2016.03.202.

[21] J. Zhang, Q. Xu, Z. Feng, M. Li, C. Li, Importance of the Relationship between Surface Phases and Photocatalytic Activity of TiO2, Angew. Chemie. 120 (2008) 1790–1793. https://doi.org/10.1002/ange.200704788.

[22] M.N. Iman Amir, N.M. Julkapli, S. Bagheri, A.T. Yousefi, TiO2 hybrid photocatalytic systems: impact of adsorption and photocatalytic performance, Rev. Inorg. Chem. 35 (2015) 151–178. https://doi.org/10.1515/revic-2015-0005.

[23] J. Cai, J. Shen, X. Zhang, Y.H. Ng, J. Huang, W. Guo, C. Lin, Y. Lai, Light-Driven Sustainable Hydrogen Production Utilizing TiO2 Nanostructures: A Review., Small Methods. (2018) 1800184. https://doi.org/10.1002/smtd.201800184.

[24] S.A. Ansari, M.M. Khan, M.O. Ansari, M.H. Cho, Nitrogen-doped titanium dioxide (N-doped TiO2) for visible light photocatalysis, New J. Chem. 40 (2016) 3000–3009. https://doi.org/10.1039/c5nj03478g.

[25] J. Xie, H. Xie, B.L. Su, Y.B. Cheng, X. Du, H. Zeng, M. Wang, W. Wang, H. Wang, Z. Fu, Mussel-Directed Synthesis of Nitrogen-Doped Anatase TiO2, Angew. Chemie - Int. Ed. 55 (2016) 3031–3035. https://doi.org/10.1002/anie.201509906.

[26] Q. Feng, Principles of calcium-based biomineralization, Prog. Mol. Subcell. Biol. 52 (2011) 141–197. https://doi.org/10.1007/978-3-642-21230-7_6.

[27] UNEP, Recommended citation : Acknowledgements :, 2016.

[28] A.L. Andrady, Microplastics in the marine environment, Mar. Pollut. Bull. 62 (2011) 1596–1605. https://doi.org/10.1016/J.MARPOLBUL.2011.05.030.

[29] R.C. Thompson, S.H. Swan, C.J. Moore, F.S. vom Saal, Our plastic age, Philos. Trans. R. Soc. B Biol. Sci. 364 (2009) 1973–1976. https://doi.org/10.1098/rstb.2009.0054.

[30] U.N.E. Programme, Marine Plastic Debris and Microplastics: Global Lessons and Research to Inspire Action and Guide Policy Change, 2016.

[31] INEGI, Anuario estadístico y geográfico de los Estados Unidos Mexicanos 2017 | Enhanced Reader, n.d.

[32] J. Zalasiewicz, C.N. Waters, J.A. Ivar do Sul, P.L. Corcoran, A.D. Barnosky, A. Cearreta, M. Edgeworth, A. Gałuszka, C. Jeandel, R. Leinfelder, J.R. McNeill, W. Steffen, C. Summerhayes, M. Wagreich, M. Williams, A.P. Wolfe, Y. Yonan, The geological cycle of plastics and their use as a stratigraphic indicator of the Anthropocene, Anthropocene. 13 (2016) 4–17. https://doi.org/10.1016/J.ANCENE.2016.01.002.

[33] R. Geyer, B. Kuczenski, T. Zink, A. Henderson, Common Misconceptions about Recycling, J. Ind. Ecol. 20 (2016) 1010–1017. https://doi.org/10.1111/jiec.12355.

[34] E.L. Teuten, J.M. Saquing, D.R.U. Knappe, M.A. Barlaz, S. Jonsson, A. Björn, S.J. Rowland, R.C. Thompson, T.S. Galloway, R. Yamashita, D. Ochi, Y. Watanuki, C. Moore, P.H. Viet, T.S. Tana, M. Prudente, R. Boonyatumanond, M.P. Zakaria, K. Akkhavong, Y. Ogata, H. Hirai, S. Iwasa, K. Mizukawa, Y. Hagino, A. Imamura, M. Saha, H. Takada, Transport and release of chemicals from plastics to the environment and to wildlife, Philos. Trans. R. Soc. B Biol. Sci. 364 (2009) 2027–2045.

https://doi.org/10.1098/rstb.2008.0284.

[35] M.I. Ali, Q. Perveen, B. Ahmad, I. Javed, R. Razi-Ul-Hussnain, S. Andleeb, N. Atique, P.B. Ghumro, S. Ahmed, A. Hameed, Studies on biodegradation of cellulose blended polyvinyl chloride films, Int. J. Agric. Biol. 11 (2009) 577–580.

[36] R. V. Moharir, S. Kumar, Challenges associated with plastic waste disposal and allied microbial routes for its effective degradation: A comprehensive review, J. Clean. Prod. 208 (2019) 65–76. https://doi.org/10.1016/j.jclepro.2018.10.059.

[37] A.E. Schwarz, T.N. Ligthart, E. Boukris, T. van Harmelen, Sources, transport, and accumulation of different types of plastic litter in aquatic environments: A review study, Mar. Pollut. Bull. 143 (2019) 92–100. https://doi.org/10.1016/j.marpolbul.2019.04.029.

[38] M.C. Rillig, Microplastic in Terrestial Ecosystems and the Soil?, Environ. Sci. Technol. 46 (2012) 6453–6454. https://doi.org/10.1021/es302011r.

[39] GESAMP, Science for Sustainable Oceans, (2015) 98.

[40] GESAMP Working Group 40, Sources, Fate and Effects of Microplastics in the Marine Environment: Part 2 of a Global Assessment - Science for Sustainable Oceans, Int. Marit. Organ. (2016) 1–217.

[41] M. Bläsing, W. Amelung, Science of the Total Environment Plastics in soil : Analytical methods and possible sources, Sci. Total Environ. 612 (2018) 422–435. https://doi.org/10.1016/j.scitotenv.2017.08.086.

[42] T. Dixon, A.C.-M.P. Bulletin, undefined 1977, Discarded containers on a Kent beach, Elsevier. (n.d.).

[43] P.G. Ryan, C.J. Moore, J.A. Van Franeker, C.L. Moloney, Monitoring the abundance of plastic debris in the marine environment, Philos. Trans. R. Soc. B Biol. Sci. 364 (2009) 1999–2012. https://doi.org/10.1098/rstb.2008.0207.

[44] P. Denuncio, R. Bastida, M. Dassis, G. Giardino, M. Gerpe, D. Rodríguez, Plastic ingestion in Franciscana dolphins, Pontoporia blainvillei (Gervais and d'Orbigny, 1844), from Argentina, Mar. Pollut. Bull. 62 (2011) 1836–1841. https://doi.org/10.1016/j.marpolbul.2011.05.003.

[45] GESAMP, Sources, fate and effects of MP in the marine environment, 2015.

[46] F. Zhu, C. Zhu, C. Wang, C. Gu, Occurrence and Ecological Impacts of Microplastics in Soil Systems: A Review, Bull. Environ. Contam. Toxicol. 102 (2019) 741–749. https://doi.org/10.1007/s00128-019-02623-z.

[47] A.A. de Souza Machado, W. Kloas, C. Zarfl, S. Hempel, M.C. Rillig, Microplastics as an emerging threat to terrestrial ecosystems, Glob. Chang. Biol. 24 (2018) 1405–1416. https://doi.org/10.1111/gcb.14020.

[48] M.C. Rillig, A. Lehmann, A.A. Souza Machado, G. Yang, Microplastic effects on plants, New Phytol. 223 (2019) 1066–1070. https://doi.org/10.1111/nph.15794.

[49] D. Xanthos, T.R. Walker, International policies to reduce plastic marine pollution from single-use plastics (plastic bags and microbeads): A review, Mar. Pollut. Bull. 118 (2017) 17–26. https://doi.org/10.1016/j.marpolbul.2017.02.048.

[50] J.A. Ivar do Sul, M.F. Costa, M. Barletta, F.J.A. Cysneiros, Pelagic microplastics around an archipelago of the Equatorial Atlantic, Mar. Pollut. Bull. 75 (2013) 305–309. https://doi.org/10.1016/j.marpolbul.2013.07.040.

[51] E. Huerta Lwanga, B. Thapa, X. Yang, H. Gertsen, T. Salánki, V. Geissen, P. Garbeva, Decay of low-density polyethylene by bacteria extracted from earthworm's guts: A potential for soil restoration, Sci. Total Environ. 624 (2018) 753–757. https://doi.org/10.1016/j.scitotenv.2017.12.144.

[52] A. Löhr, H. Savelli, R. Beunen, M. Kalz, A. Ragas, F. Van Belleghem, Solutions for global marine litter pollution, Curr. Opin. Environ. Sustain. 28 (2017) 90–99. https://doi.org/10.1016/j.cosust.2017.08.009.

[53] Alberto Marinas Aramendia, Investigación Química Catálisis heterogénea y Química Verde, An. Quim. 103 (2007) 30–37.

[54] A. Zaleska, Doped-TiO2: A Review, Recent Patents Eng. 2 (2008) 157–164. https://doi.org/10.2174/187221208786306289.

[55] N. Patel, R. Jaiswal, T. Warang, G. Scarduelli, A. Dashora, B.L. Ahuja, D.C. Kothari, A. Miotello, Efficient photocatalytic degradation of organic water pollutants using V–N-codoped TiO2 thin films, Appl. Catal. B Environ. 150–151 (2014) 74–81. https://doi.org/10.1016/J.APCATB.2013.11.033.

[56] M.-Z. Ge, C.-Y. Cao, J.-Y. Huang, S.-H. Li, S.-N. Zhang, S. Deng, Q.-S. Li, K.-Q. Zhang, Y.-K. Lai, Synthesis, modification, and photo/photoelectrocatalytic degradation applications of TiO2 nanotube arrays: a review, Nanotechnol. Rev. 5 (2016) 75–112. https://doi.org/10.1515/ntrev-2015-0049.

[57] T.M. Dung Dang, D. Dam Le, V. Thang Chau, M. Chien Dang, Visible-light photocatalytic activity of N/SiO_2–TiO_2 thin films on glass, Adv. Nat. Sci. Nanosci. Nanotechnol. 1 (2010) 015004. https://doi.org/10.1088/2043-6254/1/1/015004.

[58] N.T. Phuong Mai, PHOTOCATALYTIC DEGRADATION OF PARAQUAT USING N-TiO2/SiO2 UNDER VISIBLE LIGHT, Vietnam J. Sci. Technol. 55 (2018) 277. https://doi.org/10.15625/2525-2518/55/4C/12164.

[59] Y.D. Hou, X.C. Wang, L. Wu, X.F. Chen, Z.X. Ding, X.X. Wang, X.Z. Fu, N-Doped SiO2/TiO2 mesoporous nanoparticles with enhanced photocatalytic activity under visible-light irradiation, Chemosphere. 72 (2008) 414–421. https://doi.org/10.1016/J.CHEMOSPHERE.2008.02.035.

[60] T.P. Ang, C.S. Toh, Y.-F. Han, Synthesis, Characterization, and Activity of Visible-Light-Driven Nitrogen-Doped TiO_2 −SiO_2 Mixed Oxide Photocatalysts, J. Phys. Chem. C. 113 (2009) 10560–10567. https://doi.org/10.1021/jp9000658.

[61] X. Zhao, Z. Li, Y. Chen, L. Shi, Y. Zhu, Enhancement of photocatalytic degradation of polyethylene plastic with CuPc modified TiO2 photocatalyst under solar light irradiation, Appl. Surf. Sci. 254 (2008) 1825–1829. https://doi.org/10.1016/J.APSUSC.2007.07.154.

[62] W. Fa, C. Yang, C. Gong, T. Peng, L. Zan, Enhanced Photodegradation Efficiency of Polyethylene-TiO 2 Nanocomposite Film with Oxidized Polyethylene Wax, (n.d.). https://doi.org/10.1002/app.32413.

[63] R.T. Thomas, V. Nair, N. Sandhyarani, TiO2nanoparticle assisted solid phase photocatalytic degradation of polythene film: A mechanistic investigation, Colloids Surfaces A Physicochem. Eng. Asp. 422 (2013) 1–9. https://doi.org/10.1016/j.colsurfa.2013.01.017.

[64] M.C. Ariza-Tarazona, J.F. Villarreal-Chiu, V. Barbieri, C. Siligardi, E.I. Cedillo-González, New strategy for microplastic degradation: green photocatalysis using a protein-based porous N-TiO2 semiconductor, in: CIMTEC Forum New Mater., Perugia, Italy, 2018.

[65] T.S. Tofa, K.L. Kunjali, S. Paul, J. Dutta, Visible light photocatalytic degradation of microplastic residues with zinc oxide nanorods, Environ. Chem. Lett. 17 (2019) 1341–1346. https://doi.org/10.1007/s10311-019-00859-z.

[66] T.S. Tofa, F. Ye, K.L. Kunjali, J. Dutta, Enhanced visible light photodegradation of microplastic fragments with plasmonic platinum/zinc oxide nanorod photocatalysts, Catalysts. 9 (2019). https://doi.org/10.3390/catal9100819.

[67] M.C. Ariza-Tarazona, EVALUATION OF N DOPED TiO2 PREPARED BY A BIOMINERALIZATION-INSPIRED ROUTE FOR THE PHOTOCATALYTIC DEGRADATION OF HDPE PRIMARY MICROPLASTICS PRESENT IN COMMERCIALLY AVAILABLE FACIAL SCRUBS, Universidad Autonoma de Nuevo León, 2018.

[68] J.O. Carneiro, V. Teixeira, P. Carvalho, S. Azevedo, N. Manninen, Self-

cleaning smart nanocoatings, in: Nanocoatings Ultra-Thin Film., Elsevier, 2011: pp. 397–413. https://doi.org/10.1533/9780857094902.2.397.

[69] A. Fujishima, X. Zhang, D.A. Tryk, TiO 2 photocatalysis and related surface phenomena, Surf. Sci. Rep. 63 (2008) 515–582. https://doi.org/10.1016/j.surfrep.2008.10.001.

[70] C. Byrne, G. Subramanian, S.C. Pillai, Recent advances in photocatalysis for environmental applications, J. Environ. Chem. Eng. 6 (2018) 3531–3555. https://doi.org/10.1016/j.jece.2017.07.080.

[71] H. De Lasa, B. Serrano, M. Salaices, Photocatalytic reaction engineering, 2005. https://doi.org/10.1201/b18533.

[72] J.M. Coronado, F. Fresno, M.D. Hernández-Alonso, R. Portela, Design of advanced photocatalytic materials for energy and environmental applications, 2013.

[73] B.G. Kwon, J. Yoon, Experimental evidence of the mobility of hydroperoxyl/superoxide anion radicals from the illuminated TiO2 interface into the aqueous phase, Bull. Korean Chem. Soc. 30 (2009) 667–670.

[74] K.H.H. Aziz, K.M. Omer, A. Mahyar, H. Miessner, S. Mueller, D. Moeller, Application of photocatalytic falling film reactor to elucidate the degradation pathways of pharmaceutical diclofenac and ibuprofen in aqueous solutions, Coatings. 9 (2019) 465. https://doi.org/10.3390/coatings9080465.

[75] Q. Guo, C. Zhou, Z. Ma, X. Yang, Fundamentals of TiO2 Photocatalysis: Concepts, Mechanisms, and Challenges, Adv. Mater. 31 (2019) 1901997. https://doi.org/10.1002/adma.201901997.

[76] J.C. Phillips, Bonds and bands in semiconductors, Academic Press, 1973.

[77] M.S. Solanki, S. Benjamin, Photocatalysis, Adv. Oxid. Process. Waste Water Treat. (2018) 135–175. https://doi.org/10.1016/B978-0-12-810499-6.00006-1.

[78] K.H.J. Buschow, Encyclopedia of materials : science and technology, Elsevier, 2001.

[79] M. Lin, Zhiqun and Ye, Meidan and Wang, Multifunctional Photocatalytic Materials for Energy, Woodhead Publishing, 2018. https://doi.org/10.1016/c2016-0-01653-4.

[80] A. Mills, S.K. Lee, A web-based overview of semiconductor photochemistry-based current commercial applications, J. Photochem. Photobiol. A Chem. 152 (2002) 233–247. https://doi.org/10.1016/S1010-6030(02)00243-5.

[81] A. Hernández-Ramírez, I. Medina-Ramírez, Photocatalytic semiconductors: Synthesis, characterization, and environmental applications, 2015. https://doi.org/10.1007/978-3-319-10999-2.

[82] N. Shaham-Waldmann, Y. Paz, Away from TiO 2 : A critical minireview on the developing of new photocatalysts for degradation of contaminants in water, Mater. Sci. Semicond. Process. 42 (2015) 72–80. https://doi.org/10.1016/j.mssp.2015.06.068.

[83] R. Fagan, D.E. McCormack, D.D. Dionysiou, S.C. Pillai, A review of solar and visible light active TiO2 photocatalysis for treating bacteria, cyanotoxins and contaminants of emerging concern, Mater. Sci. Semicond. Process. 42 (2016) 2–14. https://doi.org/10.1016/j.mssp.2015.07.052.

[84] T. Wang, X. Yan, S. Zhao, B. Lin, C. Xue, G. Yang, S. Ding, B. Yang, C. Ma, G. Yang, G. Yang, A facile one-step synthesis of three-dimensionally ordered macroporous N-doped TiO 2 with ethanediamine as the nitrogen source, J. Mater. Chem. A. 2 (2014) 15611–15619. https://doi.org/10.1039/c4ta01922a.

[85] D.M.E.A. Siegel, Richard W; Hu, Evelyn; Cox, Nanostructure Science and Technology, 1999. https://doi.org/10.1007/978-1-4614-4605-7.

[86] M.K. Nowotny, J. Nowotny, Solid State Chemistry and Photocatalysis, (n.d.).

[87] J.W. (John W. Mullin, Crystallization, Butterworth-Heinemann, 2001.

[88] I. Szafraniak-Wiza, M. Alexe, D. Hesse, Nanosized ferroelectric crystals, in: Handb. Adv. Dielectr. Piezoelectric Ferroelectr. Mater. Synth. Prop. Appl., Elsevier Ltd, 2008: pp. 600–621. https://doi.org/10.1533/9781845694005.5.600.

[89] A. Fougerouse, M. Rousseau, J.L.-T. pearl oyster, undefined 2008, Soft tissue anatomy, shell structure and biomineralisation, Books.Google.Com. (n.d.).

[90] R. Zhang, L. Xie, Z. Yan, Biomineralization mechanism of the pearl oyster, pinctada fucata, 2018. https://doi.org/10.1007/978-981-13-1459-9.

[91] E. Strack, Pearls, (2006).

[92] M.M.H. Al Omari, I.S. Rashid, N.A. Qinna, A.M. Jaber, A.A. Badwan, Calcium Carbonate, in: Profiles Drug Subst. Excipients Relat. Methodol., Academic Press Inc., 2016: pp. 31–132. https://doi.org/10.1016/bs.podrm.2015.11.003.

[93] S. Weiner, L. Addadi, Crystallization Pathways in Biomineralization, Annu. Rev. Mater. Res. 41 (2011) 21–40. https://doi.org/10.1146/annurev-matsci-062910-095803.

[94] Y. Levi, S. Albeck, A. Brack, … S.W.-C.E., undefined 1998, Control over aragonite crystal nucleation and growth: an in vitro study of biomineralization, Wiley Online Libr. (n.d.).

[95] R. Demichelis, A. Schuitemaker, N.A. Garcia, K.B. Koziara, M. De La Pierre, P. Raiteri, J.D. Gale, Simulation of Crystallization of Biominerals, Annu. Rev. Mater. Res. 48 (2018) 327–352. https://doi.org/10.1146/annurev-matsci-070317-124327.

[96] M. Rousseau, L. Pereira-Mouriès, … M.A.-… and P.P.B., undefined 2003, The water-soluble matrix fraction from the nacre of Pinctada maxima produces earlier mineralization of MC3T3-E1 mouse pre-osteoblasts,

Elsevier. (n.d.).

[97] A. Checa, A new model for periostracum and shell formation in Unionidae (Bivalvia, Mollusca), Elsevier. (2000). https://doi.org/10.1054/tice.2000.0129.

[98] R. Jabbour-Zahab, D. Chagot, … F.B.-A.L., undefined 1992, Mantle histology, histochemistry and ultrastructure of the pearl oyster Pinctada margaritifera (L.), Cambridge.Org. (n.d.).

[99] J.P. Cauthler, S. Karampelas, Pearls and corals: “Trendy biomineralizations,” Elements. 5 (2009) 179–180. https://doi.org/10.2113/gselements.5.3.179.

[100] Y. Dauphin, A.D. Ball, M. Cotte, J.P. Cuif, A. Meibom, M. Salomé, J. Susini, C.T. Williams, Structure and composition of the nacre-prisms transition in the shell of Pinctada margaritifera (Mollusca, Bivalvia), Anal. Bioanal. Chem. 390 (2008) 1659–1669. https://doi.org/10.1007/s00216-008-1860-z.

[101] P.E. Saucedo-Lastra, A. Castillo-Domínguez, C.E. Melgar-Valdez, Aprovechamiento de almejas dulceacuícolas en Tabasco para formación de perlas y artesanías, Villahermo, Tabasco, 2015.

[102] C. Rivera-Perez, J.J. Ojeda-Ramirez de Areyano, N.Y. Hernandez-Saavedra, Purification and functional analysis of the shell matrix protein N66 from the shell of the pearl oyster Pteria sterna, Comp. Biochem. Physiol. Part - B Biochem. Mol. Biol. 235 (2019) 19–29. https://doi.org/10.1016/j.cbpb.2019.05.007.

[103] A. Garciagasca, R.I. Ochoabaez, M. Betancourt, Microscopic anatomy of the mantle of the pearl oyster Pinctada-Mazatlanica (Hanley, 1856), J. Shellfish Res. 31 (1994) 85–91.

[104] I.E. Napper, A. Bakir, S.J. Rowland, R.C. Thompson, Characterisation, quantity and sorptive properties of microplastics extracted from cosmetics, Mar. Pollut. Bull. 99 (2015) 178–185.

https://doi.org/10.1016/j.marpolbul.2015.07.029.

[105] A. Cordero-García, G. Turnes Palomino, L. Hinojosa-Reyes, J.L. Guzmán-Mar, L. Maya-Teviño, A. Hernández-Ramírez, Photocatalytic behaviour of WO3/TiO2-N for diclofenac degradation using simulated solar radiation as an activation source, Environ. Sci. Pollut. Res. 24 (2017) 4613–4624. https://doi.org/10.1007/s11356-016-8157-0.

[106] E. Cedillo-González, R. Riccò, … S.C.-A.S., undefined 2018, Below room temperature: How the photocatalytic activity of dense and mesoporous TiO2 coatings is affected, Elsevier. (n.d.).

[107] H. Zeng, J. Xie, H. Xie, B.L. Su, M. Wang, H. Ping, W. Wang, H. Wang, Z. Fu, Bioprocess-inspired synthesis of hierarchically porous nitrogen-doped TiO2 with high visible-light photocatalytic activity, J. Mater. Chem. A. 3 (2015) 19588–19596. https://doi.org/10.1039/c5ta04649a.

[108] M.C. Ariza-Tarazona, J.F. Villareal-Chiu, J.M. Hernández-López, J.R. De la Rosa, V. Barbieri, C. Siligardi, E.I. Cedillo-González, Microplastic pollution reduction by a carbon and nitrogen-doped TiO2: Effect of pH and temperature in the photocatalytic degradation process, J. Hazard. Mater. 395 (2020) 122632. https://doi.org/10.1016/j.jhazmat.2020.122632.

[109] P. Zou, H. Xiong, S. Tang, Natural weathering of rape straw flour (RSF)/HDPE and nano-SiO2/RSF/HDPE composites, Carbohydr. Polym. 73 (2008) 378–383. https://doi.org/10.1016/j.carbpol.2007.12.002.

[110] M. Gardette, A. Perthue, J.L. Gardette, T. Janecska, E. Földes, B. Pukánszky, S. Therias, Photo- and thermal-oxidation of polyethylene: Comparison of mechanisms and influence of unsaturation content, Polym. Degrad. Stab. 98 (2013) 2383–2390. https://doi.org/10.1016/j.polymdegradstab.2013.07.017.

[111] G. Liu, D. Zhu, W. Zhou, S. Liao, J. Cui, K. Wu, D. Hamilton, Solid-phase photocatalytic degradation of polystyrene plastic with goethite modified by boron under UV-vis light irradiation, Appl. Surf. Sci. 256 (2010) 2546–2551.

https://doi.org/10.1016/j.apsusc.2009.10.102.

[112] A. V. Ortiz, J.G. Teixeira, M.G. Gomes, R.R. Oliveira, F.R.V. Díaz, E.A.B. Moura, Preparation and characterization of electron-beam treated HDPE composites reinforced with rice husk ash and Brazilian clay, Appl. Surf. Sci. 310 (2014) 331–335. https://doi.org/10.1016/j.apsusc.2014.03.075.

[113] M. Kanna, S. Wongnawa, Mixed amorphous and nanocrystalline TiO2 powders prepared by sol-gel method: Characterization and photocatalytic study, Mater. Chem. Phys. 110 (2008) 166–175. https://doi.org/10.1016/j.matchemphys.2008.01.037.

[114] T. Theivasanthi, Review on Titania Nanopowder- Processing and Applications, (2017).

[115] T. Matsumoto, N. Iyi, Y. Kaneko, K. Kitamura, S. Ishihara, Y. Takasu, Y. Murakami, High visible-light photocatalytic activity of nitrogen-doped titania prepared from layered titania/isostearate nanocomposite, Catal. Today. 120 (2007) 226–232. https://doi.org/10.1016/j.cattod.2006.07.047.

[116] J. Geng, D. Yang, J. Zhu, D. Chen, Z. Jiang, Nitrogen-doped TiO2 nanotubes with enhanced photocatalytic activity synthesized by a facile wet chemistry method, Mater. Res. Bull. 44 (2009) 146–150. https://doi.org/10.1016/j.materresbull.2008.03.010.

[117] G. Yang, Z. Jiang, H. Shi, T. Xiao, Z. Yan, Preparation of highly visible-light active N-doped TiO2 photocatalyst, J. Mater. Chem. 20 (2010) 5301–5309. https://doi.org/10.1039/c0jm00376j.

[118] K. Kalantari, M. Kalbasi, M. Sohrabi, S.J. Royaee, Synthesis and characterization of N-doped TiO2 nanoparticles and their application in photocatalytic oxidation of dibenzothiophene under visible light, Ceram. Int. 42 (2016) 14834–14842. https://doi.org/10.1016/j.ceramint.2016.06.117.

[119] Y. huo, Y. jin, J. zhu, H. li, Highly active TiO2-x-yNxFy visible photocatalyst prepared under supercritical conditions in NH4F/EtOH fluid, Appl. Catal. B

Environ. 89 (2009) 543–550. https://doi.org/10.1016/j.apcatb.2009.01.019.

[120] T. Luttrell, S. Halpegamage, J. Tao, A. Kramer, E.S.-S. reports, undefined 2014, Why is anatase a better photocatalyst than rutile?-Model studies on epitaxial TiO 2 films, Nature.Com. (n.d.).

[121] G. Socrates, Infrared and Raman characteristic group frequencies: tables and charts, (2004).

[122] R. Li, M. Faustini, C. Boissière, D. Grosso, Water capillary condensation effect on the photocatalytic activity of porous TiO2 in air, J. Phys. Chem. C. 118 (2014) 17710–17716. https://doi.org/10.1021/jp5046468.

[123] I. Kriston, Some aspects of the degradation and stabilization of Phillips type polyethylene, Budapest University of Technology and Economics, 2010.

[124] K.N. Fotopoulou, H.K. Karapanagioti, Degradation of Various Plastics in the Environment, in: Handb. Environ. Chem., Springer Verlag, 2019: pp. 71–92. https://doi.org/10.1007/698_2017_11.

APPENDIX A: Diffusion of the project

PACRIM13
Oct. 27 - Nov. 1, 2019
Okinawa Convention Center, Japan

Certificate of Presentation

We certify that the following presentation was given at The 13th Pacific Rim Conference of Ceramic Societies (PACRIM13) held from October 27 to November 1, 2019 at Okinawa Convention Center, Ginowan-city, Okinawa-pref., Japan.

Date: Oct. 31 (5th day)
Place: Room Theater, Okinawa Convention Center
Presentation number: 31-Theater-S06-22
Presentation style: Oral presentation
Presentation title: Microplastic pollution remediation: photocatalytic degradation of LDPE and HDPE microplastics using N-TiO_2
Authors: Brenda Estefania Llorente Garcia*[1]; Juan Manuel Hernandez Lopez[1]; Juan Jacobo Ruiz Valdes[1]; Cristina Siligardi[2]; Erika Iveth Cedillo Gonzalez[1]
1. Universidad Autónoma de Nuevo León
2. Univesitá degli Studi di Modena e Reggio Emilia
"*" asterisk Indicates an presenter

Nov. 6, 2019

Pacrim13 General Chair
Takaaki TSURUMI
Tokyo Institute of Technology

<CONTACT>
The Ceramic Society of Japan
Pacrim 13 Office
E-mail: pacrim13@cersj.org
http://www.ceramic.or.jp/pacrim13/

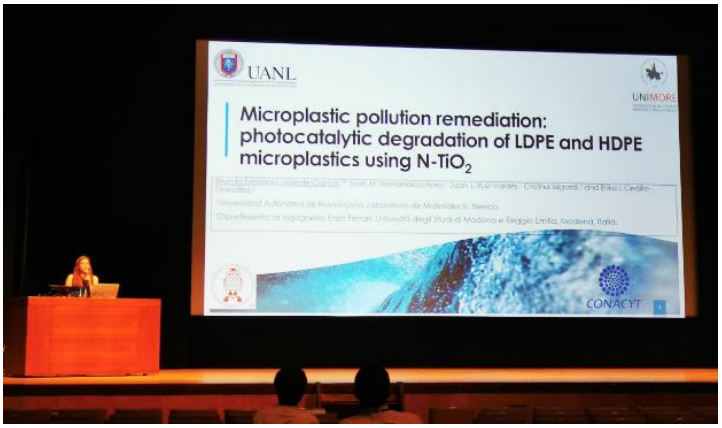

APPENDIX B: Paper accepted for publication on Journal Coatings (MDPI), ISSN 2079-6412, Impact Factor of 2.33 (JCR).

coatings

an Open Access Journal by MDPI

CITESCORE 2.4 SCOPUS

IMPACT FACTOR 2.436

CERTIFICATE OF ACCEPTANCE

Certificate of acceptance for the manuscript (**coatings-821674**) titled:

First insights of the photocatalytic degradation of HDPE and LDPE microplastics by a mesoporous N-TiO2 coating: Effect of the microplastics' size and shape

Authored by:

Brenda Estefanía Llorente-García; Juan Manuel Hernández-López; Antonio Alberto Zaldivar-Cadena; Cristina Siligardi; Erika Iveth Cedillo-González

has been accepted in *Coatings* (ISSN 2079-6412) on 06 July 2020

MDPI Academic Open Access Publishing since 1996

Basel, July 2020